January 2015

ULTRA-FAST LASER ENHANCED PRINTING OF NANOMATERIAL FOR HIGH QUALITY TRANSPARENT ELECTRODE

Qiong Nian
Purdue University

Graduate School Form 30
Updated 1/15/2015

PURDUE UNIVERSITY
GRADUATE SCHOOL
Thesis/Dissertation Acceptance

This is to certify that the thesis/dissertation prepared

By Qiong Nian

Entitled

Ultra-fast Laser Enhanced Printing of Nanomaterial for High Quality Transparent Electrode.

For the degree of Doctor of Philosophy

Is approved by the final examining committee:

Gary J. Cheng Chair	
Joseph Pekny	
Xiulin Ruan	
Hong Wan	

To the best of my knowledge and as understood by the student in the Thesis/Dissertation Agreement, Publication Delay, and Certification Disclaimer (Graduate School Form 32), this thesis/dissertation adheres to the provisions of Purdue University's "Policy of Integrity in Research" and the use of copyright material.

Approved by Major Professor(s): Gary J. Cheng

Approved by: Abhijit Deshmukh 12/8/2015

Head of the Departmental Graduate Program Date

ULTRA-FAST LASER ENHANCED PRINTING OF NANOMATERIAL FOR HIGH QUALITY TRANSPARENT ELECTRODE

A Dissertation

Submitted to the Faculty

of

Purdue University

by

Qiong Nian

In Partial Fulfillment of the

Requirements for the Degree

of

Doctor of Philosophy

December, 2015

Purdue University

West Lafayette, Indiana

To my beloved family.

ACKNOWLEDGEMENTS

First of all, I would like to express my special appreciation and thanks to my advisors Prof. Gary J. Cheng. I would like to thank him for providing me the opportunity to conduct this research and their time, ideas, and funding to make my Ph.D thesis possible.

I would like to thank Prof. Joseph Pekny, Prof. Xiulin Ruan and Prof. Hong Wan for their time to service as my PhD committee members. I thank them for all of their valuable inputs and suggestions.

I would like to thank all my labmates, previous and current, Chang Ye, Yiliang Liao, Martin Zhang, Stanley Gao, Ruby Li, Yingling Yang, David Liu, Yaowu Hu, Biwei Deng, Shengyu jin, Wenqi Wang, Mojib Saei for their kindness discussion with my research and course work. I am also grateful to the staffs of IE department for their help and assistance, especially Mrs Cheryl Barnhart. I also want to specially thank Mr. Michael Callahan, Dr. Dave Look for their help and discussion.

I would also like express my great appreciation to my parents: my father Jiezhong Nian and my mother Caixia Chen. Without their patience and education, I cannot be here in U.S. for my further studying. Without their unselfish support, I can't finish my phd study. They also affected my decision of my career goal to be a scientist. I wish them have a better health. And also I must thank for the support of my sisters for taking care of my parents when I was far away from hometown. Without their sacrifice, I might not be able to assure my phd study for more than five years.

Financial supports by Purdue University in the form of Ross fellowship and teaching assistantship, InMAC fellowship and by NSF, NSF SBIR are acknowledged.

TABLE OF CONTENTS

Page

LIST OF TABLES vii
LIST OF FIGURES viii
ABSTRACT xiii
CHAPTER 1. INTRODUCTION 1
1.1. Motivation 1
1.2. Objectives 3
CHAPTER 2. BACKGROUND AND LITERATURE REVIEW 7
2.1. Development of TCEs 7
2.2. Development of ZnO:X TCEs 8
2.3. Development of metal nanowires TCEs 10
2.4. Proposed solution for fabrication of low cost & high quality TCEs 11
CHAPTER 3. STATEMENT OF RESEARCH 13
3.1. Impact of Proposed Research upon The State-of-The-Art 13
3.2. Methodology and Mechanism of the Ultra-Fast Laser Enhancement AZO Nanoparticles 14
3.2.1. Ultra-fast laser irradiation on nanoparticles 14
3.2.2. AZO nanoparticles localized welding 16
3.2.3. Ultra-fast laser effect on macro-film temperature evolution 20
3.2.4. Summary of Laser enhancement of AZO nanoparticles coating 22
3.3. Methodology and Mechanism of the Ultra-Fast Laser Enhancement Ag Nanowires 23
3.3.1. Ultra-fast irradiation on nanowires 23
3.3.2. Heat Generation on localized junctions between crossed nanowires 25
3.3.3. Laser induced local welding 26
3.3.4. Summary of laser induced local welding of nanowires 30

CHAPTER 4. CHARACTERIZATIONS 32
4.1. Scanning electron microscope 32
4.2. Transmitted electron microscope 32
4.3. X-ray photoelectron spectroscopy 33
4.4. Optical transmittance 34
4.5. Electrical measurements 35
4.6. Summary of the chapter 36
CHAPTER 5. LASER ENHANCED AZO COATING 37
5.1. The case of high vacuum deposited AZO film 37
5.1.1. Introduction 37
5.1.2. AZO film deposition and laser processing 38
5.1.2.i. Pulsed laser deposition 38
5.1.2.ii. UV Laser processing 39
5.1.3. Microstructure change after laser processing 41
5.1.3.i. Grain growth induced by laser crystallization 41
5.1.3.ii. AZO film crystallinity enhancement 42
5.1.4. Performance characterization and discussion 45
5.1.4.i. Electrical conductance characterization 45
5.1.4.ii. Optical transmittance 48
5.1.5. Summary of this section 51
5.2. UV Laser Crystallization of Solution Based AZO Nanoparticles Ink 51
5.2.1. Introduction 51
5.2.2. Film preparation and laser processing 53
5.2.2.i. Solution Based AZO Nanoparticles Ink Fabrication 53
5.2.2.ii. Low cost AZO film coating 55
5.2.2.iii. AZO coating quality Characterization 57
5.2.2.iv. AZO coating laser processing 58
5.2.3. Microstructure change after laser processing 60
5.2.3.i. Grain growth and size distribution 60
5.2.3.ii. AZO polycrystalline film grain growth thorough depth 61

5.2.4. Performance characterization and discussion 63
5.2.4.i. Electrical conductance Improvement 63
5.2.4.ii. The decrease of electro trap density at grain boundaries 65
5.2.4.iii. Laser Intensity Effect 67
5.2.4.iv. Pulse Number Effect 69
5.2.4.v. Forming gas annealing 70
5.2.5. Optical performance discussion 73
5.2.5.i. Transmittance 73
5.2.5.ii. HAZE measurements 74
5.2.6. Summary of this section 77
CHAPTER 6. LASER ENHANCED AG NANOWIRE NETWORK PRINTING 80
6.1. Introduction 80
6.2. Sample printing and laser processing 83
6.2.1. AgNW network printing 83
6.2.2. AgNW network surface and transparency 85
6.2.3. Laser processing set up 87
6.3. Microstructure change after laser processing 90
6.3.1. Surface modification 90
6.3.2. Laser welded nanojunctions 91
6.3.3. The mechanism of localized welding 93
6.4. Performance characterization and discussion 96
6.4.1. Electrical conductance and optical transparency 96
6.4.2. Percolation theory 99
6.4.3. HAZE measurements 102
6.4.4. Mechanical and chemical stability 104
6.4.5. Overexposure effect 106
6.5. Summary of this chapter 107
CHAPTER 7. CONCLUSION 109
LIST OF REFERENCES 112
VITA 120
PUBLICATIONS 121

LIST OF TABLES

Table Page

Table 3.1 Parameters for interatomic potential of MD simulation 17

Table 5.1. Peak Position, Full width at half maximum (FWHM) of XRD AZO (0002) peaks and grain size for as-deposited and processed AZO films..... 44

Table 5.2. Electrical Properties of n-type AZO films as-deposited and processed by laser 45

Table 5.3. Room temperature Hall measurement of spin coated precursor layers..... 58

Table 5.4. UV laser crystallization parameters effect on AZO sol gel layer (run 12) carrier mobility..... 67

Table 5.5. UV laser crystallization parameters effect on AZO nanoparticle layer (run 13) carrier mobility..... 69

LIST OF FIGURES

Figure Page

Figure 1.1. TCEs used in touchscreen (a) and thin film Photovoltaics (b) 1

Figure 2.1. Proposed low cost & high quality TCEs fabrication route 12

Figure 3.1. (a) Laser beam local field concentration simulated by Comsol Multiphysics® with a Gaussian electromagnetic wave as incident beam on neighboring AZO nanoparticles, suspended in air and touching each other. Gaussian beam laser was delivered with an electrical field of 1 V/m. Each nanowire was modeled as having a circular cross-section and essential physical parameters input, (b) The field distribution at nanoparticle contacts, (c) The field distribution and heat generation in nano-scale as a function of distance to the contacts, described by power loss density calculated by Comsol Multiphysics® 16

Figure 3.2. (a) MD simulation procedure of Laser heating on AZO nanoparticles stack based on nanoscale Laser-nanoparticle interaction. (b) Overall view of initial structure for half of the simulation box consisting of closely packed AZO particles plane through periodic boundary; the other half is another identical closely packed plane of particles with point contact between two planes. (c) Sliced plane cross front-view direction to observe AZO nanoparticles stack before LASER PROCESSINGC; (d) after LASER PROCESSINGC. 19

Figure 3.3. (a) Focus-in view of crystal structure at contacts between AZO nanoparticles before LASER PROCESSINGC; (b) after LASER PROCESSINGC. 20

Figure 3.4. (a) COMSOL multiphysics® simulation of Ultra-laser effect on AZO film, (b) temperature evolutionary of AZO film corresponding to different laser intensities. 21

Figure 3.5. top view SEM images of Ultra-laser processed AZO film 22

Figure 3.6. Mechanism of as-coated small grains (**a**) grew by melting (**b**), merging (**c**), crystallizing and finally impinging to each other (**d**) 23

Figure 3.7. Comsol Multiphysics® simulation of laser irradiation on crossed Ag nws: incident Laser beam was simulated as a Gaussian electromagnetic with an electrical field of 1 V/m. nanowires crossed at zero degrees (parallel to each other) and at ninety degrees, suspended in air and touching each other, respectively. Each nanowire was modeled as having a circular cross-section with 40nm diameter and essential physical parameters input. The cross-section image of focus-in view indicates local electrical field distribution, where color legend changes from blue (minimum V/m) to red (maximum V/m). 24

Figure 3.8. (a) Laser beam local field concentration simulated by Comsol Multiphysics® with a Gaussian electromagnetic wave as incident beam on a cross of nanowire junctions. (b) The heat generation in AgNW as a function of distance to the crossed junction, decribed by power loss density calculated by Comsol Multiphysics®. (c) The heat generation in AgNW as a function of gap size between the crossed nanowire junction. 26

Figure 3.9. (a) Molecular Dynamic simulation setup of laser induced local welding. Temperature evolution was represented in cross section view (XZ plane slice) in the middle of crossed nanowire junctions (b) initial status, (c) welding status, and (d) cooling status. Nanowire FCC crystal structure evolution cross section view (XZ plane slice) in the middle of junctions (e) initial status, (f) welding status, and (g) cooling status. And nanowire ordering structure evolution cross section view (XZ plane slice) in the middle of junctions (h) initial status, (i) welding status, and (j) cooling status. 29

Figure 3.10. Perpendicular crossed nanowires CNA and CNC analysis: (a) Molecular Dynamic simulation setup of LPW. Temperature evolution was represented in cross section view (XZ plane slice) in the middle of crossed nanowire junctions (b) initial status, (c) welding status, and (d) cooling status. Nanowire FCC crystal structure evolution cross section view (XZ plane slice) in the middle of junctions (e) initial status, (f) welding status, and (g) cooling status. And nanowire ordering structure evolution cross section view (XZ plane slice) in the middle of junctions (h) initial status, (i) welding status, and (j) cooling status. 30

The local welding effect of nanowires was characterized by means of plane-view scanning electron microscopy (SEM). In figure 3.11, it shows plan view SEM images collected before welding and after different exposure times, respectively. Before welding, individual nanowires all over the image were clearly distinct throughout the junctions. However, the nanowire to nanowire junctions subject to after laser exposure get started welding, which is indicated by contrast change at the forming solder point. Apparently, the junctions welded together completely, is demonstrated by the solder point formed. 30

Figure 3.11. (a) randomly crossed Ag nanowire network before laser welding; (b) randomly crossed Agnanowire network after local welding. 31

Figure 4.1 Two mode for specimen observation of TEM: (a) diffraction mode; (b) image mode. 33

Figure 4.2. (a) Lamda 950 optical transmittance measurement, (b) The difference between diffusive transmittance and specular transmittance. 35

Figure 4.3 Thin film electrical properties measurement via four points method. 36

Figure 5.1. SEM images of as deposited AZO film by PLD. The inset is the grain size distribution histogram. 39

Figure 5.2. (a) laser processing set up, (b) As-deposited AZO film by PLD, and AZO film processed by laser processing (at 500K): (c) 120mJ/cm2, 5μs, (d) 160mJ/cm2, 5 μs. 41

Figure 5.3. (a) Grain size distribution of As-deposited AZO film by PLD; and grain size distribution of AZO film processed by LASER PROCESSING (at 500K): (b) 120mJ/cm2, 5μs; (c) 160mJ/cm2, 5 μs. 42

Figure 5.4. a) θ-2θ XRD patterns of AZO films as-deposited by PLD and processed by LASER PROCESSING at 120mJ/cm^2, 160mJ/cm^2, and 200mJ/cm^2 at 500K, respectively. The AZO films have a preferred (0002) out-of-plane orientation on the c-plane sapphire substrate. b) Thermal strain introduced by LASER PROCESSING. AZO (0002) peak of the crystallized samples show 0.1^o high angle shift. 43

Figure 5.5. Electron mobility vs. electron concentration for AZO films as-deposited by PLD and processed by UVL, comparing with nine research groups. The red curve shows current work, the other marked points and curves represent high mobility AZO films fabricated by other research groups. The diagonal dashed lines show constant conductivity on a log-log scale. 48

Figure 5.6 (a) Effect of laser crystallization conditions on UV to near IR transmittance spectra of AZO films; (b) UV to mid wave IR transmittance spectra of uncoated sapphire substrate and AZO films deposited by room temperature PLD (R_S = ~67 Ω/square) and processed by UVL (R_S = ~40 Ω/square and ~7500 Ω/square). 50

Figure 5.7. Process map of sol-gel AZO nanoparticles ink fabrication and coating..... 55

Figure 5.8. SEM top view of Spin coated AZO layers: a. Sol Gel layer b. Nanoparticle layer..... 56

Figure 5.9. SEM cross-section view of Spin coated AZO layers: a. Sol Gel layer b. Nanoparticle layer 57

Figure 5.10. XRD of AZO film fabricated via spin coating of aqueous solution precusurs. 58

Figure 5.11. SEM plane view of Spin coated AZO layers before and after UV laser crystallization: a. Sol Gel layer; b. Sol Gel layer after UV laser crystallization; c. Nanoparticle layer; d. Nanoparticle layer after UV laser crystallization. 60

Figure 5.12. The grain size distribution histograms of AZO film: (a) sol gel fabricated AZO film before laser processing: (b) after laser process. (c) commercial nanoparticles coated AZO film before laser processing: (d) after laser process. 61

Figure 5.13. SEM cross-section view of spin coated AZO layers before and after UV laser processing: a. Sol Gel layer; b. Sol Gel layer after process; c. Nanoparticle layer; d. Nanoparticle layer after process. 62

Figure 5.14. The electrical conductance of polycrystalline AZO film enhanced by laser processing: pulse number dependence of Hall measurement with optimal laser intensity of 172 mJ cm^{-2}. 64

Figure 5.15. The physical model of polycrystalline AZO film structure and electrical conductance 67

Figure 5.16, Hall measurements of AZO films processed by UV laser with following FMG. 71

Figure 5.17. (a) Scheme of polycrystalline AZO and the electron traps formed by oxygen species at grain boundaries. The oxygen species tend to absorb electrons and form negative potential

barrier. XPS spectra of AZO film before and after laser and FMG process (a) binding energy peak index to O 1s and (b) binding energy peak index to Zn $2p_{3/2}$. 73

Figure 5.18. Influence of UV laser on transmittance: (a) Visible-IR transmittance spectrum of UV laser and FMG processed AZO films, (b) the transmittance measurements of variable samples processed with and without FMG. 74

Figure5.19. (a) Light scattering measurement set up: The difference in the diffusive transmittance and the specular transmittance evaluates light scattering scale. Influence of UVLC parameters on AZO films UV-Vis-IR transmittance; (b) light scattering spectrum of processed AZO film. 75

Figure 5.20. the performance of diffusive transmittance, specular transmittance and light scattering at 550nm of UVLC AZO films, comparing with glass, CNT, silver nanowires, and graphene hybrid material. 76

Figure 5.21. (a) The performance of transmittance at 550nm and sheet resistance for AZO films, comparing with ITO, CNT, silver nanowires, metal gratings and graphene. (b) Electron mobility vs. electron concentration for AZO films processed by UVLC and FMG, comparing with high vacuum deposition by nine research groups. The red curve shows current work, the other marked points and curves represent high mobility AZO films listed for comparison. The diagonal dashed lines show constant conductivity on a log-log scale. 79

Figure 6.1. Commercial scalable roll to roll printer. 82

Figure 6.2. Ultra-fast laser processing set up. 83

Figure 6.3. AgNW ink and the nanowire SEM images, collected from Blue Nano Inc. 84

Figure 6.4. (a) schematic setup of the roll-to-roll printing system, (b) an 8 in. by 4 in. uniform printing of AgNWs on a PET substrate. 85

Figure 6.5. The SEM observation of the printed AgNW film on PET substrate in 4 different area densities: (a) P1~3.1×10^{-6} g cm^{-2}; (b) P2~7.3×10^{-6} g cm^{-2}; (c) P3~1.1×10^{-5} g cm^{-2}; (d) P4~1.6×10^{-5} g cm^{-2}. The scale bar is 5 μm. 86

Figure 6.6. Measured sheet resistance (15% variance) and optical transmittance of printed AgNW film according to 4 different area densities 87

Figure 6.7. Schematic of the AgNW junction laser processing on PET substrate. The nanowires naturally contact with each other, and then enable local heating at junctions by laser exposure. . 88

Figure 6.8. (a) Optical transmittance of bare PET versus wavelength and laser exposure time. The plots show the total diffusive transmittance as a function of wavelength for different exposure time for PET substrate. The diffusive transmittance include both specular transmitted and scattered light collected by integrating sphere. (b) XRD patterns of bare PET as a function of laser exposure time. The plots show PET structure change according to different exposure time. 89

Figure 6.9. (a) plan-view SEM images of AgNW film before laser treatment. Scale bar is 500nm. Plane view SEM images of AgNW films after laser processing with different exposure time: (b) 1.25 μs; (c) 2.50 μs; (d) 3.75 μs. Scale bar is 500nm. 91

Figure 6.10. (a) HRTEM image of nanowire junction after 2.50 μs laser exposure. (b) Magnified HRTEM image of joint area formed by laser treatment. 92

Figure 6.11. (a) HRTEM image of a single nanowire, while the insert represents the SAED patterns of the nanowire. (b), (c) and (d) Low-magnification TEM image of a nanowire junction after laser processing..... 94

Figure 6.12. (a) and HRTEM of welded junctions, the square represents the size and location of the optical diffraction aperture used for the FFT patterns. (b) Scheme of growing silver nanowire crystal structure, where central axis of nanowire is [111] direction and growing plane is along (111) facets. Nanowires welded together merge over growing plane..... 95

Figure 6.13. (a) Optical transmittance of P2 AgNW transparent electrode film versus wavelength and laser exposure time. The plots show the total diffusive transmittance as a function of wavelength for different exposure time for P2 sample. Insert: P2 AgNW transparent electrode sheet resistance corresponding to laser exposure time. (b) Optical transmittance of P3 AgNW transparent electrode film versus wavelength and laser exposure time. Insert: P3 AgNW transparent electrode sheet resistance corresponding to laser exposure time. 98

Figure 6.14. (c) P2 AgNW film sheet resistance and conductivity as a function of percolation junction resistance R_0, calculated by percolation theory with thickness T of 70nm and percolated 'stick' length L of 500nm. (d) P3 AgNW film sheet resistance and conductivity as a function of percolation junction resistance R_0, calculated by percolation theory with thickness T of 100nm and percolated 'stick' length L of 300nm. 100

Figure 6.15. Scheme of AgNW network conductance dominated by contact resistance through percolating nanowires and the scheme of LPW effect on nanowire contact resistance..... 102

Figure 6.16. Diffusive and specular transmittance of PET substrate, CNT on glass, Ag nanowire on glass, Graphene hybrid on glass, and P2, P3 AgNW on PET substrate. The differences in the diffusive and specular transmittance indicate the scattering of the light by the material. 104

Figure 6.17. (a) The ratio of bending resistance to original resistance as a function of bending curvature before and after laser processing for P2 and P3 samples, comparing to standard ITO film. The insert shows the designed bending gadget. (b) chemical stability test of laser processed P2 AgNW network on PET. (c) chemical stability test of laser processed P3 AgNW network on PET. 105

Figure 6.18. AgNW film sheet resistances as a function of laser power. The inserts shows the demonstration of selected area of damaged nanowires by over exposure and some area of destroyed nanowires by ultra-intense laser ablation. 107

Figure 6.19. Optical transmittance @550nm wavelength of laser welded P2 and P3 AgNW TCE as a function of sheet resistance. The performance of ITO, CNT, Graphene, and metal gratings are shown for comparison..... 108

Figure 7.1. IDTechEx©, Transparent Conductive Films (TCF) 2014-2024: Forecasts, Markets, Technologies NanoMarkets™, Emerging Markets for Non-ITO Transparent Conductive Oxides, 2011 110

ABSTRACT

Qiong Nian. PhD., Purdue University, December 2015. Ultra-fast laser enhanced printing of nanomaterial for high quality transparent electrode. Major professor: Gary J. Cheng.

Direct printing of nanomaterials, which integrate nanomaterials into a film via low cost mean, is designed to fabricate transparent conductive electrode (TCE) film. Following laser processing is utilized as the post treatment to enhance the film performance. The laser processing is proposed in order to weld nanomaterials in nanoscale and enhance the electrical conductance of the nanomaterials film. Rigid glass substrate was chosen as the substrate to load nanomaterials printing; however, this laser processing also can be utilized to flexible substrate like polymer and bendable glass. Aluminum doped zinc oxide nanoparticles and silver nanowires were chosen as the printable nanomaterials. The laser – nanomaterial interaction and temperature evolution was studied by Comsol Multiphysics software. The localized nanowelding was simulated by Molecular Dynamic simulation. The SEM, TEM and XRD results show that microstructure of nanomaterials film was improved significantly after laser induced nanowelding. The theoretical study of the electrical conductance enhancement is presented in the thesis. The direct printing techniques and ultra-fast laser processing have the potential to boost the efficiency when used in commercial mass – production.

CHAPTER 1. INTRODUCTION

1.1. Motivation

As increasing development and widespread of smart-devices, touchscreen laptops and thin film Photovoltaics devices, transparent conductive electrodes (TCEs), which transmit light and conduct electrical current simultaneously, are essentially needed for mass production[1]. They are mainly used as the top screen and window layer as shown in Figure 1.1.

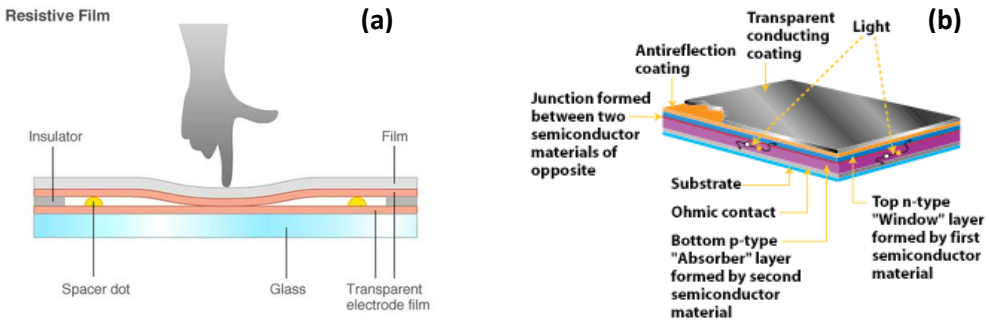

Figure 1.1. TCEs used in touchscreen (a) and thin film Photovoltaics (b)

TCEs were known in the end of 19th century, when the first example was thin metal films prepared by evaporation and sputtering[1]. Transparent conductive oxides (TCOs) was probably first investigated by Bädeker in 1907, including CdO, Cu_2O and PbO[1]. Bädeker obtained resistivity as low as 1.2×10^{-3} Ωcm, that is only around one order of

magnitude higher than the resistivity of indium tin oxide (ITO) films which is the standard optoelectronic utilized TCO layers today[2]. In 1925, understanding of the electrical properties and doping of semiconductors improved significantly due to quantum mechanics[1]. Researchers identified the roles of intrinsic defects including vacancies, substitutional and interstitial lattice site defects. TCOs films could be deposited various techniques, such as oxidation of thin metal films; the sputtering of metal targets in a reactive atmosphere; and chemical deposition onto hot glass by spraying or dipping 367. The broad industrial application of TCO materials began at the end of the 1960s, and developed around 1970s with flat-panel display technology demand, ITO became the most commonly used TCOs for transparent electrodes [3].

These transparent conductive oxides dominated the field of transparent electrodes for past three decades. Out of the different possible TCOs available, only SnO_2:X and ZnO:X (X is a dopant) have gained widespread attention, owing to their wide bandgap >3 eV, allowing for applications in the visible and near-UV range (down to 300 nm), and their low resistivities of around 10^{-3} Ω cm or lower. Among them, ITO (X is indium for SnO_2:X) is the most popular TCO material owing to the lowest resistivity on a commercial scale (2×10^{-4} Ωcm)[4]. Today, it is widely used as the transparent electrode in flat-panel displays[5] and also a transparent electrode, especially in amorphous silicon or CdTe thin-film solar cells[6, 7].

However, as increasing cost of indium, ZnO:X with resistivity in the range of $2\text{-}4\times10^{-4}$ Ωcm attracts much attention, which is also used as a window and contact layer in thin-film solar cells. To achieve low resistivity in a transparent electrode requires the carrier

concentrations and carrier mobility to be as high as possible. Whereas the maximum carrier concentration is limited by the dopant solubility in the host material (~ 2×10^{21} cm^{-3}), carrier mobility are limited by the multiple scattering mechanism according to different carrier concentration level.

Recently, researchers began searching for low cost fabrication method for TCOs and other alternative TCEs[8], in parallel with the exponential rise of the flat-panel display industry. These new research efforts are driven by several factors such as: (1) the increasing price of indium, (2) the high cost and limitation for high vacuum fabrication, (3) the quest for sheet resistances below 5Ω/sq for large displays and large-area solid-state lighting[9]. The potential low cost fabrication method for ZnO:X includes sol gel spin coating, nanoparticle ink printing and spray coating. Other alternatives includes periodic metal grids or irregular metal nanowire networks, which are usually prepared by the lithography of metal films or direct printing of metal nanowires from solutions[10-12].

1.2. Objectives

It is well known extended defects like inter-grain voids, grain boundaries and electro traps in grain boundaries play important roles in electrical and optical properties of AZO thin film[13]. For instance, these defects may bring free carrier scattering centers and tend to decrease the carrier lifetime so as to drawback the carrier mobility, resulting in low electrical conductivity of the film[14]. Though electrical conductivity can be enhanced by increasing impurity doping level, but this is usually achieved at the expense of red/IR transparency[15]. Thus, carrier scattering center minimization, in low impurity

doping level with low carrier concentration, become critical to optimize carrier mobility and finally achieve satisfied electrical conductivity for TCOs, simultaneously retaining high transparency. And, random nanowire networks, which have the potential to embed in TCOs for enhancing conductance, suffer from the intrinsic problem of percolation and large contact resistances between nanowires. In this study, we aim to accomplish the following objectives:

(a) Study on mechanism of ZnO:X transparent electrode film enhancement by ultra-fast laser. As an important component of this research, mechanism of grain growth and grain boundary modification is critical to understand the ultra-fast laser enhancement on the film.

(b) Investigation on methodology low cost ZnO:X transparent electrode film fabrication and modification by ultra-fast laser enhancement. In order to lower the cost of transparent electrode manufacturing simultaneous retain outstanding optoelectronic performance, the research focus will be placed on methodology of ultra-fast laser enhancement on the quality modification of solution fabricated low-cost ZnO:X film (spin coating, inkjet nanoparticle printing).

(c) Investigation on methodology low cost metal nanowire transparent electrode film printing and modification by ultra-fast laser. In order to embed the metal nanowire to flexible transparent electrode film to enhance optoelectronic performance, the research focus will be placed on methodology of ultra-fast laser on the quality modification of the metal nanowire network printed by roll to roll printing and inkjet printing.

(d) Study on mechanism of metal nanowire printing enhancement by ultra-fast laser. As an important component of the metal nanowire embedding, mechanism of nanowire percolation and large contact resistance modification is critical to understand the ultra-fast laser enhancement on the film.

(e) Proposal for a new fabrication route for ultra-fast laser enhanced printing of high quality transparent electrode. Lastly but the most important, a novel fabrication route to make low cost high quality transparent electrode film will be proposed. The method will combine the printing of solution based metal oxide nanoparticles or metal nanowires, and ultra-fast laser enhancement on the quality of this low cost fabricated transparent electrode film. The optoelectronic performance will be measured. The proposed fabrication route would be helpful to lower the film manufacturing cost and to avoid additional film patterning process in industry.

1.3. Structure of Dissertation

This dissertation is structured as follows. (1) Chapter 1 is the introduction. (2) Chapter 2 reviews the literature of transparent electrodes, the development of metal oxide based transparent electrodes and metal nanowire mesh based transparent electrodes. (3) Chapter 3 summarized the state of art for this research. Mainly, the simulation and experimental work were performed in order to study the laser processing effect on metal oxide nanoparticles film and metal nanowire film. It is focusing on the nanojoining between adjacent nanomaterials and the nanojunction formation. (4) Chapter 4 lists the material characterization and performance test methods of this thesis. (5) In chapter 5, Aluminum

doped zinc oxide (AZO) nanoparticels were coated as cutting edge low cost transparent electrode film, and followed by laser processing. The microstructures were studied after coating and laser processing. The recrystallization mechanism induced by UV laser was studied. Grown grain and decreased internal defects after laser process, leads to increased electro mobility inside the AZO polycrystalline films. (6) Chapter 6 summarizes the laser processing was integrated to roll to roll printing of silver nanowire film. In this chapter, the laser induced nanojoining between crossed nanowires leads to macros scale film conductance increase without compromise on optical transmittance. (7) Chapter 7 summarization of this dissertation.

CHAPTER 2. BACKGROUND AND LITERATURE REVIEW

2.1. Development of TCEs

Transparent conductive electrodes (TCEs), mainly transparent conductive oxides (TCOs), are usually used in optoelectronic devices like flat panel displays and Photovoltaics. They are fabricated with polycrystalline or amorphous structures by various deposition or coating techniques including high vacuum deposition such as DC sputtering[16], pulsed laser deposition (PLD)[17], Atomic layer deposition (ALD)[18] and chemical vapor deposition (CVD)[15]. Generally, to satisfy the application requirement, these TCEs need to achieve greater than 80-85% transmittance of incident light as well as resistivity lower than 1-2×10^{-3} Ωcm for efficient carrier transport. The transmittance of these films, just as in any transparent material, is limited by light scattering at defects and grain boundaries [19, 20]. And for use as thin-film electrodes in solar cells, TCEs should have a minimum carrier concentration on the order of 10^{20} cm^{-3} for low resistivity and a band gap lower than 380 nm to avoid absorption of light over most of the solar spectra[2]. Mobility in these films is limited by ionized impurity scattering and grain boundary scattering, on the order of 10-40 $cm^2/(V\ s)$. Currently used TCOs in industry are primarily n-type conductors, meaning their primary charge carrier as electrons.

To date, the industry standard in TCE is ITO (tin-doped indium-oxide) because of best optoelectronic property[21]. ITO achieves low resistivity of ~1-2$\times 10^{-4}$ Ωcm and a transmittance over 80%. However, ITO has the drawback of being expensive, that is due to the film's primary metal Indium is rare (6000 metric tons worldwide, 2006) and price fluctuates due to market demand (over $800/kg, 2006)[22]. Therefore, earth abundant doped zinc oxide (ZnO:X) has been proposed as alternative materials[21], as well as other like metal nanowires network[23].

2.2. Development of ZnO:X TCEs

Zinc oxide (ZnO) thin films have drawn much attention recently due to significant advantages over other transparent conductive oxide (TCO) films like indium oxide and tin oxide such as chemical stability in reducing environments, and availability to doping with a wide range of materials[15, 24]. Among extrinsic n-type dopant elements, Aluminum (Al) is the most widely used in ZnO thin films owing to two reasons: (i) Al and Zn have similar electronegativity and (ii) the ionic radius of Al is slightly smaller than Zn[25]. Furthermore, the Al dopant is able to enhance the thin film conductivity by supplying more free charge carriers, at the same time stabilizing the electrical property of ZnO thin films by impeding the chemisorption of oxygen at the surface and grain boundaries [26].

Al doped ZnO (AZO) is currently under intense investigation and development to replace indium tin oxide (ITO) as TCO film[27], though latter one is the standard compound for most applications performing best optoelectronic property[21]. Since it is crucial that AZO ensure a sustainable supply of the earth abundant and cost-effect alternatives and which is also reflected in predicted markets of $925 million in 2016 for alternative TCOs[28]. Meanwhile, AZO thin films

also exhibit impressive and reliable electro-optical performance and environmental benefits [21, 29], leading to wide application in display windows[21, 30], thin film solar cells[31, 32], and opto-electronic devices[33]. Nowadays, various deposition techniques are applied to prepare high quality AZO film with resistivity of 10^{-3} Ωcm and visible transmittance over 85%, such as DC sputtering[16], pulsed laser deposition (PLD)[17], Atomic layer deposition (ALD)[18] and chemical vapor deposition (CVD)[15]. However, these high vacuum methods are accompanied with issues like instrumental complexity, high investment costs and limits scalability[21], which draw immense demand to develop softer deposition conditions like low cost non-vacuum methods.

It is well known extended defects like inter-grain voids, grain boundaries and electro traps in grain boundaries play important roles in electrical and optical properties of AZO thin film[13]. For instance, these defects may bring free carrier scattering centers and tend to decrease the carrier lifetime so as to drawback the carrier mobility, resulting in low electrical conductivity of the film[14]. Though electrical conductivity can be enhanced by increasing impurity doping level, but this is usually achieved at the expense of red/IR transparency[15]. Thus, carrier scattering center minimization, in low impurity doping level with low carrier concentration, become critical to optimize carrier mobility and finally achieve satisfied electrical conductivity, simultaneously retaining high transparency.

Therefore, a variety of solution based approaches and post improvement have been tried to obtain good optoelectronic properties comparable to vacuum deposition techniques, but achieving a high electrical conductivity (~1000 S/cm) with transparency over 85-90% (T@550nm) has not been succeed yet to date.

2.3. Development of metal nanowires TCEs

Due to wide application in today's ubiquitous flat panel displays and touch screen technologies, as well as thin-film solar cells and light emitting diodes, low-cost and large scale manufactured transparent conductive electrodes (TCEs) have drawn increasing attention. Various types of TCEs have been used in optoelectronics including indium tin oxide (ITO), aluminum doped zinc oxide (AZO) and alternatives like single-wall carbon nanotubes (CNTs), graphenes and silver nanowires (Ag nws). Owing to low-cost synthesis and film fabrication, networks of Ag nws CNTs have been intensively investigated to replace ITO which is the standard compound for most application performing best optoelectronic property. However, Ag nws/CNTs still suffer from the problem of excessive agglomeration which would further deteriorate visible range transparency, especially when Ag nws have high aspect ratio (~35nm in diameter and ~15-20um in length).

Besides, according to[34], for Ag nws network corresponding to transmittance of 85-95%, conduction is typically dominated by percolation through junctions with relative large nw-nw contact resistance (MΩ). A variety of attempts have been made to decrease the sheet resistance by improving the junction contact conductance, including self-forming of nws[35], thermal annealing under pressure and electroplating. However, it has been challenging to reduce the sheet resistance to < 20 Ω/sq, simultaneously holding the transparency over 90%. On the other hand, optical welding of Ag nw junctions has been invented by Garnett *et al.* recently, which bring a potential for directly improving nw-nw junction conductance without any device damage, nanowire shape change nor additive material[34]. The optical welding depends on material absorption and the light intensity;

in particular metals exhibit large ohmic losses, enable effective light concentration and serve as efficient and light driven sources of heat. It can be illustrated that one can rapidly raise and lower the temperature in nanoscale metallic structures with the use of pulsed lasers.

2.4. Proposed solution for fabrication of low cost & high quality TCEs

To fabricate the low cost and high quality transparent conductive electrode films, a novel process is proposed consisting of nano-material precursor printing (low cost) and the post ultra-fast laser enhancement (high quality) as given in Figure 2.1. In the first step, investigation will be made on AZO nanoparticles precursor coating and printing on substrate. Then, ultra-fast laser enhancement of AZO nanoparticle coating will be carried out make sure the post treatment is capable to improve the film quality. Then, Ag nanowire will be printed by roll to roll printing (commercial scale) and modified by similar ultra-fast laser process. This nanomaterials printing is a deliberately controlled process to coat homogeneous thin film by low-cost, fast and flexible route. The ultra-fast laser enhancement performs as the post treatment to further improve the structural, electrical and optical properties of the nanomaterials printings. Finally, the AZO nanoparticles and Ag nanowires after laser treatment would possess high quality, providing a potential to form hybrid film, to enhance the electrical conductance with little compromise of transparency.

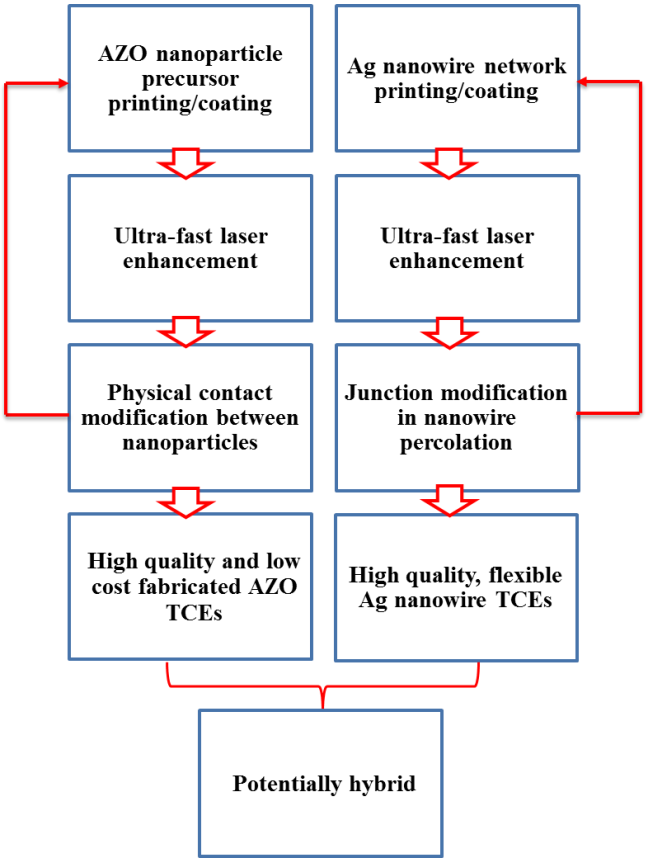

Figure 2.1. Proposed low cost & high quality TCEs fabrication route

CHAPTER 3. STATEMENT OF RESEARCH

3.1. Impact of Proposed Research upon The State-of-The-Art

The proposed ultra-fast laser enhanced printing of nanomaterials for high quality transparent electrode combines two approaches: (1) mass-production and printing of low-cost nano-ink on substrates, and (2) ultra-fast laser post treatment to enhance film quality. Combining these two processes, the challenges of low cost and high quality of transparent electrode film can be met. Success in this proposed idea is expected to immediate the commercial scale mass-production, given any degree of success is able to suggest a possible cheap or efficient TCEs manufacturing route which already attract and will retain the attention of industry. The specific impacts are discussed as follows.

The precursor printing/coating is a very promising technique in thin film electronics for achieving both high performance and low cost. Advantages include: *Low cost:* the process does need neither high temperature nor high vacuum equipment, which lower the cost of manufacturing process; *High quality:* the stoichiometric ratio is fixed almost molecularly, which results in the formation of thin films with a very uniform composition; *Efficiency and Flexibility:* The printing/coating can be used to fabricate thin films on flexible substrate and can achieve efficient manufacturing by scaling up from lab to industry levels inexpensively.

Ultra-fast laser post treatment of nano-ink film for improving quality of thin film includes advantages: *High speed*: the frequency (50-100KHZ) of the commercial available diode pump solid state (DPSS) laser is much higher than the lab-used Eximer laser system (10HZ), which make it possible to process commercial-scale large devices like touch panels and solar panels; *Versatility*: the Ultra-fast laser beam can be directed to multiple targets by adjusting the light path with mirror systems. And this direct laser scanning process without high vacuum/high temperature is favorable on product assembling line over traditional post treatment like furnace annealing; *selectivity*: due to selective heating (via choice of wavelength) and a much smaller heat-affected zone, laser treatment area be designed precisely; and laser treatment could be applied to most functional materials since laser wavelength can be selected to have high absorption only by nanomaterials. Energy saving: due to high absorption coefficient of nano-scale materials, very low profile laser conditions are required to process nano-ink thin film compared with bulk materials; the short on/off relaxation time subject to ultra-fast laser process makes high temperature controlling system required by traditional furnace annealing unnecessary.

3.2. Methodology and Mechanism of the Ultra-Fast Laser Enhancement AZO Nanoparticles

3.2.1. Ultra-fast laser irradiation on nanoparticles

To understand the mechanism of laser process nano-ink, we performed a Comsol Multiphysics® simulation with a Gaussian electromagnetic wave as incident on a cross of nanomaterials printing. The crystallization occurring in nano-scale, laser-nanoparticle interaction, which is fundamentally different with bulk materials, needs to be aware of.

As illustrated in Figure 3.1a, two AZO nanoparticles are simulated with essential physical parameter impute, suspended in air and point contacted over surface, then exposed to laser beam with electrical field of 1 V m^{-1}. Unlike bulk material, the field distribution of round shape nanoparticles is polarized due to plasmonic effect. The mechanism of plasmonic effect remains unknown, but it relates to enriched electrons and high relative permittivity of N-type semiconductor has been demonstrated in prior reports and our simulation. Polarized field distribution, magnified in Figure 3.1b, shows intensive electrical field enhancement near nanoparticle contacts, achieving as high as 9 V m^{-1}. While the field strength distributes inside nanoparticles remaining in lower level as high as 0~1 V m^{-1}, indicating nanoparticle contacts form "hot spots" during laser-mater interaction. To further explore the heating process generated by the 'hot spots', the electromagnetic power loss density as a function of distance to nanoparticle contacts was plotted in Figure 3.1c. The heat generation was determined from the illumination power density multiplies the AZO nanoparticle absorption coefficient (imaginary part of the dielectric function)[36], that is, the power loss density calculated in Comsol Multiphysics®. Heat generation decreases as distance to nanoparticle contacts increasing, implying the effective heat zone of initial laser scanning is constrained near contacts within around ±10nm. Although following heat dissipation and diffusion spread thermal energy all over nanoparticles, the nanoparticle contacts still desire further investigation to determine how the heat generation and diffusion influence the phase transformation and mass transport.

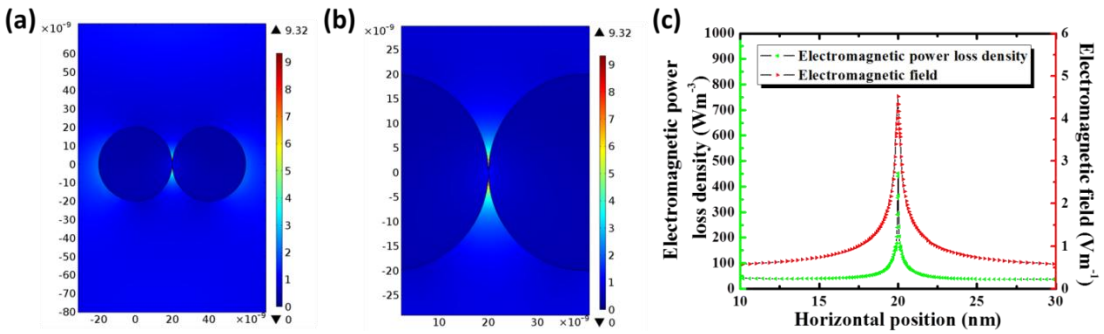

Figure 3.1. (a) Laser beam local field concentration simulated by Comsol Multiphysics® with a Gaussian electromagnetic wave as incident beam on neighboring AZO nanoparticles, suspended in air and touching each other. Gaussian beam laser was delivered with an electrical field of 1 V/m. Each nanowire was modeled as having a circular cross-section and essential physical parameters input, (b) The field distribution at nanoparticle contacts, (c) The field distribution and heat generation in nano-scale as a function of distance to the contacts, described by power loss density calculated by Comsol Multiphysics®.

3.2.2. AZO nanoparticles localized welding

To delve into the evolution of AZO nanoparticles after laser irradiation induced hot spots formation, Although following heat dissipation and diffusion spread thermal energy all over nanoparticles and neighboring ones, the nanoparticle contacts still desire further investigation to determine how the heat generation and diffusion influence the phase transformation and mass transport during macro scale crystallization. Thus, Molecular Dynamic Simulation was performed to simulate Laser heating on three layers of closely

packed AZO nanoparticles using LAMMPS[37] with periodic boundary conditions applied in all three dimensions. The OVITO[38] package was used for visualization. Firstly, the Laser heating input on these nanoparticles was set constrained in heat effect zone as calculated above, and then letting heat dissipation and diffusion spread all over. Secondly, to simulate atoms motion and mass transport between AZO nanoparticles, the standard Newton equations of motion were integrated in time using the velocity Verlet algorithm with a time step of 0.25 fs, as shown in Figure 3.2a. The interaction between metal and oxygen atoms was modeled using the Binks potential (i.e. rigid ion approximation)[39, 40]. The Binks inter-atomic potential has the form:

$$E(r_{ij}) = A\exp(\frac{-r_{ij}}{\rho}) - \frac{C}{r_{ij}^6} + \frac{q_i q_j}{r_{ij}} \qquad \text{Eq. 3.1}$$

where r_{ij} is the distance between ions i and j, q_i and q_j are the electric charges of ion i and j. A, ρ, and C are potential parameters listed in Table 3.1. On right-hand side of EQ.3.1, the first and second terms describe the short-range repulsive and attractive interactions, respectively. The additional third term represents the long-range Columbic potential, which invokes the particle-mesh Ewald technique[41]. The cutoff for the Columbic term is set to 8 angstroms. Pairwise interactions within the cutoff distance are computed directly; interactions outside the cutoff distance are computed in reciprocal space.

Table 3.1 Parameters for interatomic potential of MD simulation

Species		A(eV)	P(Å)	C(eVÅ6)
O^{2-}	O^{2-}	9547.96	0.21916	32.0
Zn^{2+}	O^{2-}	529.70	0.3581	0.0
Zn^{2+}	Zn^{2+}	0.0	0.0	0.0

Figure 3.2b only shows one plane of AZO nanoparticles consisted of 5 particles that touch each other in simulation box and through periodic boundary. Each particle with wurtzite structure is consisted of approximately 650000 atoms and 20 nm in diameter. However, overall three dimensional structures is closely packed in each plane and in point contact for out of the plane direction, two discrete planes touch each other on the poles of particles. Due to the memory limitations we only represent one plane of particles in the picture of Figure 3.2b. Before the start of Laser heating part, equilibrium has been reached by running simulation in NPT ensemble for 10 ps. Laser heating has been applied to structure using a uniform heating all over the structure. To create hot spots, excessive heating has been applied over the connecting geometry of particles in a band of 30 nm in width. An exponential function has been used to identify excessive heating as a function of depth inward to touching particles. The uniform heating and the maximum in exponential heating are both equivalent to 5.6 μeV/fs per atom, meaning the maximum heating rate that an atom can acquire is 11.2 μeV/fs. Also this heating rate is very high but it is required for MD simulation to reach the same heating input as experiment in acceptable computing time. Figure 3.2c and 3.2d depict the structure modification of AZO particles stack before and after heating, which clearly show the particles coalesce together and forming “patch” like contact phase after LASER PROCESSINGC. The new phase in state of gaps between particles, results from atom movement driven by Binks inter-atomic potential change during laser/heat-matter interaction. The formation of patch-like phases tends to connect particles, squeeze internal gaps and voids and finally condense loose AZO nanoparticles stack. The reducing of internal gaps and voids, which serve as mid-band electron traps, is crucial for electron mobility improvement.

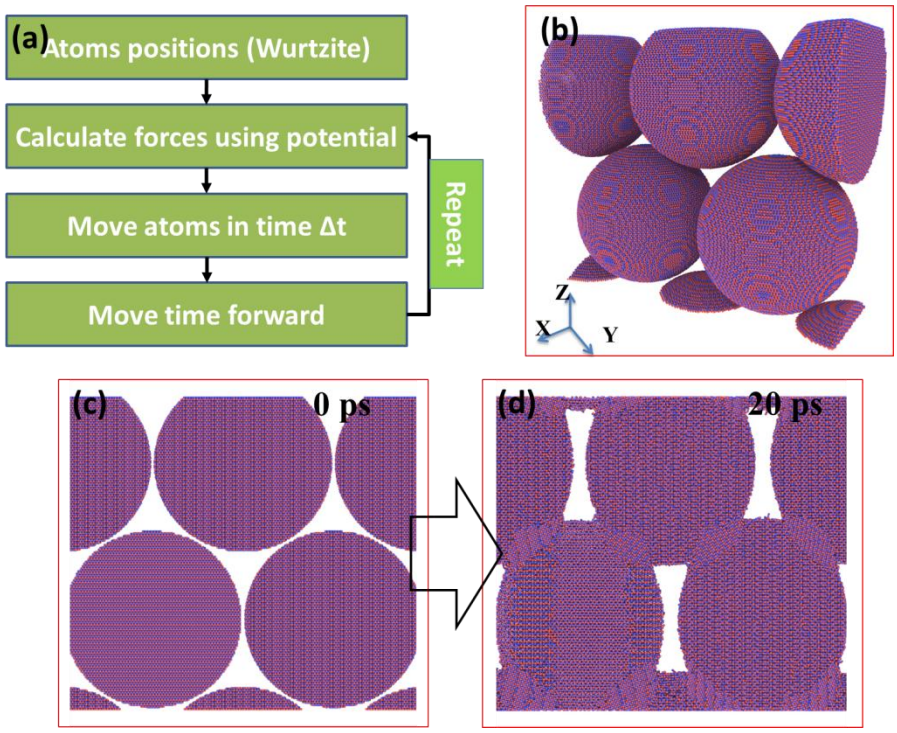

Figure 3.2. (a) MD simulation procedure of Laser heating on AZO nanoparticles stack based on nanoscale Laser-nanoparticle interaction. (b) Overall view of initial structure for half of the simulation box consisting of closely packed AZO particles plane through periodic boundary; the other half is another identical closely packed plane of particles with point contact between two planes. (c) Sliced plane cross front-view direction to observe AZO nanoparticles stack before LASER PROCESSINGC; (d) after LASER PROCESSINGC.

Moreover, as demonstrated by focus-in observations of Figure 3.3a and 3.3b, the lattice structure formed by mass transport though contains plenty of disordering, tends to generate ordering alternatively arranged zinc atoms and oxygen atoms to certain extent.

However, rather than ordering crystal lattice, even amorphous boundary between particles would definitely assist electron migration comparing with inter-particle gaps which are usually supposed as infinite potential well only allowing electron tunneling. On the other hand, the amorphous boundaries allow both electron tunneling and barrier crossing, while the latter one is dominant and determined by the barrier height which finally traces back to the disordering structures and electro traps at boundaries.

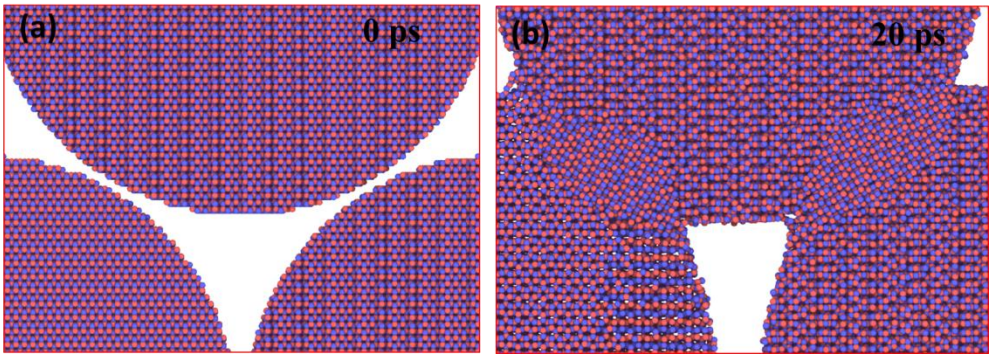

Figure 3.3. (a) Focus-in view of crystal structure at contacts between AZO nanoparticles before LASER PROCESSINGC; (b) after LASER PROCESSINGC.

3.2.3. Ultra-fast laser effect on macro-film temperature evolution

Trying to analyze the temperature history in macro-film induced by laser beam power loss density, COMSOL Multiphysics® was applied to simulate the laser energy absorption as schemed in Figure 3.4a. The electromagnetic module (EM) was used to simulate Laser irradiation, and the heat transfer module (HT) was used to describe the temperature increase in AZO nanoparticles during a single laser pulse delivery. The result of one laser pulse irradiation was represented in Figure 3.4b, the temperature of

AZO nanoparticles increases to 800-1500K in 60ns depending on laser fluence of 120-200 mj/cm^2, respectively. Then the temperature of the AZO nanoparticles would be lowered by thermal dissipation, before subsequent Laser pulse delivery.

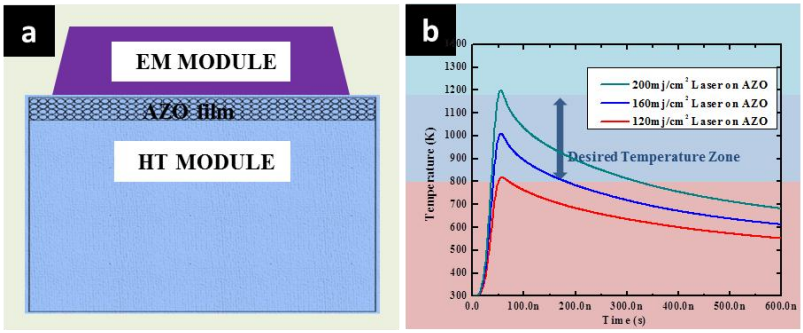

Figure 3.4. (a) COMSOL multiphysics® simulation of Ultra-laser effect on AZO film, (b) temperature evolutionary of AZO film corresponding to different laser intensities.

Figure 3.5 shows the top view FESEM image of the Laser scanned film, as thermal energy continues along multi laser pulse delivery, AZO nanoparticles tend to melt and merge until faceted boundaries formed and impinged with each other. Comparing untreated to transition and finally treated area, it is found that the UV laser crystallized AZO film is more compact and continuous, implying the crystallinity of the AZO film has been significant enhanced [13, 29]. The good film homogeneity and crystal quality result from the AZO crystal growth and reductions of internal defects include inter-crystal gaps and voids [42]. Grain boundary density was also decreased due to small sized crystal merged and larger size crystal formed.

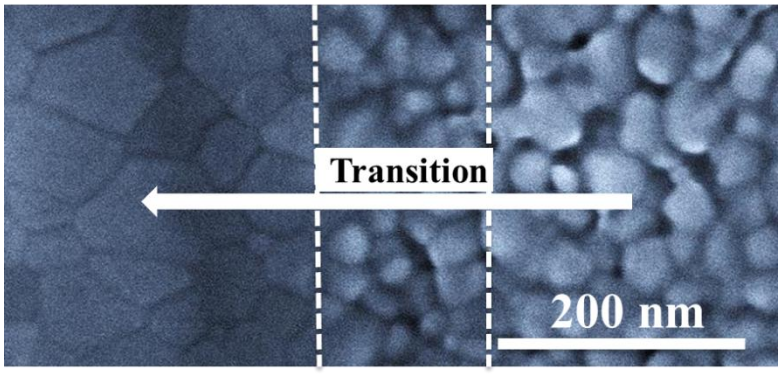

Figure 3.5. top view SEM images of Ultra-laser processed AZO film

3.2.4. Summary of Laser enhancement of AZO nanoparticles coating

It can be seen from Figure 3.6a that the as-coated AZO films exhibit loose film structure with plenty of defects like voids, gaps, and grain boundaries, inhomogeneous and discontinuous [29, 43]. Figure 3.6b and c shows that the small grains grew to large size and became facetted with apparent grain boundaries when UV Laser was delivered to the AZO film with intensity of 173mJ/cm^2 (optimal intensity during experiments). The small grains grew by melting, merging, crystallizing, and finally impinging to each other, when homogeneous and continuous film quality was achieved (Figure 3.6d). Apparently, large grains formed would lower the grain boundaries density for the same AZO film area. On the other hand, since the nanocrystal shape changed to facetted and impinged with each other, the inter grain defects like voids, gaps and discontinuity decreases, which originally may create energy levels in the band gap that tend to trap the free carriers and decrease their lifetime, causing high film resistivity [14].

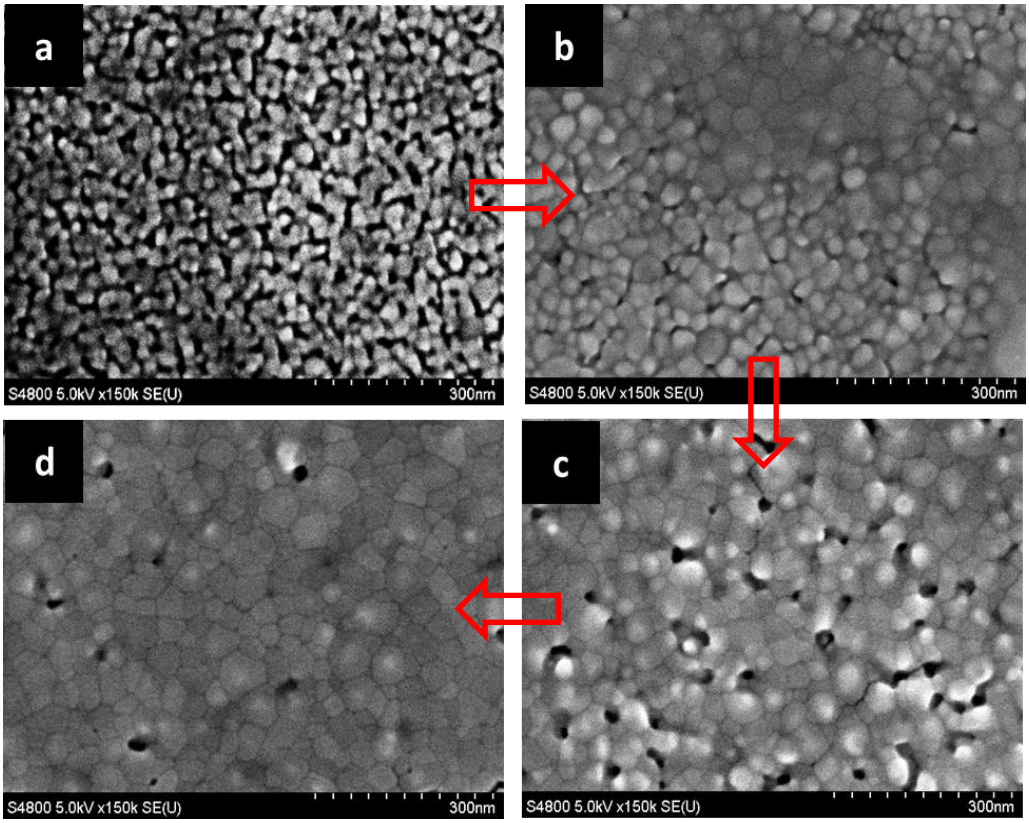

Figure 3.6. Mechanism of as-coated small grains (**a**) grew by melting (**b**), merging (**c**), crystallizing and finally impinging to each other (**d**)

3.3. Methodology and Mechanism of the Ultra-Fast Laser Enhancement Ag Nanowires

3.3.1. Ultra-fast irradiation on nanowires

To understand the consequence of laser irradiation on nanowires, we performed a Comsol Multiphysics® simulation with a Gaussian electromagnetic wave as incident laser on a cross of nanowire junctions, as shown in Figure 3.7. Gaussian beam laser was delivered to Ag nws with an electrical field of 1 V/m, where the diameter of Ag nws was set as 40

nm. In the simulation, we considered a Gaussian beam illumination on Ag nws crossed at ninety degrees, suspended in air and touching each other. Each nanowire was modelled as having a circular cross-section and with essential physical parameters input. The simulation provided local electric field values in the crossed nanowire junctions shown in SF3. Local electrical field was concentrated as high as 13-14 V/m near junction area due to Surface Plasmon Polarization[34, 44, 45]. However, for paralleled Ag nws junctions, only 4.5 times enhancement subject to adjacent paralleled nanowires was observed. This suggests that laser welding favors the crossed nanowire junctions over paralleled ones, which nearly would not affect welding quality of random Ag nws film printed in this study since crossed junctions dominated. Additionally, it is well deserved to note that solely several nanometers gap is able to enhance the local electrical field and form 'hot spot', while leaving the nanowire away from the junctions remain nearly unaffected.

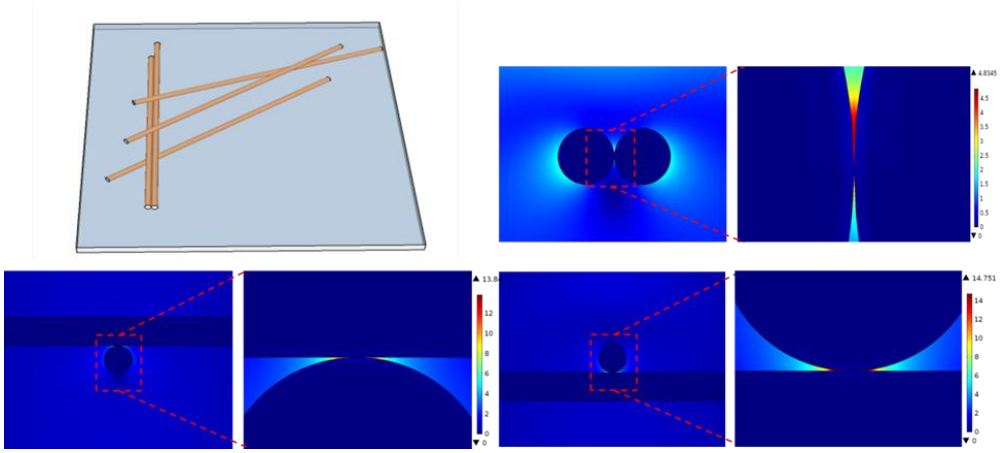

Figure 3.7. Comsol Multiphysics® simulation of laser irradiation on crossed Ag nws: incident Laser beam was simulated as a Gaussian electromagnetic with an electrical field of 1 V/m. nanowires crossed at zero degrees (parallel to each other) and at ninety degrees, suspended in air and touching each other, respectively. Each nanowire was modeled as

having a circular cross-section with 40nm diameter and essential physical parameters input. The cross-section image of focus-in view indicates local electrical field distribution, where color legend changes from blue (minimum V/m) to red (maximum V/m).

3.3.2. Heat Generation on localized junctions between crossed nanowires

To further explore the heating process generated by the 'nano heater', the electromagnetic power loss density as a function of the distance to junctions and gap size between nanowires was plotted in Figure 5b and c. The power loss density calculated by Comsol Multiphysics®, was determined from the illumination power density multiplies the metal nanostructures absorption coefficient (imaginary part of the dielectric function, constant for mono wavelength laser)[36], that indicates, the heat generation. Figure 5b illustrates that the heat generation limits near AgNW junction (±5 nm), and decreases as distance to junctions increasing. It implies that the effective zone of LPW is constrained near junctions with about 5 nm variations, providing efficient junction welding without nanowire itself affecting. This is in good agreement with Figure 3 that the nanowire away from junctions remain nearly unchanged. Figure 5c illustrates that as the gap size between nanowires decreases, which is nanowires come closer together, the power loss density increases, indicating the heat generation spikes. The apparent heat generation was solely observed in small gaps like size lower than 5nm, but still supplying sufficient nano-welding for nanowire junctions usually with a gap size in 2nm due to organic ligands. As the gap size increases, the power loss density decrease and the heating become less effective, which protects nanowire itself from being affected[34, 46].

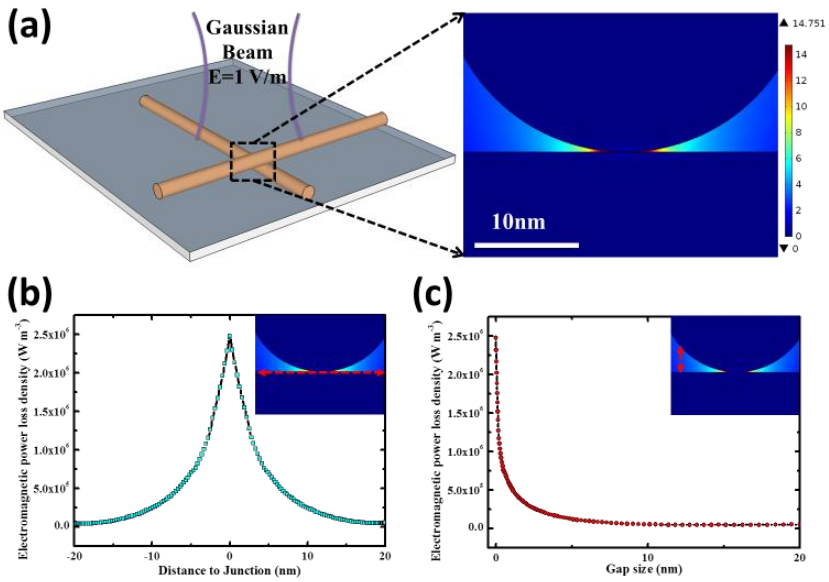

Figure 3.8. (a) Laser beam local field concentration simulated by Comsol Multiphysics® with a Gaussian electromagnetic wave as incident beam on a cross of nanowire junctions. (b) The heat generation in AgNW as a function of distance to the crossed junction, decribed by power loss density calculated by Comsol Multiphysics®. (c) The heat generation in AgNW as a function of gap size between the crossed nanowire junction.

3.3.3. Laser induced local welding

With constrained heat generation around nanowire junctions, to further delve into the joining process and forming structure of solder point, Molecular Dynamics (MD) simulation was implemented. LAMMPS[37] package was used in this simulation setup. As shown in figure 3.9a, silver nanowires either crossed in random angels or perpendicularly were considered in a box with periodical boundaries in all directions. Firstly, NPT ensemble with pressure of 1 atm and equilibrium temperature of 300 K for 100 ps was applied. Then, in NVE ensemble laser heating was considered as a heat

source focused in nanowire junctions. To fay with COMSOL simulation, heating was introduced as an exponential function of distance. The maximum in exponential heating is equivalent to 5.6 μeV/fs per atom. Laser heating has been continued for 150 ps and then the heating source was turned off while simulation continued for an additional 500 ps in a NVT ensemble. For this last simulation step the Nose-Hoover thermostat has been weakened using a time constant equal to 1000 time steps. This is to match simulation with the real case where the structure cools down in air in a slower pace compared to laser heating phase.

In this simulation the interactions between silver atoms has been simulated using EAM[47] potential extracted from prior work of *Williams et al.*[48]. A time step of 1 fs was used during the whole simulation, with OVITO[49] being utilized for visualization. Figures 3.9b, c and d show temperature evolution of structure after NPT run (initial state), just after laser heating (welding state), and at the end of simulation (cooling state), respectively. These figures show a XZ plane cross section view in the middle of junction area. From figure 3.9c, it is clear that heat generation was mainly focused near nanowire junctions, though heat diffusion and dissipation occurs, resulting in thermally activated silver atoms created in the junction. Figures 3.9e, f and g represent the result of common neighbor analysis (CNA)[50] for equivalent states corresponding to figures 3.9b, c and d, in which perfect FCC structure was marked green while other disordering structures were marked grey. It is interesting to observe how the structure evolved from the initial structure to a distorted state during welding, however by going to cooling state it gradually returns to ordered crystalline structure with apparent grain boundary. The

disordering structure formed during welding, attribute to thermally excited atoms tending to vibrate and resist staying in original lattice position. These excited isolated metal atoms possess high mobility, diffusing over nanowire junctions and enabling welding process[51]. While, during cooling process these activated atoms tend to follow the arrangement of matrix to gain the perfect FCC crystalline structure back due to Binks potential, though 2 layers of atoms formed boundary between different grain orientations. This reflects that although heated junction was distorted, the perfect crystalline structure would be formed due to enough spacing time between laser pulses. As well as figure 3.9h, i and j, structure disordering degree in lattice structure indicated by Centro-Symmetry parameter[52] (CNC) analysis. As shown, the CNC analysis was done on laser welded randomly crossed silver nanowires. The color legend on the right hand side illustrate that the disordering increases when color changes from blue to red. Comparing the three processes shown in the figures, it is clearly seen that during welding process, the silver atoms in both two nanowires were thermally excited tending to vibrate and resist stay in original position. However, in the cooling process, the energy of metal atoms decreases, driving the atoms reorganized to low energy structure which is crystallized and ordering structure. A boundary with 2 or 3 layers of atoms was formed due to unmatched lattice orientation between the bottom and top nanowire.

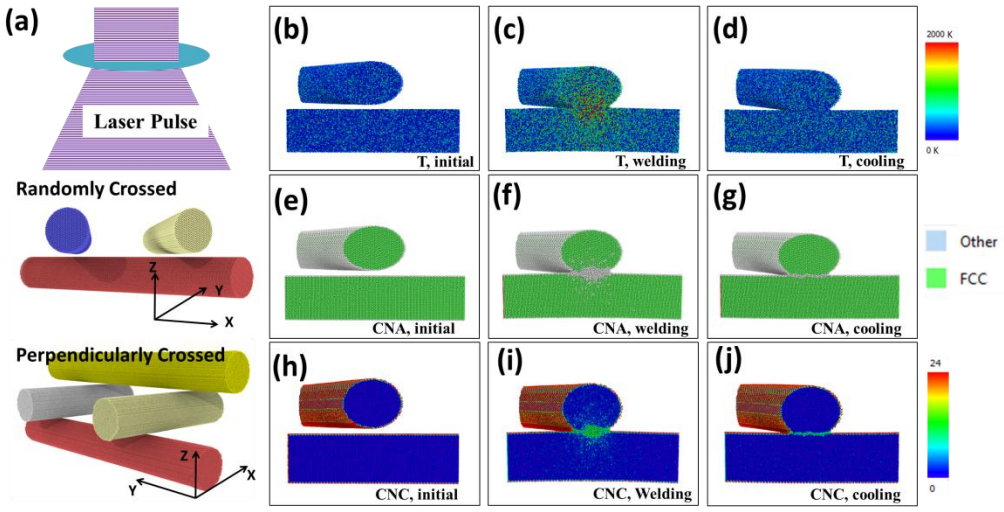

Figure 3.9. (a) Molecular Dynamic simulation setup of laser induced local welding. Temperature evolution was represented in cross section view (XZ plane slice) in the middle of crossed nanowire junctions (b) initial status, (c) welding status, and (d) cooling status. Nanowire FCC crystal structure evolution cross section view (XZ plane slice) in the middle of junctions (e) initial status, (f) welding status, and (g) cooling status. And nanowire ordering structure evolution cross section view (XZ plane slice) in the middle of junctions (h) initial status, (i) welding status, and (j) cooling status.

However, upon perpendicular nanowire junction shown in figure 3.10a, b and c, due to perfectly matched lattice orientation of two crossed nanowires, metal atoms inside welding point recrystallize and reorder into single crystal phase (FCC) without any boundaries formed. CNC analysis in the figure 3.10d, e and f verify this statement as well. Additionally, SF2 also shows the XZ plane cross section view of local welding on nanowires crossed in 90 degrees and the corresponding structure in a diagonal slice in YZ plane. Thus, an angle-dependable recrystallization process during laser welding was

demonstrated, providing a guild for further research and application of aligned AgNW device.

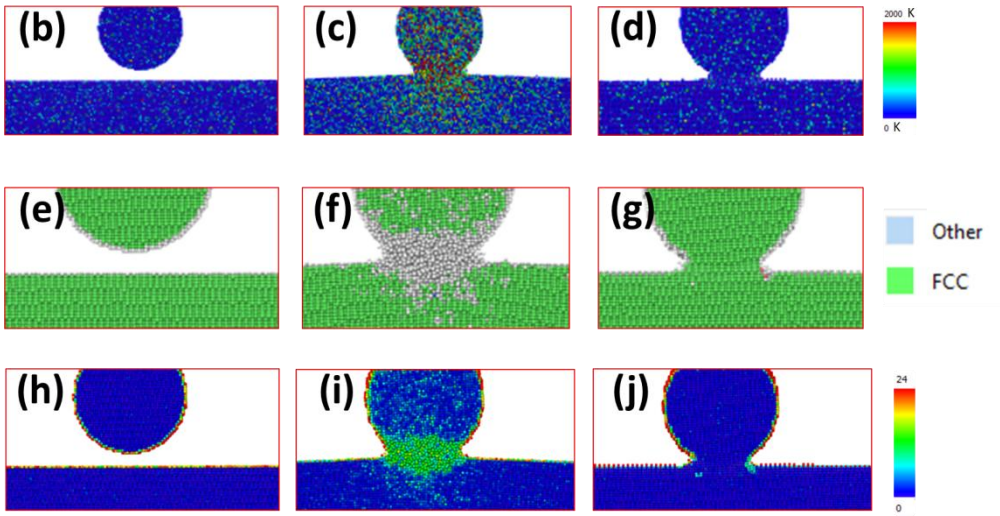

Figure 3.10. Perpendicular crossed nanowires CNA and CNC analysis: (a) Molecular Dynamic simulation setup of LPW. Temperature evolution was represented in cross section view (XZ plane slice) in the middle of crossed nanowire junctions (b) initial status, (c) welding status, and (d) cooling status. Nanowire FCC crystal structure evolution cross section view (XZ plane slice) in the middle of junctions (e) initial status, (f) welding status, and (g) cooling status. And nanowire ordering structure evolution cross section view (XZ plane slice) in the middle of junctions (h) initial status, (i) welding status, and (j) cooling status.

3.3.4. Summary of laser induced local welding of nanowires

The local welding effect of nanowires was characterized by means of plane-view scanning electron microscopy (SEM). In figure 3.11, it shows plan view SEM images

collected before welding and after different exposure times, respectively. Before welding, individual nanowires all over the image were clearly distinct throughout the junctions. However, the nanowire to nanowire junctions subject to after laser exposure get started welding, which is indicated by contrast change at the forming solder point. Apparently, the junctions welded together completely, is demonstrated by the solder point formed.

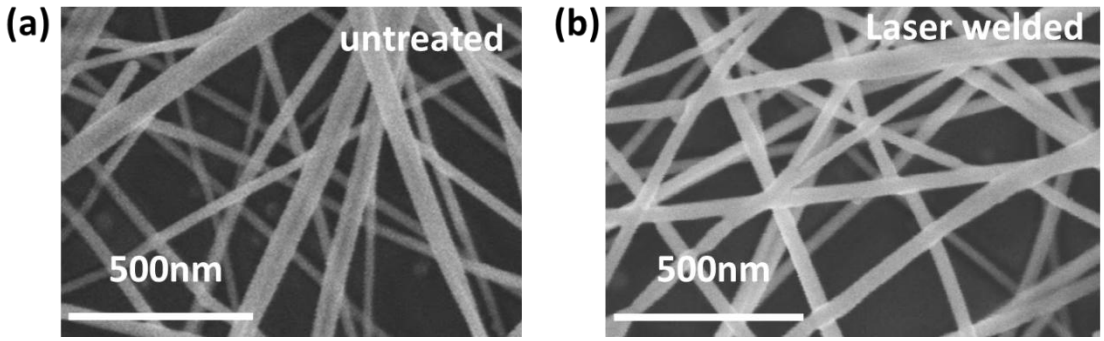

Figure 3.11. (a) randomly crossed Ag nanowire network before laser welding; (b) randomly crossed Agnanowire network after local welding.

CHAPTER 4. CHARACTERIZATIONS

4.1. Scanning electron microscope

Scanning Electron microscopy (SEM): sample surface morphology before and after laser modification is characterized by SEM (Hitachi S-4800 Field Emission SEM) for 2-D images (Hitachi S-4800 Field Emission SEM).

4.2. Transmitted electron microscope

Transmission electron microscopy (TEM) is an imaging technique whereby a beam of high energy electrons passes through a thin specimen. TEM contains two widely used modes for the specimen observation: the image mode and the diffraction mode (as shown in Figure 4.1). In the image mode, the scattered beams with elastically scattered electrons, combined with the transmitted beam, are projected on the fluorescent screen. By blocking the scattered beams with the objective aperture, the bright field (BF) images with high contrast could be obtained. On the other hand, dark field (DF) images, with only diffracted electrons could be obtained by blocking the transmitted beam. In the diffraction mode, the diffraction pattern of an area could be obtained to identify the crystallography.

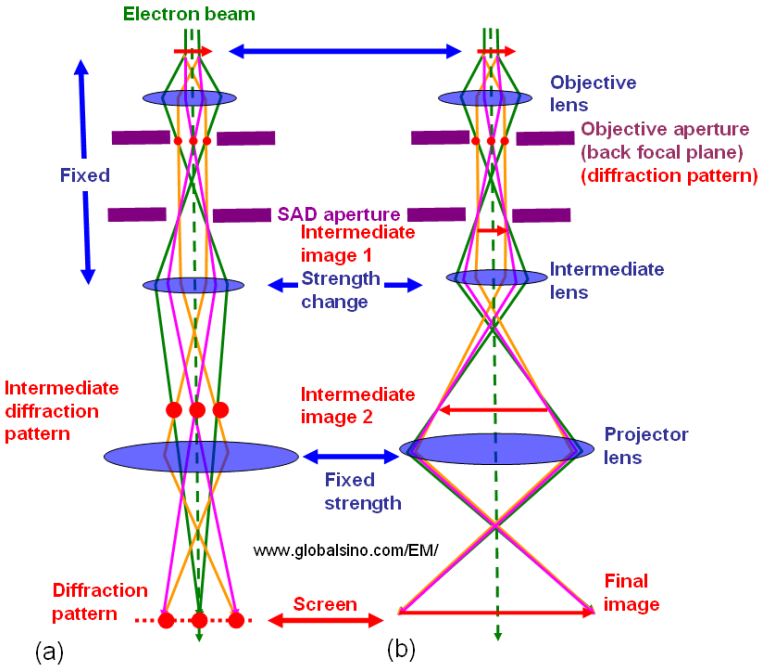

Figure 4.1 Two mode for specimen observation of TEM: (a) diffraction mode; (b) image mode.

In this research, TEM (FEI-Tecnai TEM and FEI-Titan TEM, operated at 200 kV and 300 kV, respectively) were used to characterize the microstructures after processing. During TEM operation, the Gatan imaging filter (GIF) was utilized to exclude the inelastic scattered part to improve the quality of diffraction patterns and observe the weak diffraction spots originating from precipitates.

4.3. X-ray photoelectron spectroscopy

X-ray Photoelectron Spectroscopy (XPS) provides information about the element and chemical composition of a substrate. The AXIS ULTRA DLD incorporates quantitative

real-time parallel XPS imaging with a lateral resolution of 5 μm. The system integrates Monochromatic Al Kα (1486.6 eV) and Ag Lα (2984.3 eV) anodes, non-monochromatic dual anode X-ray gun with Al Kα (1486.6 eV) and Mg Kα (1253.6 eV), which were used to characterize the chemical bonding of film before and after laser process.

4.4. Optical transmittance

In Figure 4.2, the diffusive transmittance was measured by Lambda 950 with an integrating sphere to integrate all forward light including both specular transmitted and scattered transmitted. The specular transmittance indicates the light comes out of the sample parallel to the incident light. The difference between the diffusive and specular transmittance is utilized to investigate the light scattering which is also called HAZE[23, 53], which might trigger problematic in flat panel displays and touch screens applications. The diffusive and specular transmittance data are collected at 550 nm wavelength.

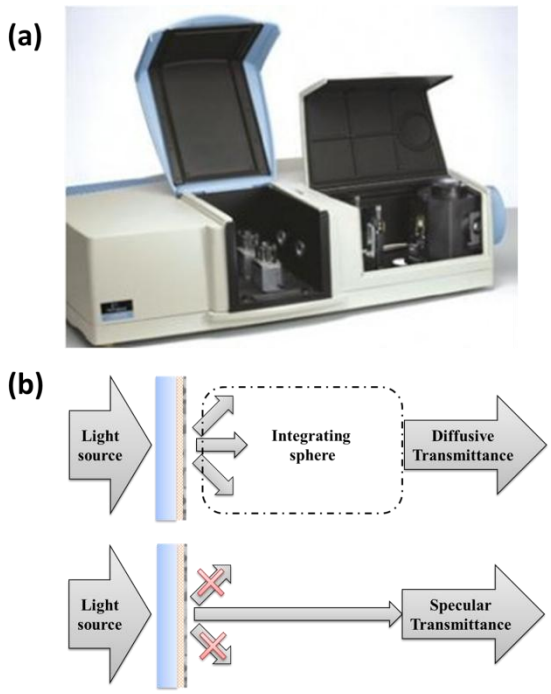

Figure 4.2. (a) Lamda 950 optical transmittance measurement, (b) The difference between diffusive transmittance and specular transmittance.

4.5. Electrical measurements

In Figure 4.3, the sheet resistance of thin film in current study was measured by 4 points method. A current is passed through the outer probes and induces a voltage in the inner voltage probes. Using the voltage and current readings from the probe, equation (1) shows the calculations of thin film sheet resistance[54]:

$$\rho_{\mathrm{sq}}\left(\frac{\Omega}{sq}\right) = \frac{\pi}{ln2}\frac{V}{I} \qquad \text{Eq 4.1}$$

However, it need to be aware of that this equation works when the film thickness less than half the probe spacings (t < s/2)[55]. In current series sample measurements, the

nanomaterial stacks are less than 2 μm thick, which is far smaller comparint to Jandel four points probe spacings (500 μm). If adding a magnetic field, the hall mobility and carrier concentration also could be calculated according to Hall Effect.

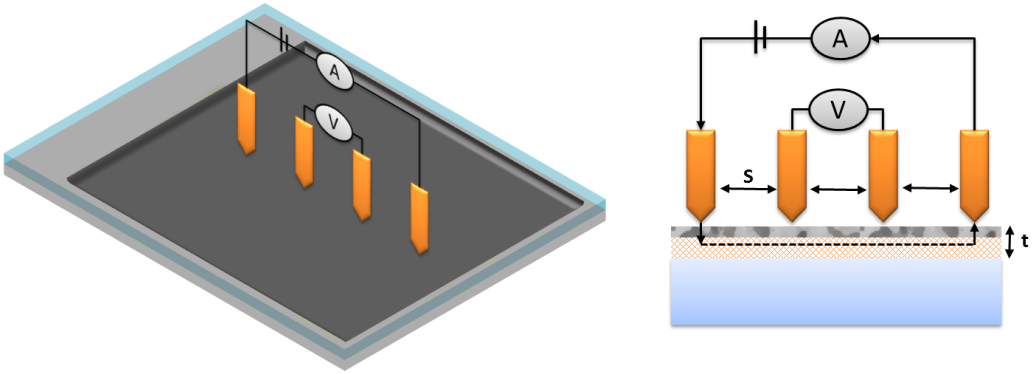

Figure 4.3 Thin film electrical properties measurement via four points method.

4.6. Summary of the chapter

In this chapter, the materials characterization techniques used in this research are summarized and briefly reviewed.

CHAPTER 5. LASER ENHANCED AZO COATING

5.1. The case of high vacuum deposited AZO film

5.1.1. Introduction

Al doped ZnO (AZO) is currently under intense investigation and development to replace indium tin oxide (ITO) as a transparent conductive coating. AZO thin films exhibit high electro-optical quality, sufficient material availability, environmental benefits, and low cost to manufacture[43, 56, 57]. Meanwhile, the good electro-optical properties and reliability of AZO films lead to wide applications in display windows[30], thin film solar cells[16] and optoelectronic devices[33] such as transparent thin film transistors. Various deposition techniques are applied to fabricate AZO films, such as sputtering, evaporation, chemical vapor deposition, spray pyrolysis, cathodic arc deposition, atomic layer deposition (ALD) and pulsed laser deposition (PLD)[17, 18, 58-60], mainly operating at elevated temperatures. There are some reports of depositing AZO by low temperature PLD[61-63] for optical devices, but poor optoelectronic properties were obtained. On one hand, because extended defects like grain boundaries and inter-grain voids play an important role in the electrical properties of AZO films[13]. For instance, these defects may create energy levels in the band gap (traps) that tend to decrease the carrier lifetime so as to decrease the electro mobility[14]. In order to reduce the drawback effect of these defects, post-deposition annealing is utilized to enhance the electrical stability of the AZO film. The enhancement results from alleviating accumulated strain energy and improving crystallinity[64]. However, annealing might cause lower conductivity because of the ionization of oxygen vacancies and the oxidation of aluminum[65]. On the other hand, increasing the optical transparency in the red/IR range can be

achieved by reducing the carrier concentration; however, this is usually associated with the expense of conductivity[15]. Thus, high carrier mobility and low carrier concentration are desired for simultaneously outstanding conductivity and transparency. Some methods are now being developed to relax this conductivity/transparency trade-off by increasing the carrier mobility[15, 66]. In this section, AZO films were deposited on sapphire substrates by room temperature PLD. Then low temperature annealing and UV laser crystallization (UVL) were combined to achieve high carrier mobility for improving the conductivity and transmittance, aiming to relax conductivity/transparency trade-off.

5.1.2. AZO film deposition and laser processing

5.1.2.i. Pulsed laser deposition

The AZO film coating were carried out via room temperature pulsed laser deposition (PLD). Before deposition, a 50.4 mm diameter, 0.33 mm thick, (0001) orientation sapphire substrate was cleaned by acetone, methanol, and DI water in an ultrasonic cleaner for 5 minutes each, sequentially. Then the sapphire substrate was put into a high vacuum chamber with a base pressure of 4.0×10^{-6} Torr. In this chamber ZnO (99.99%) and 2% Al_2O_3-doped zinc oxide (AZO) targets with 50 mm diameters were ablated by a KrF excimer laser (λ of 248 nm with τ of 25 ns). The target-substrate distance was fixed at 80 mm. Targets and substrates rotated at 7 and 5 RPM, respectively. A 50nm thick *i*-ZnO film was deposited on the sapphire substrate at laser fluence of 1.5 J/cm^2, repetition rate (RR) of 10 Hz for 20 minutes, and then 200nm thick Al-ZnO was deposited at laser fluence of 0.5 J/cm^2, RR of 5Hz for 90 minutes. Finally a 250nm thick AZO film was deposited at laser fluence of 0.5 J/cm^2, RR of 5 Hz for 90 minutes. O_2 pressure was set to

be 150 and 1 mTorr for *i*-ZnO and AZO films, respectively. Figure 5.1 represents the FE-SEM surface morphology of the AZO film as-deposited by PLD, contains inter-grain defects like voids, gaps, and grain boundaries, exhibiting inhomogeneity and discontinuity[29, 43]. The investigation of grain size is also characterized by observing grain size distribution as shown in insets of FESEM images, with an average size of ~35nm (diameter).

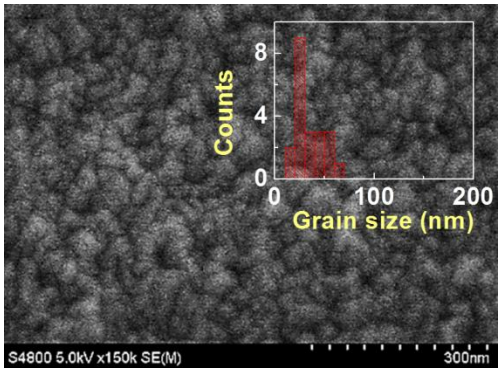

Figure 5.1. SEM images of as deposited AZO film by PLD. The inset is the grain size distribution histogram.

5.1.2.ii. UV Laser processing

Then, as-deposited samples were transferred into a 10mTorr vacuum chamber for UV Laser treatment. The laser was used with RR of 10 Hz and laser beam shaped to a square, top-hat profile (8x8 mm). The sample was placed on a motorized hotplate stage (kept at 500K) which enabled translations along both X and Y-axes as shown in Figure 5.2a. Laser fluence applied ranged from 120 to 200mJ/cm^2 with exposure time 2.5 to 5μs. After Treaement, field emission scanning electron microscopy (FE-SEM) and X-ray

diffraction pattern (XRD) were used to observe the film morphology and crystallinity. Electrical resistivity, carrier mobility and carrier concentration were measured by the Hall Effect with the Van der Pauw method. Optical transmittance was measured by ultraviolet-visible-IR spectrometer. Optoelectronic measurements would be discussed in next few parts.

Figure 5.2b, c and d show the plane-view FESEM surface morphology of the AZO film as-deposited by PLD, and processed by UV laser (120mJ/cm^2 and 160mJ/cm^2) for 5μs exposure time. It can be seen in Figure 5.2b that the as-deposited AZO film contains inter-grain defects like voids, gaps, and grain boundaries, exhibiting inhomogeneity and discontinuity[29, 43]. Comparing to Figure 5.2c, when laser is applied to AZO film with fluence of 120mJ/cm^2 for 5μs, facetted grains are getting to form and impinge with each other, achieving compact and continuous surface, suggesting film quality and crystallinity have been significantly improved[13, 29]. Figure 5.2c subject to UV laser with higher fluence of 160mJ/cm^2 for 5μs exposure shows similar surface morphology such as good film homogeneity and surface flatness. Whereas, the facetted grains with boundaries become more apparent, since more thermal energy is delivered for thorough crystallization.

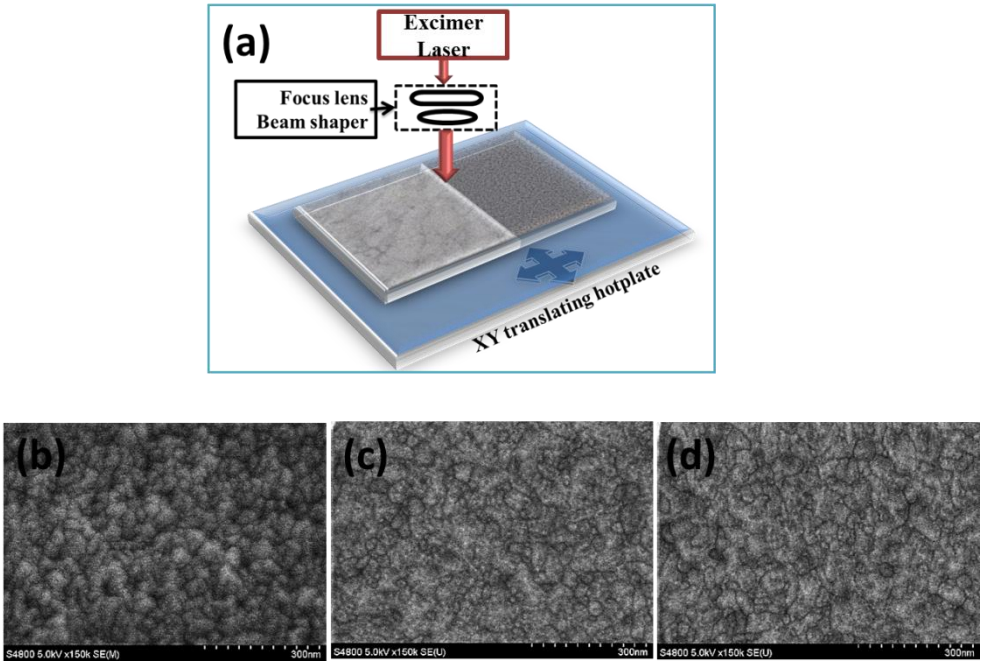

Figure 5.2. (a) laser processing set up, (b) As-deposited AZO film by PLD, and AZO film processed by laser processing (at 500K): (c) 120mJ/cm2, 5μs, (d) 160mJ/cm2, 5 μs.

5.1.3. Microstructure change after laser processing

5.1.3.i. Grain growth induced by laser crystallization

Not only grain shape change but also grain growth is detected. The investigation of grain growth is carried out by observing grain size distribution as shown in figure 5.3. It can be observed that higher laser fluence results in better grain growth. In most of the cases grain size distribution is bimodal. There is a swift transition of smaller grains into larger grains dominant. On the other hand, at laser fluence higher than the optimum threshold (160mJ/cm^2) window though, there is a clear-cut grain growth as compared to the as-deposited film. Film lack long range crystalline order, as higher laser fluence like 200mJ/cm^2 causes ablation of material[42, 67] , that is, laser evaporated material would

redeposit back on the surface but no crystallization energy is available for them, so that resultant surface would lack crystallinity.

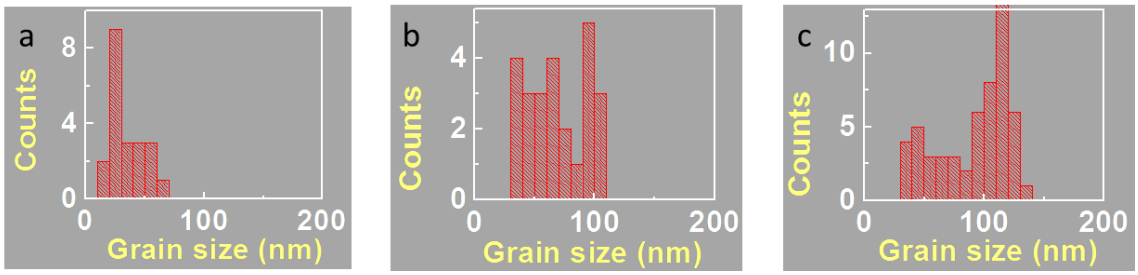

Figure 5.3. (a) Grain size distribution of As-deposited AZO film by PLD; and grain size distribution of AZO film processed by LASER PROCESSING (at 500K): (b) 120mJ/cm2, 5μs; (c) 160mJ/cm2, 5 μs.

5.1.3.ii. AZO film crystallinity enhancement

The crystallinity improvement of polycrystalline AZO film processed by laser was confirmed by XRD patterns, which were collected and analyzed as shown in Figure 5.4a and b. In Figure 5.4a, the diffraction peaks appearing at 34.5^{o} and 41.7^{o} correspond to (0002) peak of hexagonal wurtzite structure AZO and (0006) peak of sapphire, respectively [17, 68, 69]. It is well known that (0002) is the dominant orientation in Al doped ZnO films grown by various methods including PLD, sputtering, and CVD[43, 61]. No characteristic peaks of metallic Zn, Al, or $ZnAlO_4$ were detected, indicating that the films have highly crystalline structure with a c-axis preferred out-of-plane orientation. After laser processing, AZO (0002) peak was found to become stronger and stronger associated with laser fluence increase from 0 to 120mJ/cm^2 and finally 160mJ/cm^2. The

stronger peaks attribute to the crystallinity enhancement including a larger grain size and preferable orientation, i.e. low misalignment or tilt along the c-axis. However, laser fluence of 200mJ/cm^2 is too high, which lowers the XRD peak height, implying degraded crystallinity. And the well-known Debye-Scherrer Formula was utilized to calculate crystal sizes from the full width at half maximum (FWHM) of the XRD patterns as presented in the right column of Table 5.1. The average crystal size of AZO film increased from 25 to 32.4nm when a laser fluence of 160mJ/cm^2 and 5 μs exposure is applied. However, the clear-cut crystal size decrease was detected in fluence of 200mJ/cm^2, which is not desired.

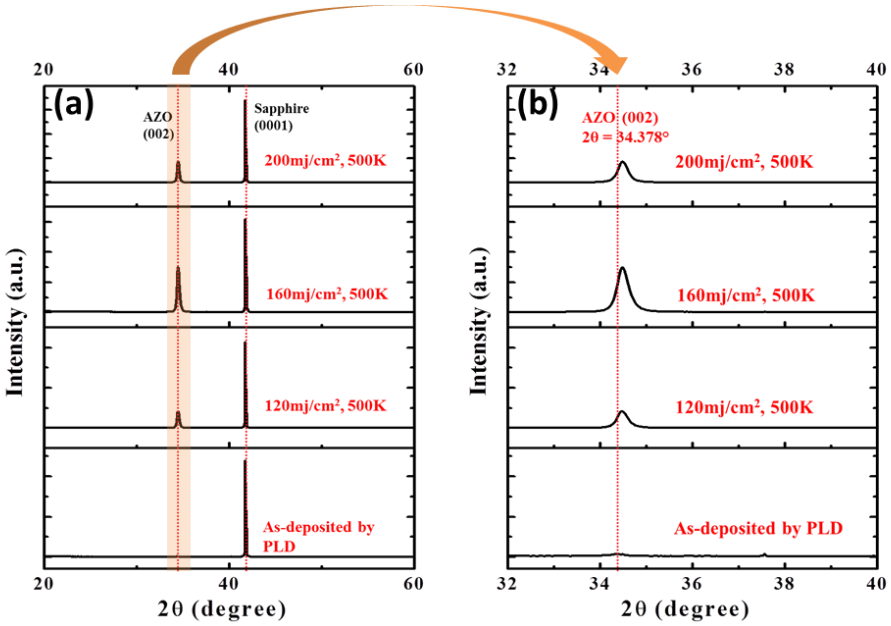

Figure 5.4. a) θ-2θ XRD patterns of AZO films as-deposited by PLD and processed by LASER PROCESSING at 120mJ/cm^2, 160mJ/cm^2, and 200mJ/cm^2 at 500K, respectively. The AZO films have a preferred (0002) out-of-plane orientation on the c-plane sapphire

substrate. b) Thermal strain introduced by LASER PROCESSING. AZO (0002) peak of the crystallized samples show 0.1^{o} high angle shift.

Furthermore, a 0.1^{o} shift to higher angle of AZO (0002) peak was detected in processed samples as shown in Figure 5.4b and Table 5.1. This upshift indicates the lattice distortion induced due to thermal strain. The strain most likely originated from the substitution of Al^{3+} for Zn^{2+} [70, 71] . For 2% Al doped ZnO film in this work, the Al^{3+} has a smaller radius (~0.05nm) than Zn^{2+} (~0.074nm), thus leading to a decrease in the lattice constant[70]. The smaller radius of the Al^{3+} brings about higher ion mobility, which drives the Al^{3+} more likely getting across the crystal boundary than Zn^{2+} in laser processing and resulting in a better crystalline orientation at AZO (0002) peak. Therefore, after laser process, the substitution of Al^{3+} to Zn^{2+} is enhanced, causing the crystallinity enhancement and the lattice constant decrease which are shown as AZO (0002) peak strengthening and upshifting in 5.4a and b.

Table 5.1. Peak Position, Full width at half maximum (FWHM) of XRD AZO (0002) peaks and grain size for as-deposited and processed AZO films

sample	Peak Position (°)	FWHM (°)	Crystal Size (nm)
As-deposited by PLD	34.378	0.328	24.9
120mJ/cm², 500K	34.484	0.284	29.1
160mJ/cm², 500K	34.487	0.255	32.4
200mJ/cm², 500K	34.476	0.274	30.1

5.1.4. Performance characterization and discussion

5.1.4.i. Electrical conductance characterization

Due to crystallinity improvement after laser processing, an enhanced electrical conductance was expected. Hall Effect measurements were carried out to investigate the resistivity, mobility, and carrier concentrations each for 3 times, whose mean are shown in Table 5.2. The resistivity of as-deposited by PLD was measured to be 1.68×10^{-3} Ω-cm, but decreased to 9.90×10^{-4} Ω-cm after optimized laser processing (160mJ/cm^2, 5μs) exposure at 500K. This reveals laser processing coalescences a few small crystals into larger ones and reorganizes the facetted grains into a compact and homogenous film which decreases the internal defects density that influences polycrystalline AZO film conductance [19, 29, 43, 65].

Table 5.2. Electrical Properties of n-type AZO films as-deposited and processed by laser

AZO films	Method	Thickness	Mean Resistivity (Ohm*cm)	Mean Hall mobility (cm2/Vs)	Mean Carrier density (cm-3)
As-deposited	This work(PLD (RT))	200nm	1.68×10^{-3}	6.7	$5.5\times10^{+20}$
160mJ/cm^2, 2.5μs	This work(500K)	200nm	9.92×10^{-4}	19.5	$3.2\times10^{+20}$
160mJ/cm^2, 5μs	This work(500K)	200nm	9.90×10^{-4}	79.0	$7.9\times10^{+19}$
200mJ/cm^2, 5μs	This work(500K)	200nm	1.87×10^{-1}	9.9	$3.4\times10^{+18}$

To understand the conductance enhanced by laser processing, Hall mobility and carrier concentration of AZO films subject to as-deposited and processed by optimized fluence (160mJ/cm^2) with 2.5 μs and 5 μs exposure are analyzed. It is found Hall mobility increases from 6.7 to 19.5 and 79 cm^2/Vs after 2.5 μs and 5 μs exposure. While the carrier concentration decreases from $5.5\times10^{+20}$ to $3.2\times10^{+20}$ and then $7.9\times10^{+19}$cm^{-3}. Carrier concentration decrease is caused by un-equilibrium and low-oxygen laser

processing process that produces zinc vacancies that then capture excited electrons from the Al dopant and thus lower the carrier density[72]. However, polycrystalline Hall mobility μ_{hall} depends on intragrain mobility μ_i or grain boundary mobility μ_g, usually dominated by ionized impurity scattering or grain boundary scattering, according to different carrier concentrations[15, 19, 20, 73]. Equation 5.1 shows the relationship, neglecting neutral impurity scattering, lattice vibration scattering and intragrain cluster scattering[73].

$$\frac{1}{\mu_{hall}}=\frac{1}{\mu_i}+\frac{1}{\mu_g} \qquad \text{Eq 5.1}$$

For the relative high carrier concentrations ($>2\times10^{20}$ cm^{-3}), it is generally agreed that mobility is dominated by ion impurity scattering, explaining that Hall mobility increase from 6.7 to 19.5 cm^2/Vs mainly due to carrier concentration decrease that diminishes ion impurity scattering[19, 20]. However, for relative low carrier concentration ($7.9\times10^{+19}cm^{-3}$) after laser processing, the dominant factor is grain boundary scattering, which depending on grain boundary density and energy potential barrier (Φ_B) at grain boundaries[20, 74]. To describe μ_g, Seto and Baccarani [75, 76] extend Petriz model [77] as presented in equation 5.2.

$$\mu_g=\mu_0 \exp\left(-\frac{\Phi_B}{kT}\right)=\frac{eL}{\sqrt{2\pi m^* kT}}\exp\left(-\frac{e^2 {N_t}^2}{8kT\varepsilon\epsilon_0 N_{eff}}\right) \qquad \text{Eq5.2}$$

where L is the grain size, N_t is the electron trap density at grain boundaries, N_{eff} is the free electron concentration, m^* is the electron effective mass, $\varepsilon\epsilon_0$ is the static dielectric constant and e is the elementary charge. After laser processing, grain size L is enlarged, with an increase factor of ~2 times according to Figure 5.3 histograms, which does not

match the significant mobility increase from 6.7 to 79 cm^2/Vs. Thus, electron trap density N_t should have been lowered to achieve high mobility. It is well known extended defects like inter-grain voids, gaps and grain boundaries might form electro traps at grain boundaries[13]. laser processing forms facetted grains that impinge with each other to achieve compact structure, significantly lowering the internal defect density and contributing to electron trap density decrease. In addition, prior reports[15, 21] also state that UV light exposure is capable to desorb oxygen species at grain boundaries, which help decrease electron trap density as well. Both enlarged grain size and decreased electron trap density contribute to Hall mobility enhancement at low carrier concentration.

To demonstrate the performance boost by laser processing, electrical property of processed AZO film (red curve) is compared with prior advancements[78-86], as shown in Figure 5.5, that is, electron mobility vs. free electron concentration data for AZO thin films deposited by different research groups. It is well known as free carrier concentration increases over $2\times10^{+20}$ cm^{-3} in polycrystalline AZO films, the traps between grains can be partially or completely filled, reducing the barrier height and width, and thereby increasing Hall mobility. However, for relative low carrier concentration, grain boundary scattering modification would play dominant role in Hall mobility enhancement. When carrier density of $7.9\times10^{+19}$ cm^{-3} is fixed, laser processed AZO film obtains higher carrier mobility than previous reports, indicating diminishing grain boundary barrier or decreasing grain boundary density. Additionally, grain boundary density also could be affected by film thickness which would further influence the carrier

mobility [15]. Considering the 200nm thick film in our work is thinner than prior advancements, laser processing has potential to achieve even higher hall mobility.

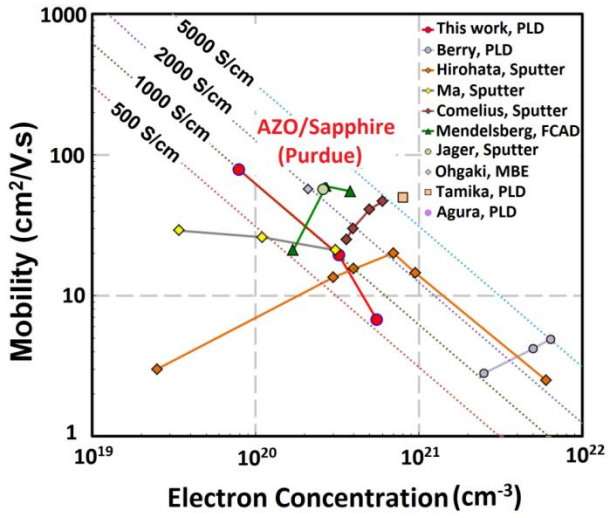

Figure 5.5. Electron mobility vs. electron concentration for AZO films as-deposited by PLD and processed by UVL, comparing with nine research groups. The red curve shows current work, the other marked points and curves represent high mobility AZO films fabricated by other research groups. The diagonal dashed lines show constant conductivity on a log-log scale.

5.1.4.ii. Optical transmittance

It has been proven that high Hall mobility is necessary for relaxing the conductivity/transparency trade-off, that is, increasing the transparency in the red/IR range can be readily achieved by reducing the impurity doping level, whereas, without expense of conductivity[15]. High Hall mobility help perform satisfied electrical conductance even at low impurity doping level. The transmittance spectra of processed

samples on sapphire were collected to compare with as-deposited ones as shown in Figure 5.6. As observed, the transmittance of as-deposited film decreases in the near IR region (750-1500 nm) because of increasing reflectance and free carrier absorption[87]. While, laser processing dramatically enhances the Red/IR transmittance in the wavelength range of 750-1500 nm for processed samples as shown in Figure 5.6a. The enhanced Red/IR transmittance attributes to decreasing reflectance and free carrier absorption, resulting from improved film flatness and diminished carrier concentration[88]. The laser beam with all three fluences shows the capability to boost up Red/IR (700-1500nm) transmittance. Among which, the electrically optimal condition with fluence of 160mJ/cm^2 achieves the strongest enhancement in IR transmittance: over 21% average transmittance increase in the wavelength range 900-1500nm, subject to significantly decreased carrier concentration. In order to further demonstrate the feasibility of optimally processed sample as an infrared transparent conductor for windows and optoelectronic devices, Mid-IR transmittance measurements from 350-8000nm were conducted as shown in Figure 5.6b. It is found that in the near IR (NIR) to mid wave IR (MWIR) region (900-5000nm), the average transmittance increase of 36% is achieved under 160mj/cm^2, implying a decreased internal defects level and reduced free carriers[88]. This transparency improvements are associated with decreased carrier concentration, but increased Hall mobility, thus slightly decreased sheet resistance (from 67Ω/sq to 40 Ω/sq), without any expense of conductance, which relaxes the conductivity/trenchancy trade-off[15]. And considering light absorption of sapphire, the sole AZO film of current series of samples can achieve even higher transparency, which is comparable or higher, as compared with previous literatures[87-91].

However, too high fluence like 200mJ/cm^2 reduced the film conductance back to a low level (Figure 5.6b), demonstrating that extra thermal energy beyond optimal fluence degrades the film quality, though the Mid-IR transmittance is dramatically increased over 60% to 6000nm wavelength (grey curve in Figure 5.6b) due to intensively decreased carrier concentration. In short, optical interference effects in these thin films change the transmittance at shorter wavelengths. As shown in Figure 5.6a, the transmittance minimum shifted from 78.2% at 490 nm to 76.5% at 590 nm because the film became denser with fewer voids after laser processing. One the other hand, the shift to a longer wavelength and the greater difference between the peak and valley transmittance in the processed film indicate the higher index of refraction and lower free carrier absorption than the as-deposited film. The peak transmittance is equal to that of the sapphire substrate indicating very low absorption loss for $450 < \lambda < 1100$ nm in the laser processed samples.

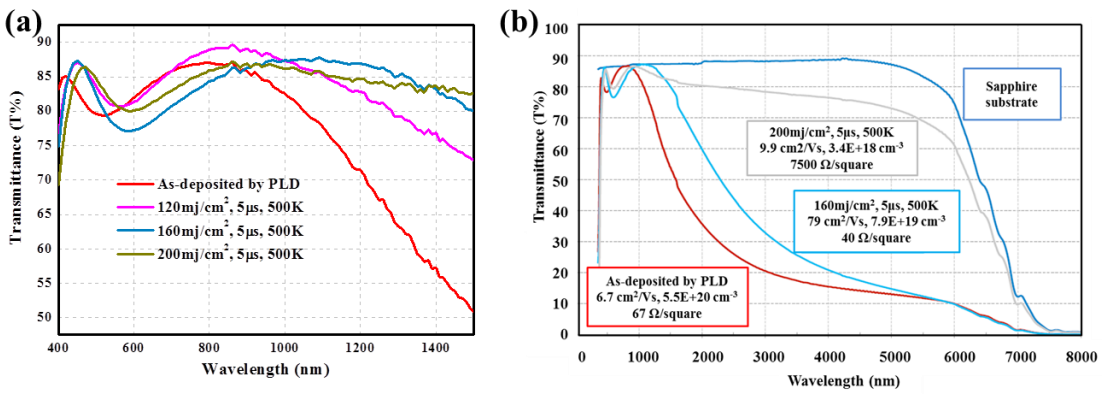

Figure 5.6 (a) Effect of laser crystallization conditions on UV to near IR transmittance spectra of AZO films; (b) UV to mid wave IR transmittance spectra of uncoated sapphire

substrate and AZO films deposited by room temperature PLD (R_S = ~67 Ω/square) and processed by UVL (R_S = ~40 Ω/square and ~7500 Ω/square).

5.1.5. Summary of this section

In sum, transparent and conductive AZO films were deposited by room temperature PLD and processed by UV laser. This laser processing technique is able to produce AZO films with high Hall mobility of 79 cm^2/Vs, and low carrier concentration of $7.9 \times 10^{+19} cm^{-3}$, relaxing conductivity/transparency trade-off. The near to mid IR range transmittance from 900-5000 nm of this UVL processed AZO film (R_S = 40 ohms/square) was dramatically enhanced, around 36% higher than as-deposited AZO (R_S = 67 ohms/square).

5.2. UV Laser Crystallization of Solution Based AZO Nanoparticles Ink

5.2.1. Introduction

AZO is currently under fast development and extensive application to replace indium tin oxide (ITO) as TCO film[27], though latter one is the standard compound for most devices performing best optoelectronic property[21]. Since it is crucial that AZO ensure a sustainable supply of the earth abundant and cost-effective alternatives. This is reflected in predicted markets of $925 million in 2016 for alternative TCOs[28]. Meanwhile, AZO thin films also exhibit impressive and reliable optoelectronic performance and environmental benign[21, 29], leading to wide installment in smart windows[21, 30], screen displays, photovoltaic cells[31, 32], and other optoelectronic devices[33]. Various deposition techniques are investigated to prepare high quality

AZO film with resistivity of 10^{-3} Ω cm and visible transmittance over 85%, such as DC sputtering[16], pulsed laser deposition (PLD)[17], Atomic layer deposition (ALD)[18] and chemical vapor deposition (CVD)[15]. However, these high vacuum methods are accompanied with key issues like instrumental complexity, high investment costs and limits scalability[21], thus there is an ever-increasing demand to develop low cost non-vacuum deposition, especially for cutting edge flexible printing electronics. In this scheme, interest in solution based coating/printing and post treatment has been centered in breakthrough in the low profile fabrications. However, to the author's knowledge, AZO film with high electrical conductivity (~1000 S cm^{-1}) with transparency over 85-90% (T@550nm) on the basis of non-vacuum deposition has not been succeed yet.

In principal, AZO thin films drew incredible attention due to significant advantages such as chemical stability in reducing environments and moreover the stabilized electrical property by aluminum dopant, which brought free charge carriers and simultaneously impede the chemisorption of oxygen at surface and grain boundaries[26]. However, since these polycrystalline AZO thin film coatings contain extended defects like inter-grain voids, gaps and grain boundaries, serving as electro traps at grain boundaries being detrimental to overall optoelectronic performance[13]. For instance, these defects tend to bring free carrier scattering centers and decrease the carrier lifetime so as to drawback the carrier mobility, resulting in low electrical conductivity[14]. Although electrical conductivity can be enhanced by increasing impurity doping level, this is usually compensated at the expense of red/IR transparency[15]. Thus, carrier scattering center minimization, in low impurity doping level with low carrier concentration, become critical to optimize carrier mobility and achieve satisfied electrical conductivity, without any compromise on transparency.

In this section, the method of mediating aqueous solution grows and post UVLC was built to overcome the bottleneck. The AZO precursor paste was painted onto the Cole-Parmer glass and followed by UV Laser exposure to minimized the extended defects and improve the optoelectronic performance as shown in Figure 1a. Nevertheless, in contrast with interests focusing on the crystallization process itself, reports on the crystallization mechanism is rare and only little attention has been paid to the basic physical model. Herein, these key issues are tackled and physical model is built, which could apply to other N type oxide semiconductor oxide film thermal treatment.

5.2.2. Film preparation and laser processing

5.2.2.i. Solution Based AZO Nanoparticles Ink Fabrication

In this part, the laser processing, with confirmed capability to enhance AZO film quality, was investigated to low cost aqueous solution fabricated AZO coatings. In order to fabricate AZO thin film, the precursor solution consisted of semiconductor grade ethanol in which 0.4M of zinc acetate dihydrate [$Zn(CH_3COO)_2 \bullet 2H_2O$] was dissolved. Aluminum nitrate hexahydrate [$Al(NO_3)_3 \bullet 6H_2O$] was dissolved in an amount to yield 2% Al in relation to Zn. Diethanolamine [$NH(CH_2CH_2OH)_2$, DEA] was added at 1M ratio to the zinc acetate. The solution was heated to approximately 75 ℃ and stirred for 2 hours and allowed to cool to room temperature. The possible chemical reaction is shown below.

$$Zn(CH_3COO)_2 \bullet 2H_2O + Al(NO_3)_3 \bullet 6H_2O \xrightarrow[PH\ adjustment]{DEA} Zn^{2+} + Al^{3+} + HO^{-1} + CH_3COO^{-1} + NO_3^{-1}$$

$$\xrightarrow[475°C\ convertion]{heating\ to\ 75°C} \text{AZO precursor}$$

Then, soda lime glass slides were used as substrates for precursor coating. The slides were sectioned into pieces each with approximately 2.5 cm^2 area. These pieces were then cleaned with deionized water and isopropanol and dried using an air gun with purified air. These substrates, one at a time, were then loaded into a Laurell WS-650 spin coater with an automatic dispenser unit. The precursor solution was dispensed onto each substrate 8 successive times with the substrate spinning at 500 rpm for dispensation and then 3000 rpm for drying. After each layer dispensed, it was evaporated and annealed on a hot plate at approximately 475℃ to convert each precursor layer to AZO. After all 8 layers achieved, the substrates were placed in a tube furnace and heated in argon with 2% hydrogen gas for 2 hours. The process map of the nanoparticles fabrication and coating is shown below in Figure 5.7.

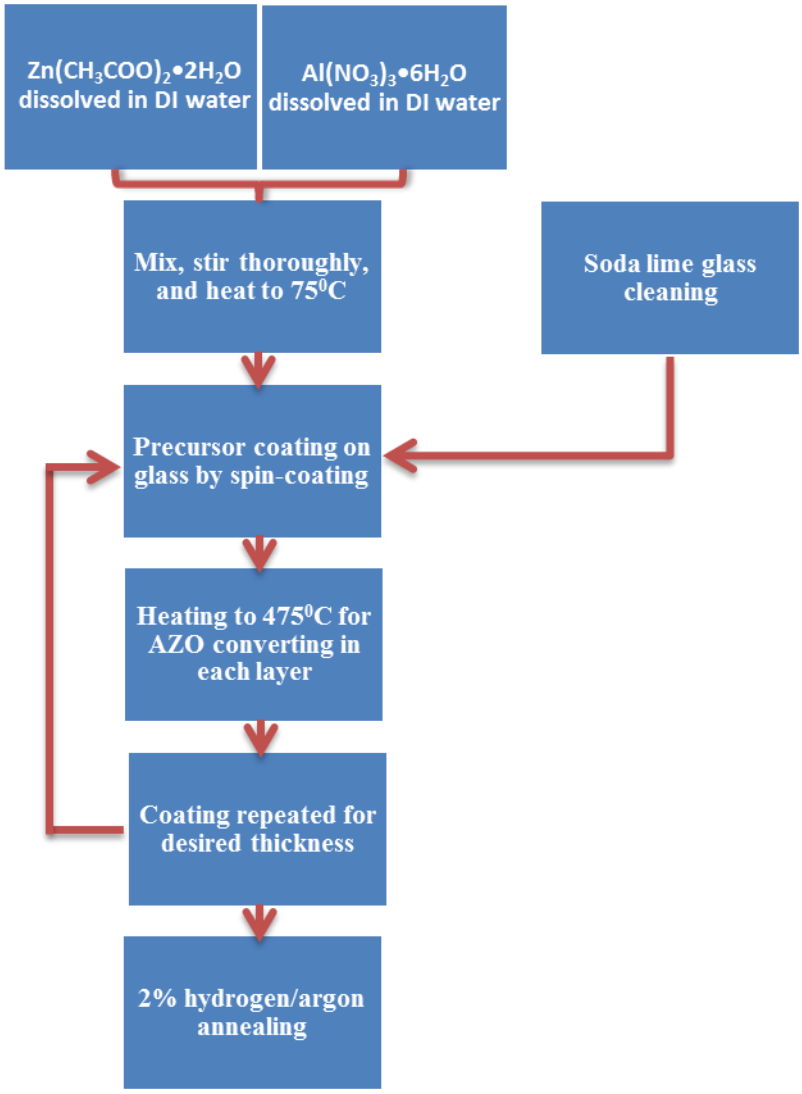

Figure 5.7. Process map of sol-gel AZO nanoparticles ink fabrication and coating

5.2.2.ii. Low cost AZO film coating

Not only sol gel AZO precursor but also AZO nanoparticles (commercial) are used to fabricate the low-cost AZO thin film. Spin coated layers were deposited on soda lime glass by two methods. The first method used typical Sol Gel chemical precursors (run#12 and 14) as found in the literature[92], while the second method involved spin coating

AZO nanoparticles dispersed in an appropriate solution (run #13). After precursor coating, the substrate were heated to evaporate the solvent and/or liquid dispersant and the Sol Gel layers were additionally heated to convert the remaining solid precursors after evaporation to AZO. A layer thickness of 300-400 nanometers was deemed optimal in order to investigate the effects of laser crystallization on the aqueous solution fabricated AZO layers. A ~ 2% Al:Zn molar ratio was used for the Sol Gel layers and the AZO nanoparticles had 2% Al_2O_3 by weight which also equates to ~ 2% molar ratio. Figure 5.8 shows the morphology of Sol Gel layers versus AZO nanoparticle layers coated on glass substrate.

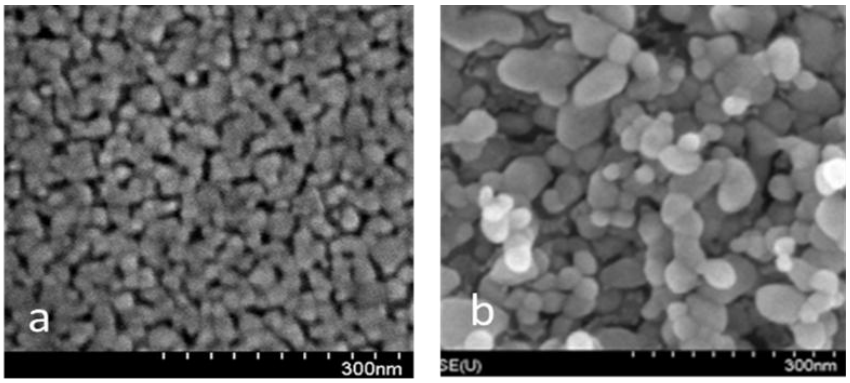

Figure 5.8. SEM top view of Spin coated AZO layers: a. Sol Gel layer b. Nanoparticle layer

As is clearly evident the Sol Gel films are denser, more uniform, and have smaller average grain size. This is further evidenced with cross section SEM images comparing Sol Gel samples (Figure 5.9). The UV laser crystallization performance of each layer will be discussed in next section.

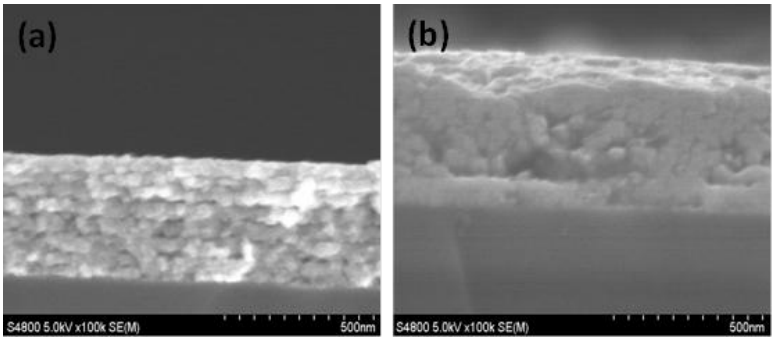

Figure 5.9. SEM cross-section view of Spin coated AZO layers: a. Sol Gel layer b. Nanoparticle layer

5.2.2.iii. AZO coating quality Characterization

X-ray diffraction (XRD) was performed and shown in Figure 5.10 on both the Sol Gel layers (run#12 and 14) and nanoparticle layers (run#13) to confirm that the zinc oxide wurzite hexagonal phase was formed and to give a further indication of the morphology of the layers. XRD for both the Sol Gel layers and the nanoparticle layers shows predominate (100), (002), (101) peaks indicating a random grain orientation, but what is also clearly seen is that the Sol Gel layers have a higher (002) peak indicating a more pronounced orientation in the c-axis than the nanoparticle films.

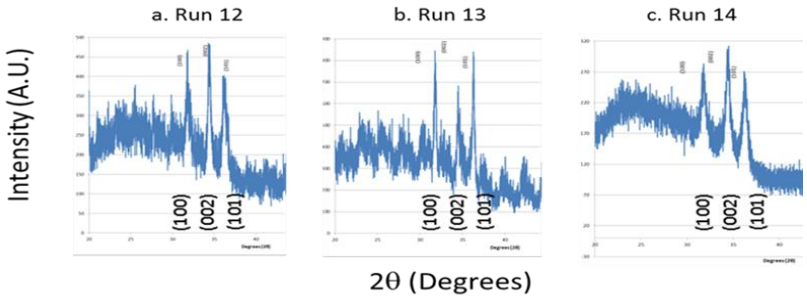

Figure 5.10. XRD of AZO film fabricated via spin coating of aqueous solution precusurs.

Mobility and Sheet resistance from several samples from each run number was performed by room temperature Hall Effect and listed in Table 5.3. The mobility and sheet resistance is typical of spin coated layers on soda lime glass substrates seen in the literature. The mobility and resistivity of untreated spin coated and other printed AZO or ITO films is typically 10X and 50X lower, respectively, than what is required for transparent conducting films for the touch panel market.

Table 5.3. Room temperature Hall measurement of spin coated precursor layers

Sample #	**12-2B**	**12-2C**	**12-2D**	**13-2B**	**13-2C**	**13-2D**	**14-2B**	**14-2C**	**14-2D**
Mobility ($cm^2/V*s$)	1.36	2.14	1.66	2.06	3.94	2.07	0.908	2.34	1.32
SR (ohms/square)	2109	1643	1917	1762	931	1421	1101	1159	1824

5.2.2.iv. AZO coating laser processing

In order to evaluate the effect of the UV Laser processing on AZO films, surface modification was observed by the top view FESEM images, before and after UV Laser processing, as shown in Figure 5.11. Figure 5.11a and c shows the plane-view FESEM images of the AZO film (sol gel layer and nanoparticle layer) before UV Laser crystallization, while (b) and (d) shows the sample after treatment, respectively.

It can be seen from Figure 5.11a and c that the as-coated AZO films ((a): sol-gel layer; (c): nanoparticle layer) exhibit loose film structure with plenty of defects like voids, gaps, and grain boundaries, inhomogeneous and discontinuous [29, 43]. However, the small grains grew to large size and became facetted with apparent grain boundaries when UV

Laser was delivered to the AZO film with intensity of 172mJ/cm^2. The small grains grew by melting, merging, crystallizing, and finally impinging to each other, when homogeneous and continuous film quality was achieved, these processes were also discussed in the section 3.2.4. Apparently, large grains formed would lower the grain boundaries density for the same AZO film area. On the other hand, since the nanocrystal shape changed to facetted and impinged with each other, the inter grain defects like voids, gaps and discontinuity decreases, which originally may create energy levels in the band gap that tend to trap the free carriers and decrease their lifetime, causing high film resistivity [14]. Both lower grain boundary density and less grain boundary traps are able to boost the grain boundary mobility which contribute to and could be dominant for polycrystalline AZO thin film mobility [15, 19, 20]. Although the plane-view images show significant improvement of AZO crystallinity, cross-section images should be taken to investigate the film crystallization depth which will be shown in next section.

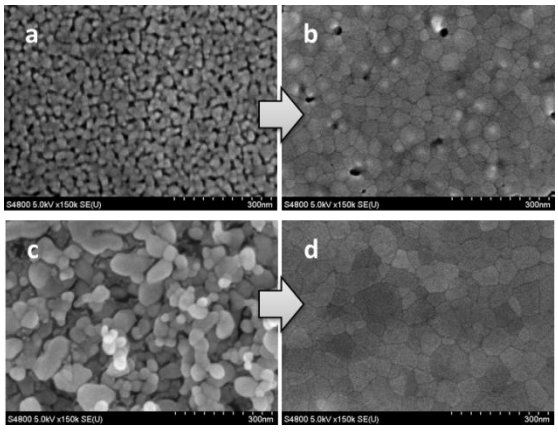

Figure 5.11. SEM plane view of Spin coated AZO layers before and after UV laser crystallization: a. Sol Gel layer; b. Sol Gel layer after UV laser crystallization; c. Nanoparticle layer; d. Nanoparticle layer after UV laser crystallization.

5.2.3. Microstructure change after laser processing

5.2.3.i. Grain growth and size distribution

The grain growth was further investigated after laser processing as shown in the Figure 5.12 grain size distribution histogram. In most of the cases grain size distribution is bimodal. There is a swift transition of smaller grains into larger grains dominant. Comparing spin coated sol gel layer before UV laser processing to afterwards, the grain size range switch from 25-75nm to 50-100 nm. The average grain size increased up to 1.5-2 times. On the other hand, for the nanoparticle layer before UV laser processing, a wide distributed grain size was obtained like dumbbell, that is, ranged 40-80nm and 110-150nm, implying a more inhomogeneous film comparing to sol gel layer. While afterwards (Figure 5.12d), a uniformly distributed grain size was achieved, ranged 60-140 nm and centered at 100nm. The average grain size increased also up to 1.5-2 times. These increased grain size and uniformed size distribution both contributed to the grain boundary density decrease as discussed above.

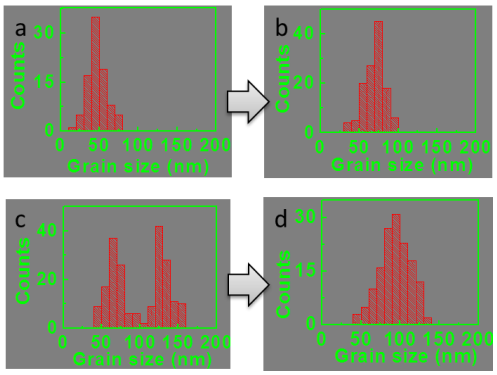

Figure 5.12. The grain size distribution histograms of AZO film: (a) sol gel fabricated AZO film before laser processing: (b) after laser process. (c) commercial nanoparticles coated AZO film before laser processing: (d) after laser process.

5.2.3.ii. AZO polycrystalline film grain growth thorough depth

Although the plane-view images show significant improvement of AZO crystallinity, cross-section images should be taken to investigate the film crystallization depth. As presented in Figure 5.13a and c, the 350nm thick AZO films were coated with sol gel layer and nanoparticle layer, respectively. While after UV laser treatment (172mj/cm^2) shown as Figure 5.13b and d, it was found that only top layer (around 150nm thick) of the AZO film was complete melted and crystallized. The bottom layer started to crystallize because of the thermal dissipation, but not completely.

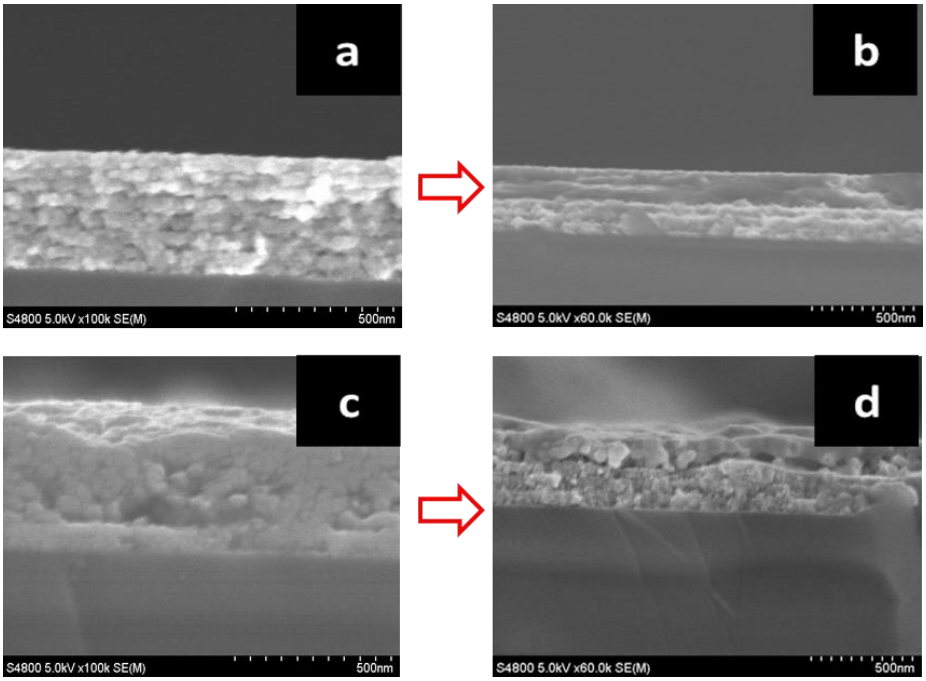

Figure 5.13. SEM cross-section view of spin coated AZO layers before and after UV laser processing: a. Sol Gel layer; b. Sol Gel layer after process; c. Nanoparticle layer; d. Nanoparticle layer after process.

The thickness of crystallized layer related with laser penetration depth and film absorption coefficient. With high film absorption coefficient to incident laser beam, the penetration depth will be low because of intensive energy conversion on the top layer. In this preliminary study, the penetration depth is around 150nm form AZO precursor layer, because of top layer absorption and particle scattering. However, the AZO film applied to touch panel displays or thin film solar cells window layers usually requires 200-300nm thick, which can be achieved by layer by layer laser processing combined with cutting edge printing techniques.

5.2.4. Performance characterization and discussion

5.2.4.i. Electrical conductance Improvement

Figure 5.14 shows the change in electrical properties of UV Laser crystallized AZO films (sol gel layer) with intensity of 172mJ/cm^2, which is optimal condition in this study, detected by Hall Effect Measurement. After UV Laser treatment, a strong decrease in sheet resistance R_s and resistivity ρ_{hall} is measured for all Laser conditions. R_s decreases from 1.5 KΩ/sq to 217, 179 and 153 Ω/sq, respectively when 50, 100 and 150 pulses were delivered to AZO film with intensity of 172mj/cm^2. ρ_{hall} decreases from 2.28×10^{-2} Ωcm to 3.26×10^{-3}, 2.69×10^{-3}, 2.30×10^{-3} Ωcm in the same way. Both of them imply the electrical conductivity has been significant improved with a factor of 10 times after UV Laser treatment. To further investigate the electrical conductivity enhancement, carrier concentration and carrier mobility of the untreated and processed films are plotted in Figure 5.14. It is can be seen that the conductivity enhancement is associate with a large increase in electron mobility, as well as a moderate increase in electron concentration of

approximately 2-3 $\times 10^{19}$ cm^{-3}. The mobility has been increased over 8 times after UV Laser treatment for the sol-gel paste fabricated AZO thin film. Under optimal Laser condition of 172 mj/cm^2 and 150 pulses, the solution based AZO thin film reach remarkably high mobility values of 18.1 $cm^2V^{-1}s^{-1}$, simultaneously keeping a high carrier concentration of 1.50 $\times 10^{20}$ cm^{-3}, and finally leading to resistivity as low as 2.30×10^{-3} Ωcm that has not been succeed before to the author's knowledge. Since carrier concentration in AZO thin film increase from 1.20 $\times 10^{20}$ cm^{-3} to 1.50 $\times 10^{20}$ cm^{-3} after UV Laser treatment, which could enhance conductivity by a factor of 1.25. This leave a conductivity enhancement factor of 8 by carrier mobility increase as mentioned above[15].

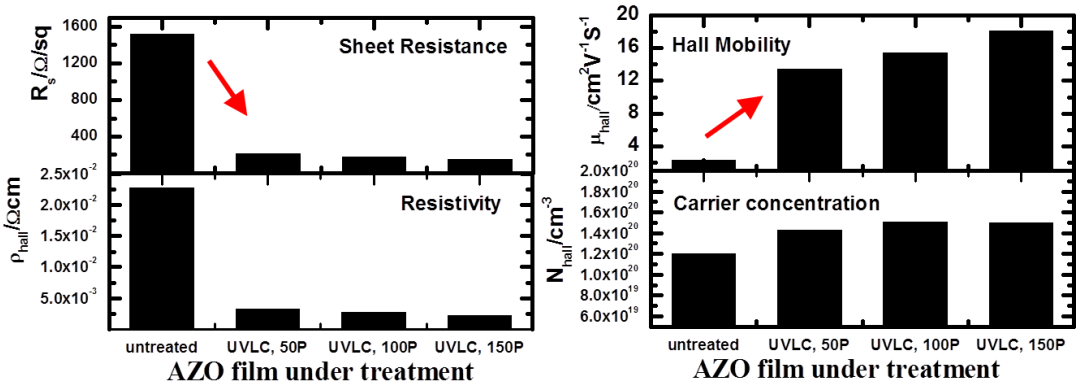

Figure 5.14. The electrical conductance of polycrystalline AZO film enhanced by laser processing: pulse number dependence of Hall measurement with optimal laser intensity of 172 mJ cm^{-2}.

According to *Delahoy et al.* [20], free carrier mobility μ_{hall} of polycrystalline AZO film would be determined by four principal scattering process include ionized impurity scattering μ_i, lattice vibration scattering μ_l, grain boundary scattering μ_g and neutral

impurity scattering μ_n, as presented in equation 5.3. While the lattice vibration scattering μ_l could be neglected at room temperature and neutral impurity scattering μ_n is also negligible since the amount of neutral impurity scattering centers is much less than that of ionized impurity [73]. So the free carrier mobility is mainly determined by ionized impurity scattering μ_i and grain boundary scattering μ_g, as shown in equation 5.1.

$$\frac{1}{\mu_{hall}}=\frac{1}{\mu_i}+\frac{1}{\mu_l}+\frac{1}{\mu_g}+\frac{1}{\mu_n} \qquad \text{Eq5.3}$$

Referring to equation 5.1 and [15, 19, 20, 93], in the polycrystalline conductive film like AZO, the hall mobility depends on intragrain mobility μ_i usually dominated by ionized impurity scattering at room-temperature and grain boundaries mobility μ_g usually determined by grain boundary density and the electron scattering intensity at grain boundaries. For the relative low carrier concentrations ($<2\times10^{20}$ cm^{-3}) in this study ($1.2\text{-}1.5\times10^{20}$ cm^{-3}), it is generally agreed that mobility is dominated by grain-boundary scattering [20, 74], which means the hall mobility of the as-coated and processed AZO film is determined by the value of grain boundary mobility μ_g according to equation 5.1 and 5.3. This also could be proved by μ_i value of 50-80 $cm^2V^{-1}s^{-1}$ at current carrier concentration ($1.2\text{-}1.5\times10^{20}$ cm^{-3}) calculated by Brooks-Herring-Dingle model [20, 74]. However, taking into account of the combined effect, the vast carrier mobility increase in figure 5.14 after UV Laser processing results from the polycrystalline film grain boundary mobility μ_g improvement from 2.42 to at least 25 $cm^2V^{-1}s^{-1}$ by 10 times.

5.2.4.ii. The decrease of electro trap density at grain boundaries

To analyze the modification on the polycrystalline AZO film grain boundary by UV Laser processing, the scheme of polycrystalline structure and energy level of AZO film was presented in Figure 5.15. As shown, during electrons flowing in polycrystalline AZO film with grain boundary scattering dominant, the grain boundary density is determined by grain size L while the scattering intensity at grain boundaries is determined by grain boundary barrier height Φ_b indicated in Figure 5.15. The latter is controlled by electron trap density (N_t) and the free electron concentration (N_{hall}). For all the thin films in current study, the product of the average grain size (~70-120nm) times the electron concentration (1.2×10^{20} cm^{-3}-1.5×10^{20} cm^{-3}) is larger than N_t (<3.0×10^{13} cm^{-2}), so that the grain are not fully depleted of their carriers[15, 19]. Then first approximation can be applied to describe the energy potential barrier at grain boundary as shown in equation 5.4 [15, 19, 20, 73], in which $\varepsilon\epsilon_0$is the static dielectric constant and e is the elementary charge.

$$\Phi_B=\frac{e^2{N_t}^2}{8\varepsilon\epsilon_0 N_{eff}} \qquad \text{Eq 5.4}$$

$$\mu_g=\mu_0 \exp\left(-\frac{\Phi_B}{kT}\right)=\frac{eL}{\sqrt{2\pi m^* kT}}\exp\left(-\frac{e^2{N_t}^2}{8kT\varepsilon\epsilon_0 N_{eff}}\right) \qquad \text{Eq 5.5}$$

Considering both grain boundary density and energy potential barrier at grain boundaries, Seto and Baccarani [75, 76] extend Petriz model [77] to describe the grain boundary mobility μ_g as shown in equation 5.5, where m^* is the electron effective mass, L is the grain size and Φ_b is the grain boundary potential (barrier height). The basic result of this equation is based on electrons transport through grain boundary by thermionic emission

over the barrier, taking into account of electron traps as a depletion region formed on either side of the grain boundary barrier. As confirmed by crystal size histogram in Figure 5.12, the average grain size "L" was increased by ~2 times which leads to an enhance factor of 2 for the grain boundary mobility according to equation 5.5. However, as calculated from equation 5.1, the grain boundary mobility has been improved by 10 times which leave a factor of 5 mainly from the electron trap density (N_t) decrease at grain boundaries. The decrease of electron trap density attributes to desorption of oxygen species at grain boundaries of UV Laser exposed sample which are in good agreement with prior reports[15, 21]. The desorption of oxygen species would release free carriers from traps which is proved by a moderate increase of carrier concentration increase after UV Laser crystallization shown in Figure 5.14.

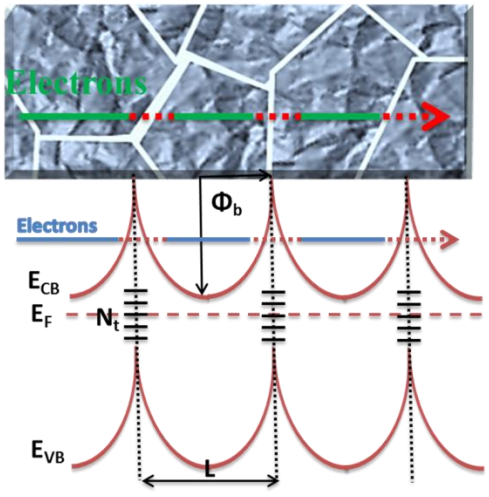

Figure 5.15. The physical model of polycrystalline AZO film structure and electrical conductance

5.2.4.iii. Laser Intensity Effect

To investigate the optimal parameters for UV laser crystallization, several series of AZO thin film coated by sol gel layer and nanoparticle layer were processed and measured by Hall measurements. The carrier mobility was used to evaluate the effect on AZO thin film quality by UV laser. The initial laser parameters of several trials were designed according to COMSOL Multiphysics® simulation shown in the prior section and experimental characterizations. Then, suitable parameters including laser intensity and pulse number were analyzed, taking into account of both carrier mobility test results and the Multiphysics simulation.

Table 5.4. UV laser crystallization parameters effect on AZO sol gel layer (run 12) carrier mobility

Sample number	Laser condition	mobility cm^2/VS
1	172mj/cm², 50pulses	13.4
2	172mj/cm², 100pulses	15.4
3	172mj/cm², 150pulses	18.1
4	192mj/cm², 50pulses	9.28
5	192mj/cm², 100pulses	12.7
6	192mj/cm², 150pulses	14.4
7	208mj/cm², 50pulses	11.5
8	208mj/cm², 100pulses	11.9
9	208mj/cm², 150pulses	3.3
10	227mj/cm², 50pulses	2.8
11	227mj/cm², 100pulses	1.66
12	227mj/cm², 100pulses	1.9

Table 5.4 shows the UV laser processing parameters effect on AZO thin film carrier mobility fabricated by sol gel layer spin coating. Apparently, laser intensity of $172mj/cm^2$

is the optimal for carrier mobility enhancement, suggesting lowest grain boundary density or electron trap density at grain boundaries [19, 20]. High laser intensity beyond optimal threshold window though, is able to degrade film quality, that is, a clear-cut carrier mobility decrease as compared to the optimal condition. Film lack long range crystalline order, as higher laser fluence causes ablation of material [42, 67] , that is, laser evaporated material would redeposit back on the surface but no crystallization energy is available for them, so that resultant surface would lack crystallinity.

Table 5.5 shows the UV laser crystallization parameters effect on AZO thin film carrier mobility fabricated by nanoparticle layer spin coating. Similarly, laser intensity of 172mj/cm^2 is the optimal for carrier mobility enhancement, suggesting lowest grain boundary density or electron trap density at grain boundaries too. However, comparing the run 13 to run 12, it can be found that nanoparticle layer AZO film performs lower carrier mobility than sol gel layer, demonstrating looser film structure for nanoparticles ink printing.

Table 5.5. UV laser crystallization parameters effect on AZO nanoparticle layer (run 13) carrier mobility

Sample number	Laser condition	13-2-H mobility cm^2/VS
1	136mj/cm², 100pulses	8
2	136mj/cm², 150pulses	10.2
3	136mj/cm², 200pulses	10.8
4	172mj/cm², 50pulses	8.82
5	172mj/cm², 75pulses	10.6
6	172mj/cm², 100pulses	10.8
7	208mj/cm², 50pulses	9.27
8	208mj/cm², 75pulses	8.16
9	208mj/cm², 100pulses	8.55
10	240mj/cm², 5pulses	6.41
11	240mj/cm², 25pulses	6.81
12	240mj/cm², 50pulses	6.00

5.2.4.iv. Pulse Number Effect

Under optimal laser intensity during UV laser crystallization, a strong decrease in sheet resistance R_s and resistivity ρ_{hall} is measured for different pulse number as shown in Figure 7. R_s decreases from 1.5 KΩ/sq to 217, 179 and 153 Ω/sq, respectively when 50, 100 and 150 pulses were delivered to AZO film. ρ_{hall} decreases from 2.28×10^{-2} Ωcm to 3.26×10^{-3}, 2.69×10^{-3}, 2.30×10^{-3} Ωcm in the same way. As discussed in prior section, it can be seen that the conductivity enhancement is associate with a large increase in electron mobility, over 8 times and 4 times after UV Laser treatment for the sol-gel layer (table 2) and nanoparticle layer (table 3), respectively. And as shown in table 5.4 and table 5.5, under laser intensity of 136mj/cm^2, 172mj/cm^2 and 192mj/cm^2, 150 pulses supply more thoroughly film modification which achieved highest carrier mobility.

Higher carrier mobility results from lower grain boundary scattering dominated by grain boundary density and electron trap density at grain boundaries. While laser intensity exceeds 200mj/cm^2, that would require pulse number less than 100 to avoid film quality degradation because of possible material ablation and insulate layer formation (Aluminum oxide) [42, 67].

5.2.4.v. Forming gas annealing

Since impurity ion scattering is still not dominant mechanism in polycrystalline AZO film after UV Laser processing in current series sample, implying further increase in carrier has a potential to enhance electrical conductivity more. Demonstrated in Figure 5.16, sheet resistance of AZO thin film could further drop from 179 Ω/sq to 75 Ω/sq after FMG (Forming gas treatment under 400 $^{\circ}$C). The sheet resistance drop and electrical resistivity decrease mainly due to the large increase of carrier concentration from 1.51×10^{20} cm^{-3} to 3.61×10^{20} cm^{-3} by free carriers release from FMG passivation oxygen species and other electron traps, without drawback carrier mobility. On the other hand, carrier mobility of AZO under UL2 (UV Laser process with 172 mj/cm^2 and 150 pulses) encounter a slight decrease from 18.1 to 17.3 cm^{2}V^{-1}s^{-1} after FMG, implying impurity ion scattering accumulate influence on carrier transport. However due to carrier concentration increase, a remarkable low sheet resistance of 79 Ω/sq is still obtained.

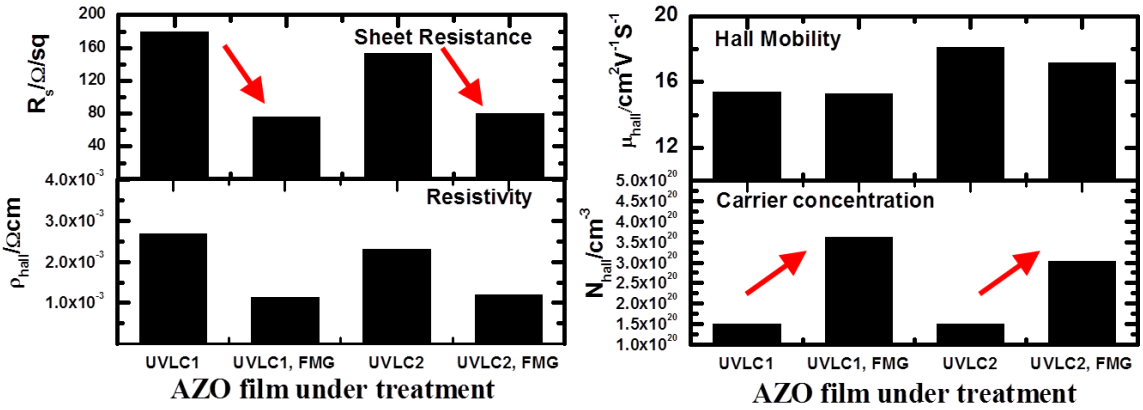

Figure 5.16, Hall measurements of AZO films processed by UV laser with following FMG.

FMG not only contributes to the release of free carriers but also desorption of oxygen species (electron traps) at grain boundaries, similarly to UV laser processing. This is crucial for film conductivity since the oxygen species (mainly oxygen and water) tends to absorb electrons to form insulation hydroxides phase, in which the absorbed electrons generate negative potential barrier at boundaries would be also detrimental for electron thermionic emission. This is illustrated in Figure 5.17a. Desorption of oxygen species after laser treatment and FMG can be further confirmed by XPS spectra as shown in Figure 5.17b and 5.17c. As compared before and after laser treatment, only a slight difference in the Zn2$p_{3/2}$ signal was observed. In contrast, the O1s signal was affected dramatically after the UV Laser exposure, where the peak with higher binding energy subject to hydroxides was diminished and shifted to lower energy typical for metal oxides. Moreover after laser and FMG, O1s signal assigned to hydroxides almost completely disappeared, leaving strong metal oxides signal. This reveals that the removing of absorbed oxygen species after AZO film aqueous solution fabrication was accomplished

by laser treatment and followed FMG, which eliminated electron traps and boosted the electron mobility and conductance[15, 21].

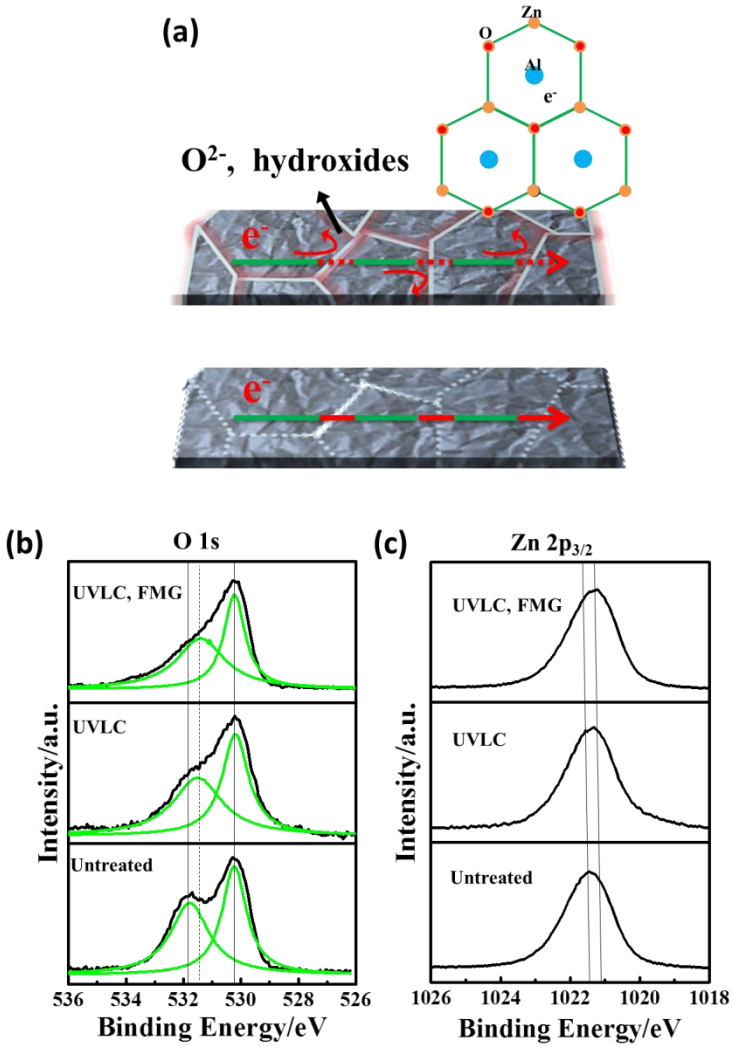

Figure 5.17. (a) Scheme of polycrystalline AZO and the electron traps formed by oxygen species at grain boundaries. The oxygen species tend to absorb electrons and form negative potential barrier. XPS spectra of AZO film before and after laser and FMG process (a) binding energy peak index to O 1s and (b) binding energy peak index to Zn $2p_{3/2}$.

5.2.5. Optical performance discussion

5.2.5.i. Transmittance

Not only electrical conductance but also transparency needs to be considered so as to evaluate the potential application of this solution fabricated AZO film like in practical touch screen display and smart window. UV-Vis-IR transmittance measurement was carried out to explore this optoelectronic performance. As illustrated in Figure 5.18a and b, the transmittance spectrum of the current series of samples in the wavelength range of 400-2000 nm were measured with Cole-Pamer glass as reference substrate. All results meet the requirements of touch screen display for practical application (R_s: 500 Ω/sq; T: 85%). For instance, the films processed by 172 mJ cm^{-2} reach 217 Ω/sq with 95% T@550nm (Figure 5.18b), 75 Ω/sq with 88% T@550nm and 79 Ω/sq with 89% T@550nm (Figure 5.18a), depending on Laser pulse number and FMG, respectively. To date, no such low sheet resistance (R_s<80 Ω/sq @ T >88%) has been reported before for the thorough solution fabricated AZO film, though combined with post treatment. This remarkable optoelectronic performance mainly attributes to the relaxing conductivity / transparency trade-off by increasing the charge carrier mobility after UV laser processing [15, 21]. On the other hand, the UV-Vis-IR transmittance exhibits a slight decrease near Vis-IR range after following forming gas annealing (FMG) process (Figure 5.18b comparing with / without FMG) owing to free carrier absorption, which is reflected in the moderate carrier concentration increase in Figure 5.16. As well as laser intensity of 192 mJ cm^{-2}, the films reach 273 Ω/sq with 96% T@550nm, 217 Ω/sq with 95% T@550nm and 95 Ω/sq with 89.4% T@550nm, depending on different Laser pulse number and FMG, respectively (Figure 5.18b).

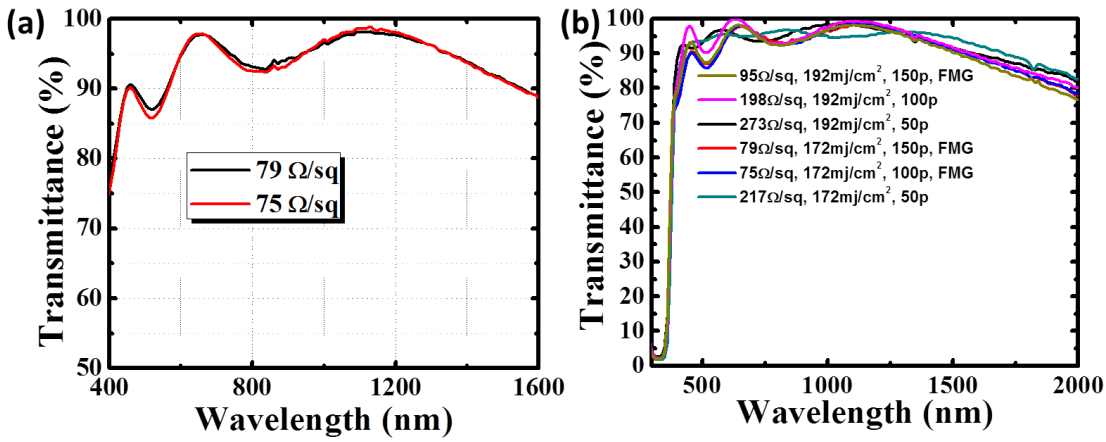

Figure 5.18. Influence of UV laser on transmittance: (a) Visible-IR transmittance spectrum of UV laser and FMG processed AZO films, (b) the transmittance measurements of variable samples processed with and without FMG.

5.2.5.ii. HAZE measurements

Figure 5.19a shows the film scattered transmittance scale evaluation setup. The light scattering was quantified by the difference between diffusive and specular transmittance (the light comes out of the sample parallel to the incident light), which also is called HAZE measurements. The diffusive transmittance was measured by an integrating sphere to integrate all forward light including both scattered and specular transmitted light. After the baseline for the UV-Vis-IR spectroscopy was set by scanning a blank glass substrate, the AZO film was installed on a solid sample holder between light source and the detector for measurement. The quantification of scattering would be required, as well as comparison to other alternatives, due to crucial role in customer experience if manufactured in optoelectronic devices like touch screens and smart windows. As

illustrated in Figure 5.19b, the current series of laser processed solution fabricated AZO film exhibit ultra-low scattering transmittance in the full visible range (400-800nm), implying macro-scale uniform and homogeneous film surface.

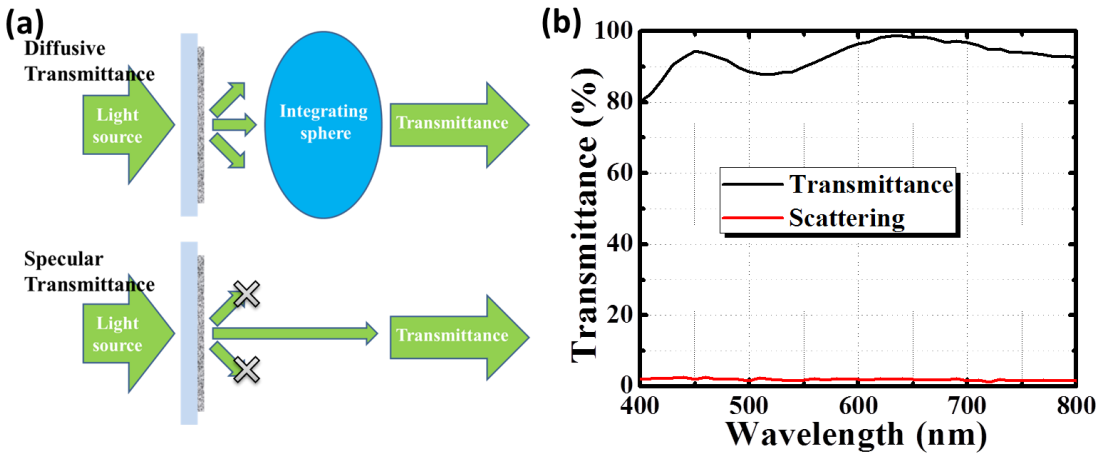

Figure5.19. (a) Light scattering measurement set up: The difference in the diffusive transmittance and the specular transmittance evaluates light scattering scale. Influence of UVLC parameters on AZO films UV-Vis-IR transmittance; (b) light scattering spectrum of processed AZO film.

Figure 5.20 shows the diffusive and specular transmittance of AZO film measured by UV-Vis-IR spectroscopy at 550nm wavelength in the same way. The difference between them are shown and compared with other transparent electrode alternatives[23, 53]. It is can be seen that the scattering of AZO film is ~1.8% after UVLC and FMG. Comparing with other alternatives like CNT (~3%), silver nanowires (~10%) and Graphene hybrid film (h3, ~6.6%), whose high light scattering scale might trigger problematic for certain displays like touch screens[23], the processed AZO film achieve significant low light scattering and lead to potential capability to compete with ITO (~1%)[23, 53].

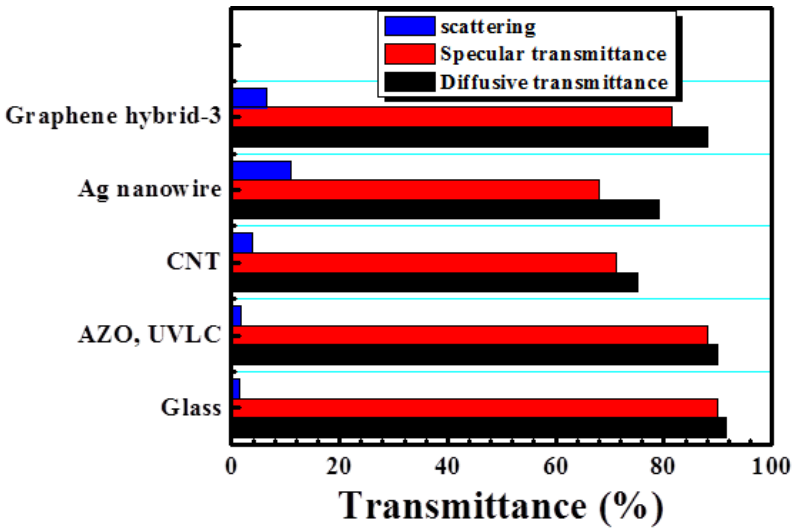

Figure 5.20. the performance of diffusive transmittance, specular transmittance and light scattering at 550nm of UVLC AZO films, comparing with glass, CNT, silver nanowires, and graphene hybrid material.

5.2.6. Summary of this section

Comparing aqueous solution fabrication in our work with other groups, the UV Laser processed AZO films exhibit high mobility (18.1$cm^2 V^{-1} s^{-1}$), implying diminishing grain boundary barrier and decreasing grain boundary density. When carrier density was increased to ~3×10^{20} cm^{-3} by FMG, the UV Laser processed AZO film obtains slightly decreased carrier mobility, indicating the charge mobility dominated by both impurity ion scattering and grain boundary barrier scattering. The highest electrical conductivity of current series of sample reaches ~1000 S cm^{-1}, which performs better than many vacuum methods. In addition, grain boundary density also could be affected by film thickness which would further influence the carrier mobility[15]. According to equation 5.5, the grain boundary density influences the grain boundary mobility with a linear factor. This

supply an explanation that charge mobility in our study is still lower than some high vacuum fabrications like FCAD and Magnetic assisted PLD. However, considering the 150nm thick AZO film in our work is extremely thinner than most prior advancements (μm scale), UV laser processing has potential to achieve even higher carrier mobility with the efficient low cost aqueous solution fabrication.

Figure 5.21a milestones the accomplished AZO film performance, comparing with experimental data for ITO thin films[10] and other recently developed transparent electrode alternatives such as CNT random meshes[94-96], silver nanowire networks[23], metal gratings[11] and graphene[53, 97]. The treated AZO films compare favorably to vapor deposited ITO and other transparent electrodes at a lower manufacturing cost due to the nature of printing technology. Figure 5.21b plots electron mobility vs. free electron concentration data for AZO thin films deposited with different process conditions from several groups[15, 21, 32, 78-86]. These prior advancements have achieved high electrical conductivity on different substrates with vacuum or aqueous solution methods, and provide a comparison with the work discussed here on our aqueous solution AZO films (red curve in Figure 3b). The highest electrical conductivity of the current series of sample reaches ~1000 S cm^{-1}, which performs better than the up-to-date best aqueous solution method[21] and many vacuum methods[15, 32, 79, 81].

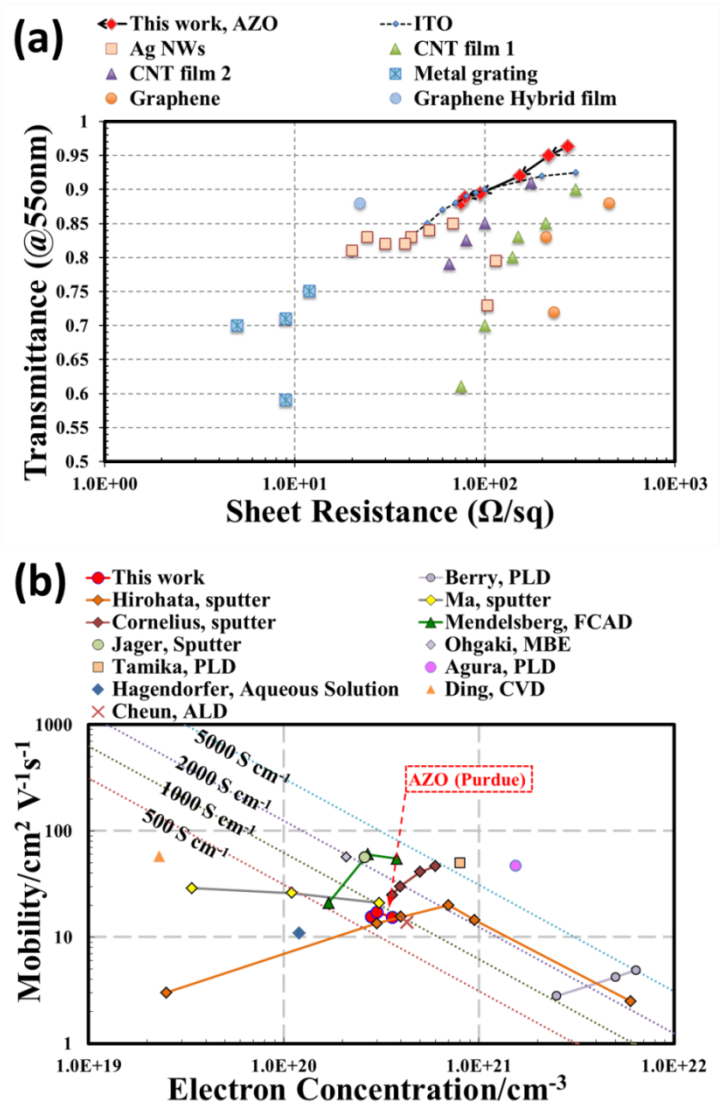

Figure 5.21. (a) The performance of transmittance at 550nm and sheet resistance for AZO films, comparing with ITO, CNT, silver nanowires, metal gratings and graphene. (b) Electron mobility vs. electron concentration for AZO films processed by UVLC and FMG, comparing with high vacuum deposition by nine research groups. The red curve shows current work, the other marked points and curves represent high mobility AZO films listed for comparison. The diagonal dashed lines show constant conductivity on a log-log scale.

CHAPTER 6. LASER ENHANCED AG NANOWIRE NETWORK PRINTING

6.1. Introduction

Being widely applied in today's ubiquitous flat panel displays and touch screen technologies, as well as thin-film solar cells and light emitting diodes, transparent and conductive electrodes (TCEs) have drawn increasing attention[98]. Various types of TCEs have been developed for these optoelectronics devices, such as indium doped tin oxide (ITO) and aluminum doped zinc oxide (AZO) which are the standard compounds for most applications performing outstanding optoelectronic property[99]. However, these oxides required high vacuum deposition, which is accompanied with issues like instrumental complexity, high cost and limit scalability[100]. This brittle metal oxide film also does not fulfill the demand of cutting edge flexible electronics. Thus, alternatives like single-wall carbon nanotubes (CNTs)[94, 96, 98], graphenes[97] and AgNWs[23] have been intensively investigated for replacement, attribute to low-cost material synthesis, scalable film fabrication and inherent flexibility.

However, AgNWs film fabrication still suffers from the problem of excessive agglomeration which would deteriorate electrical field distribution and visible range transparency, especially when AgNWs have high aspect ratio (like ~ 35 nm in diameter and ~ 15 um in lengths)[23]. Besides, for AgNWs network corresponding to transmittance of 85-95%, conduction is typically dominated by percolation through

junctions with relative large nanowire cross junction resistance (MΩ)[34, 101, 102]. A variety of attempts have been made to decrease the sheet resistance by improving the junction contacts, including self-forming of nanowires[35], thermal annealing under pressure[103] and electroplating[23]. But none of these are suitable with cutting-edge agglomeration-free roll to roll printing techniques, especially printing on low melting point PET substrate. And, it also has been challenging to reduce the sheet resistance to below 10 Ω/sq, simultaneously holding the transparency over 90%. While, UV lamp induced optical welding of AgNWs has been invented by Garnett *et al.* recently, which bring a potential for directly improving nanowire junction conductance[34]. During the optical welding, large ohmic losses of metals enable effective light concentration and serve as efficient light driven sources of heat[34] to weld crossed nanowires.

Furthermore, the illustration of rapidly raising and lowering the temperature in nanoscale metallic structures with the use of pulse laser[29, 42, 46] suggests that the optical welding, depending on material absorption and the light intensity, can be more effective and efficient if equipped with high speed and high power Laser. In addition, laser beam processing time usually ranged from nano-sceonds to micro-seconds, which is favorable for localized fusion of AgNWs without affecting other areas. This direct, efficient and selective laser processing[104, 105] could achieve high speed roll-to-roll integration of nanomaterials.

In this chapter, we investigated the ultra-fast Laser processing to assist the commercial scalable roll-to-roll printing of AgNWs on PET substrate. The printing process based on Meyer rod coating technique to deposit high respect ratio AgNWs (~35nm in diameter

and ~15um in length) network on flexible PET substrate as shown in figure 6.1. The printing line speed reaches as high as 1.5 m/min with outstanding film quality.

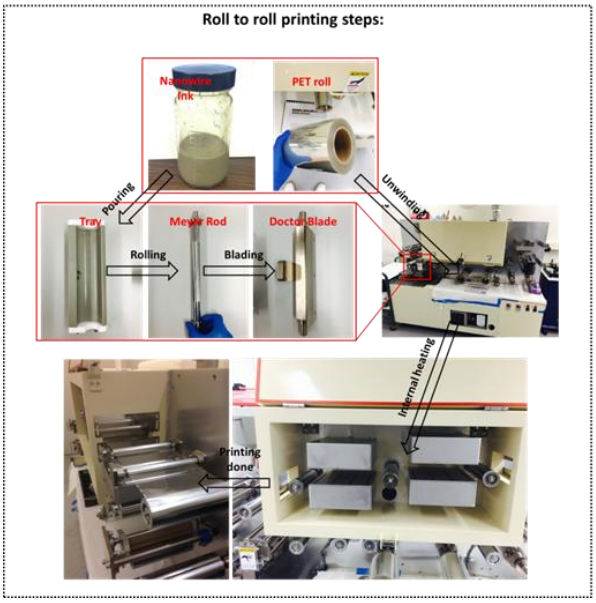

Figure 6.1. Commercial scalable roll to roll printer.

Then pulsed laser was scanning to generate local fusion of AgNW and improve cross junction contacts. Since, The controlled pulsed laser irradiation sparks off heat generation at nanowire junctions due to electromagnetic field concentration that occurs in the nanoscale gap between two crossed nanowires[34, 46]. As a consequence, thermally activated isolated silver atoms flow over nanowire junction and recrystallize to solder point. The Laser used in laser processing is shown in figure 6.2. KrF excimer laser (λ of 248 nm and τ of 25 ns) with repetition rate (RR) of 10 Hz was directed to the AgNW network to improve the cross-wire junctions. In order to efficiently process large scale film, the laser beam was shaped to a square, top-hat profile (8x8 mm) and enabled translations along both X and Y-axes. Laser intensity utilized in the welding is 20 mJ cm^{-}

^{2}, and the exposure time of each spot ranged 0.25- 3.75 μs corresponding to 10-150 pulses. The laser beam with line shape and higher repetition rate is taken into account to boost process speed even more and immediate efficient commercial scale manufacturing.

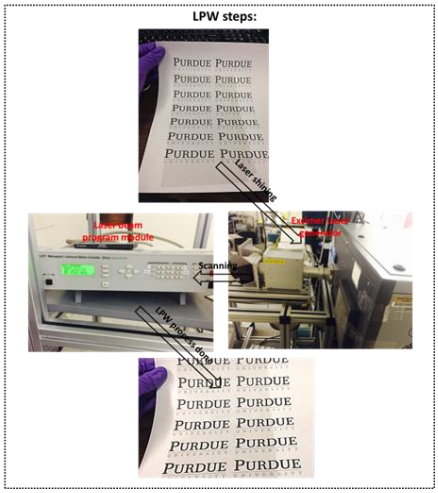

Figure 6.2. Ultra-fast laser processing set up.

6.2. Sample printing and laser processing

6.2.1. AgNW network printing

AgNW ink was bought from Blue Nano Inc., in which high aspect ratio nanowires (diameters of ~35 nm and lengths of ~15 um) were dispersed in ethanol at a concentration of 10 mg mL^{-1}. The ink dispersion was observed to be stable at room temperature and ambient atmosphere for 4 months as shown in Figure 6.3.

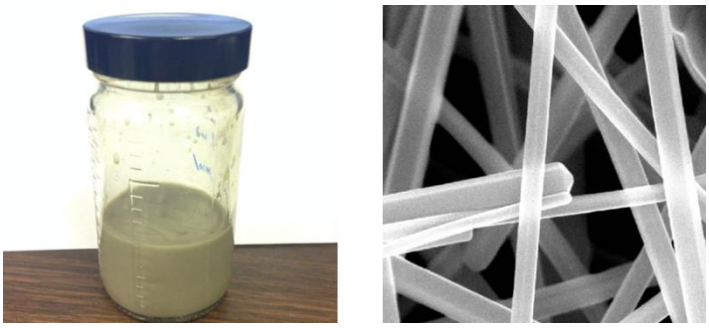

Figure 6.3. AgNW ink and the nanowire SEM images, collected from Blue Nano Inc.

To avoid agglomeration and achieve uniform printing, AgNW ink was sonicated for 5-10s and shaken by hand for 1-2 min. Figure 6.1 shows the commercial scaled Roll-to-Roll printing system. To print a film, 50ml ink is filled into tray, #30 MG gravure coater is rolled over the ink and a doctor blade is assembled to remove excess ink, leaving a uniform thin layer of AgNW ink on the PET substrate with a ~60um wet thickness. This printing system is a reverse kiss gravure coater, where the coater rotates in the opposite direction to the substrate as shown in scheme of Figure 6.4a. The kiss coating configuration minimized deflection of the substrate as it passes above the gravure coater, resulting in a small stable bead that combined with the reverse application and finally gives a very good quality and a low coating weight. The liquid thickness is determined by gravure coater rolling speed and wire distribution[106], that is, the wire diameter and the spacing as mentioned above (#30). Then, the wet coating of AgNW on PET is translated into internal heater for carefully drying at 110°C, with translating speed being 1.5 m/min as shown in Figure 6.4a. The internal heater is applied parallel to PET substrate to avoid uneven local heating, in case of coating agglomeration[23]. Figure 6.4b illustrates an 8 in. by 4 in. uniform coating of AgNWs on a PET substrate with a Purdue logo underneath.

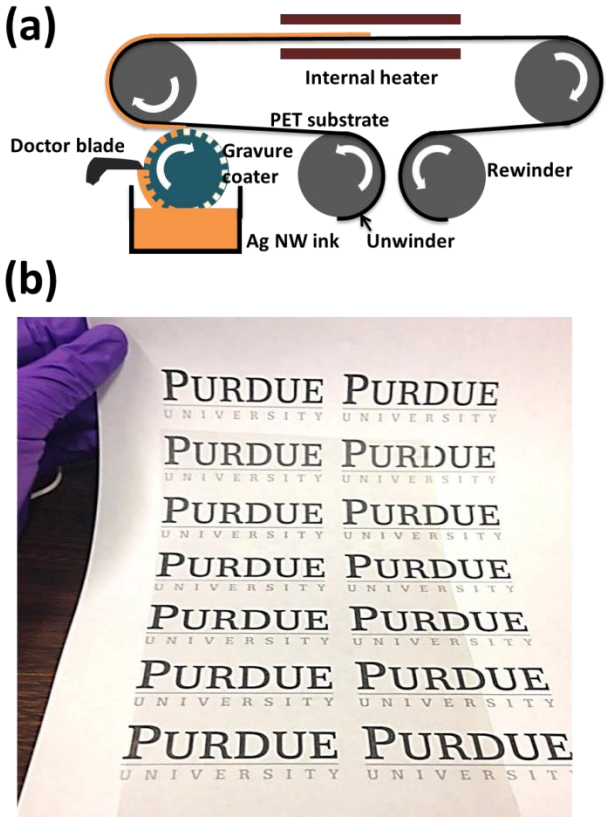

Figure 6.4. (a) schematic setup of the roll-to-roll printing system, (b) an 8 in. by 4 in. uniform printing of AgNWs on a PET substrate.

6.2.2. AgNW network surface and transparency

Figure 6.5a, b, c and d show scanning electron microscope (SEM) observation of the printing. It can be seen uniform, agglomeration-free coating of AgNWs has been achieved. According to our experiment experience and prior reports[23, 106, 107], it is found that the ink concentration play a critical role in tuning the ink viscosity optimally for uniform coatings, which performs best between 1-2.5 mg/ml. To boost the efficient manufacturing for commercially scaling up, 2.5 mg/ml concentration is applied. AgNW

films with different area densities on PET substrates could be printed, by manipulating ink concentration, wet thickness and coating area. By tuning the density higher, denoted P1 to P4, there are fewer and smaller holes in the films which contribute to better electrical field distribution and conductive performance when used in optoelectronics. The area density increase is estimated by ImageJ calculated surface filling fraction ratio (FF) as well, as shown in inserts where FF increase from 18.1% to 51.4%. As the film density decreases from P4 to P1, sparser films with more holes are obtained, which bring negative effect on electrical conduction but perform better optical transparency[108].

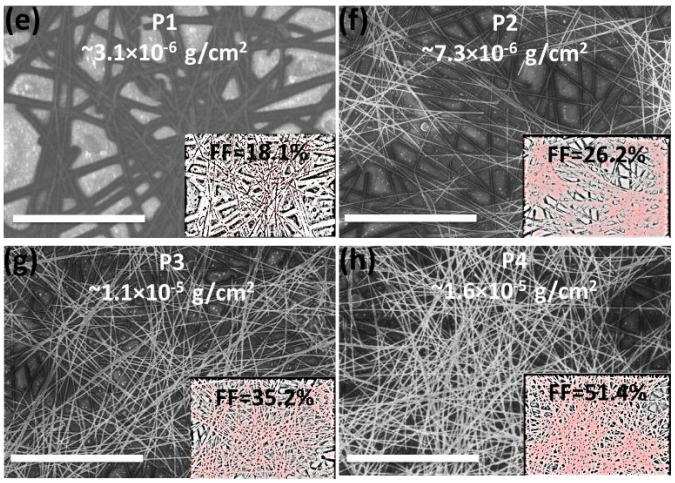

Figure 6.5. The SEM observation of the printed AgNW film on PET substrate in 4 different area densities: (a) P1~3.1×10^{-6} g cm^{-2}; (b) P2~7.3×10^{-6} g cm^{-2}; (c) P3~1.1×10^{-5} g cm^{-2}; (d) P4~1.6×10^{-5} g cm^{-2}. The scale bar is 5 μm.

As illustrated in Figure 6.6, optical transmittance over a large wavelength range is measured with a Vis-IR spectrometer using a blank PET substrate as the reference. P1 with lowest area density of ~3.1×10^{-6} g cm^{-2} (close to classical percolation limit) exhibits highest transmittance over 95% in the full range. As denser films printed, conductance

increases from ~26 KΩ/sq to ~450 Ω/sq, ~150 Ω/sq and ~100 Ω/sq for P1, P2, P3 and P4 with a 15% variation, respectively. However, transmittance decreases to around 80% near infrared range due to AgNW scattering and reflectance. It is deserved to note that visible range transmittances of these 4 different area densities all located over 85% fulfilling requirements of plenty of applications like screen displays, smart windows, photovoltaics, as well as light emitting diodes[34].

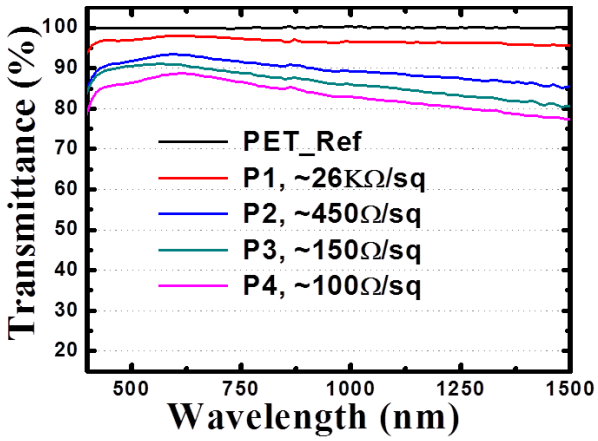

Figure 6.6. Measured sheet resistance (15% variance) and optical transmittance of printed AgNW film according to 4 different area densities

6.2.3. Laser processing set up

Right after printing, laser processing was carried out on AgNW/PET substrate, with laser parameters mentioned. Figure 6.7 shows a schematic of the experimental set-up and illustrates the NW-NW junction welding. KrF Excimer laser (λ of 248 nm and τ of 25 ns) beam shaped to a square, top-hat profile (8x8 mm) is scanning on AgNW films with enabled translations along both X and Y axis. The laser beam size is adjustable

depending on requirement. Nanowire junctions are formed at exposure time of 0.25-3.75 μs for each spot, in laser beam intensity of 20 mJ cm^{-2}. The laser intensity is chosen for nearly negligible heating effect on PET substrate, demonstrated by unchanged PET transparency and XRD signal (Figure 6.8). The laser processing effect was characterized by means of plane-view scanning electron microscopy (SEM), transmission electron microscopy (TEM), optical transmittance and electrical conductivity measurements.

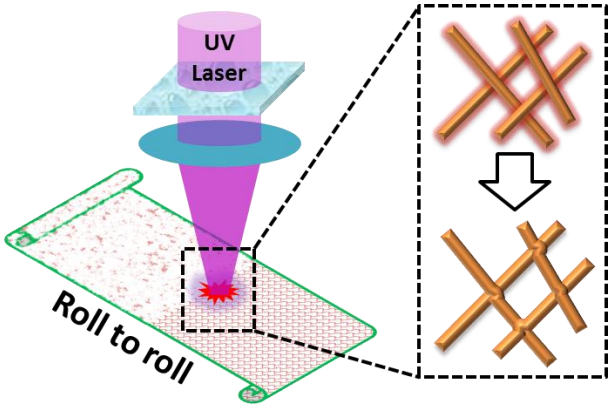

Figure 6.7. Schematic of the AgNW junction laser processing on PET substrate. The nanowires naturally contact with each other, and then enable local heating at junctions by laser exposure.

To illustrate that PET substrate has capability to sustain during laser processing, bare PET substrates subject to all laser exposure conditions were characterized by Vis-IR transmittance and X-ray diffraction (XRD) patterns in Figure 6.8a and b. As shown in Figure 6.8a, extremely slight transmittance change was detected after up to 3.75 μs exposure, comparing with untreated one. This reveals that the laser exposure will not affect the optical performance of current series of samples. Figure 6.8b plots the XRD patterns of PET substrates, before and after laser exposure, showing unchanged PET

structure due to untra-short exposure time, small heat-effective zone and fast processing speed, consistent with prior reports[109]. Both the optical performance and structure test further confirm the nearly unaffected substrate during laser processing after roll to roll printing, which is helpful for large-scale promotion.

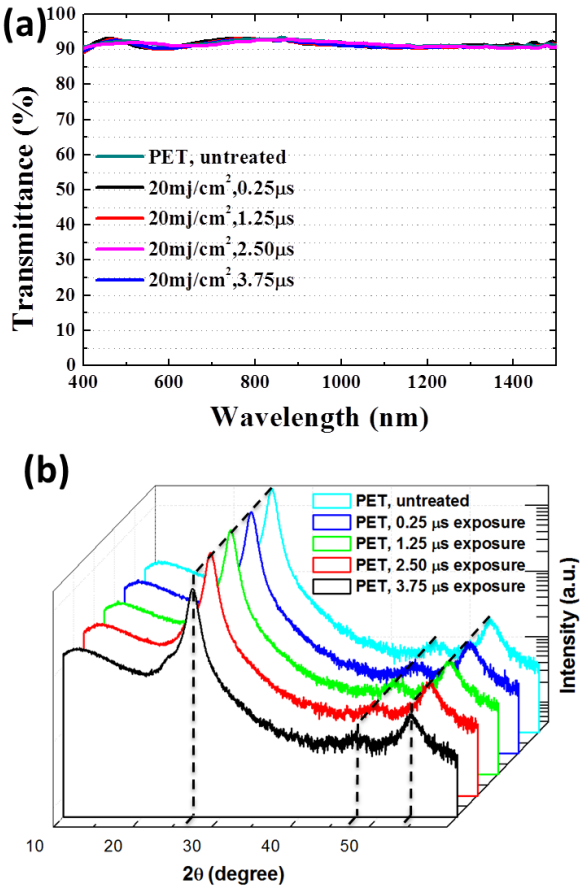

Figure 6.8. (a) Optical transmittance of bare PET versus wavelength and laser exposure time. The plots show the total diffusive transmittance as a function of wavelength for different exposure time for PET substrate. The diffusive transmittance include both specular transmitted and scattered light collected by integrating sphere. (b) XRD patterns

of bare PET as a function of laser exposure time. The plots show PET structure change according to different exposure time.

6.3. Microstructure change after laser processing

6.3.1. Surface modification

Figure 6.9a, b, c and d show plan view SEM images collected before welding and after different exposure times, respectively. Before welding, individual nanowires all over the image were clearly distinct throughout the junctions (Figure 6.9a). However, the NW-NW junctions subject to 1.25 μs and 2.50 μs laser exposure get started welding, which is indicated by contrast change at the forming solder point (Figure 6.9b and c). Apparently, the NW-NW junctions subject to 3.75 μs exposure are welded together completely, which is demonstrated by the solder point formed (Figure 6.9d). No more exposure time is applied to AgNW films suggested by the electrical measurements.

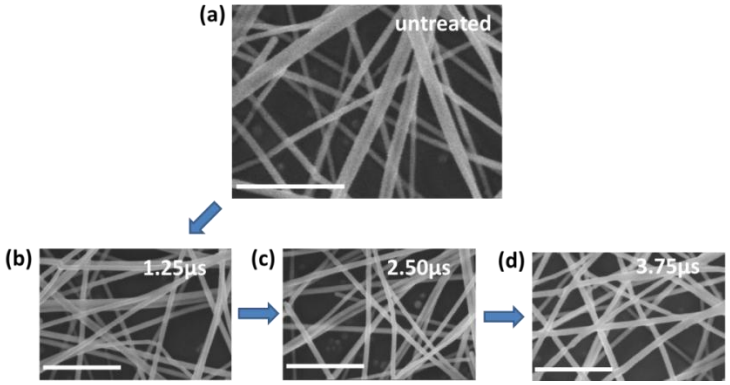

Figure 6.9. (a) plan-view SEM images of AgNW film before laser treatment. Scale bar is 500nm. Plane view SEM images of AgNW films after laser processing with different exposure time: (b) 1.25 μs; (c) 2.50 μs; (d) 3.75 μs. Scale bar is 500nm.

6.3.2. Laser welded nanojunctions

Further evidence for solder point formation and laser welded nanojunctions is also provided by high resolution TEM images in figure 6.10a and b. As marked by NW_1 and NW_2, two nanowires are slanting downward and merging together. The lattice orientation runs perpendicular cross its length, and lattice fringe measured of 0.23 nm spacing, faying with Ag (111) [110-112]. Distinct crystal orientations could be established for two merging nanowires following lattice fringe, represented by the black and white parallel line pairs[110] in figure 6.10a. Figure 6.10b shows magnified view of the rhombic area, in which two white lines mark the wire orientation of NW_2. Since the orientation of NW_2 slants bottom left corner, the silver atoms inside the rhombic should originally follow the lattice fringe of NW_2. However, going through NW-NW contact after laser processing, it clearly shows lattice orientation of NW_2 was interrupted along the edge of a rhombic area. Inside the rhombic area, atom positions seem following established lattice fringe of NW_1, and simultaneously contributed by NW_2. This reveals a silver atoms recrystallization process during laser processing, suggesting laser activated silver atoms around nanojunctions must have exhibited high mobility during ultra-fast laser treatment and allowed the recrystallization onto crystal phase at the solder point area[34, 113]. Since it is well recognized that the diffusion barrier for a single metal atom surface is quite low (less than 1 eV), which could be easily thermal activated, even at room temperature rather than laser beam exposure[113]. However, to create such isolated metal atoms demands a pretty high energy cost, especially with organic ligands coating between nanowires. The ultra-fast Laser heating is enough to remove organic ligands between nanowires and enable thermal activation as stated in chapter 3, so

isolated metal atoms can be created and thus diffused rapidly by means of surface diffusion. On the other hand, lattice fringe at solder point still could be distinguished apparently from NW_1, implying a possible non-equilibrium recrystallization[114] rather than a epitaxial recrystallization[34]. This is owing to ultra-short laser exposure serving as driven force in LPW process (25 ns per pulse). Dislocations could be found in NW_1 according to missing atoms and dislocating atom positions as shown, which ascribe to the nanowire synthesis.

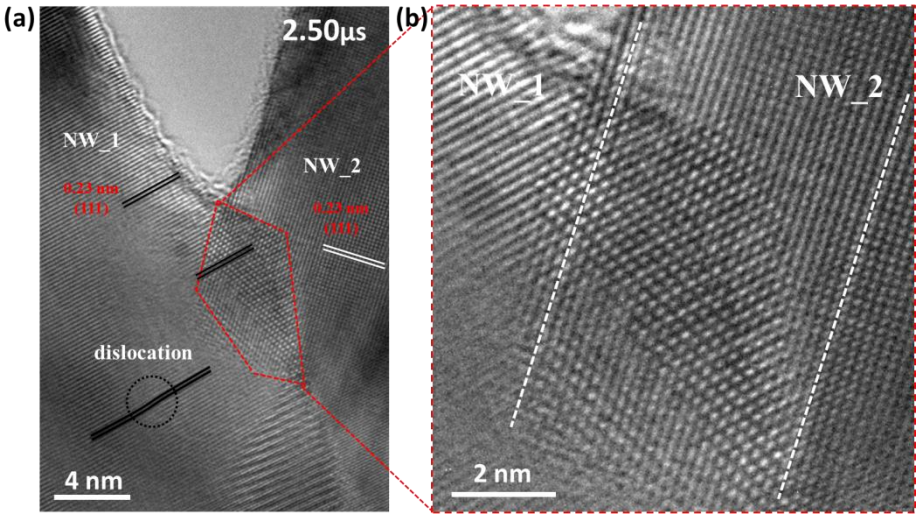

Figure 6.10. (a) HRTEM image of nanowire junction after 2.50 μs laser exposure. (b) Magnified HRTEM image of joint area formed by laser treatment.

6.3.3. The mechanism of localized welding

The selected area Fast Fourier Transform (FFT) patterns collected also verified the formation and recrystallization of solder point between contacted AgNWs after laser processing, shown in Figure 6.11. Figure 6.11a show an representative TEM image and

FFT patterns (equal to optical diffraction patterns) of single nanowire, faying with prior reports, exhibiting pentagonally twined structure sitting on the substrate with one of the five equivalent crystal facets lying flat[110]. The different contrasts inside the twinning boundaries represent the presence of microtwins and stacking faults in silver matrix. These pentagonal twined crystals aroused relatively weak double diffraction spots comparing to stronger primary patterns along one direction, leading to parallel lines of spots[34]. Figure 6.11b shows the low-magnification TEM image of nanowire junctions after laser processing. The appearance of anomalous contrast change in nanowires is due to overlapping nanowires or a high density of stacking faults in addition to twinning boundaries. The twining structure was mainly observed in nanowires, however rarely in nanojucntions due to recrystallization process of welding, more images were shown in figure 6.11c and d.

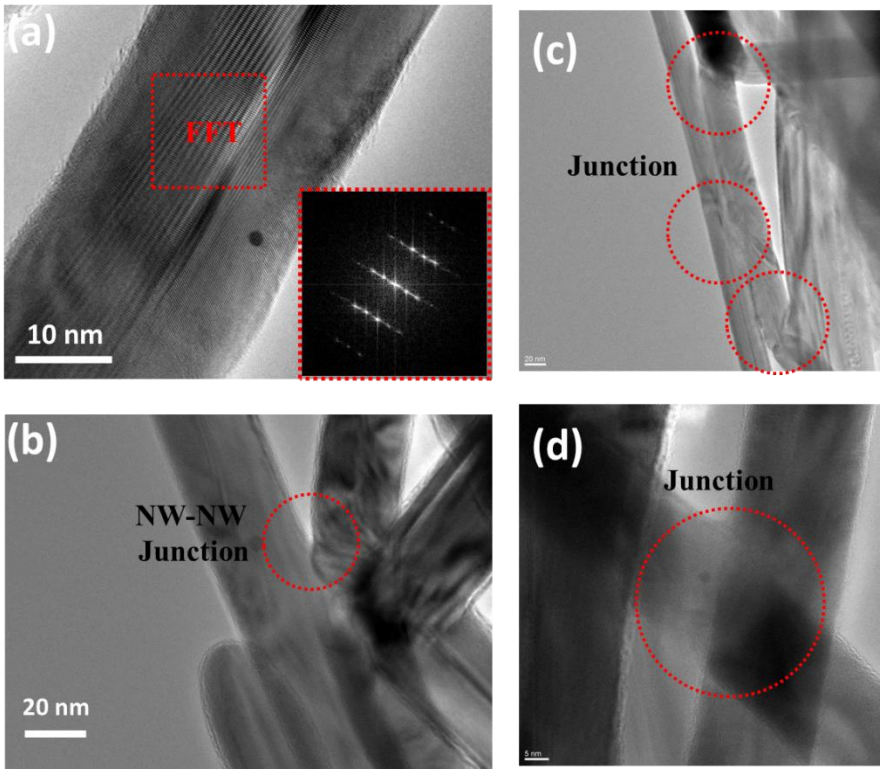

Figure 6.11. (a) HRTEM image of a single nanowire, while the insert represents the SAED patterns of the nanowire. (b), (c) and (d) Low-magnification TEM image of a nanowire junction after laser processing.

The nanowire junction is focus-in viewed and FFT patterns are analyzed in Figure 6.12a. Comparing NW_1 to NW_2, the diffraction patterns is visible along two different directions, with roughly equal intensity and rotated certain degrees (~45^{o}). Both these two diffraction patterns represent silver nanowires by tilting the silver nanowires around the growth direction of [110] (the long axis of nanowire)[110]. However, at the joint after laser processing, it is clearly seen diffraction patterns of solder point are corresponding to the single crystal with FCC structure along the [110] zone axis direction, indicating recrystallized phase and reorganized atom positions accomplished along the (111)

growing plane[110]. The geometry scheme is shown in Figure 6.12b, in which the FCC lattice of silver nanowire is tilted to be comparable with TEM image taken on right-hand side, showing the two single nanowires were grown along [110] long axis with growing plane of (111). During nanowire laser induced welding process, subcrystals along (111) plane get started to weld together via metal atom surface diffusion, in which isolated metal atoms are created by Laser heating[34, 110, 113, 115]. The crystal structures of nanowires and the welding process between them provides good comparison to prior statements[34, 110-113, 115].

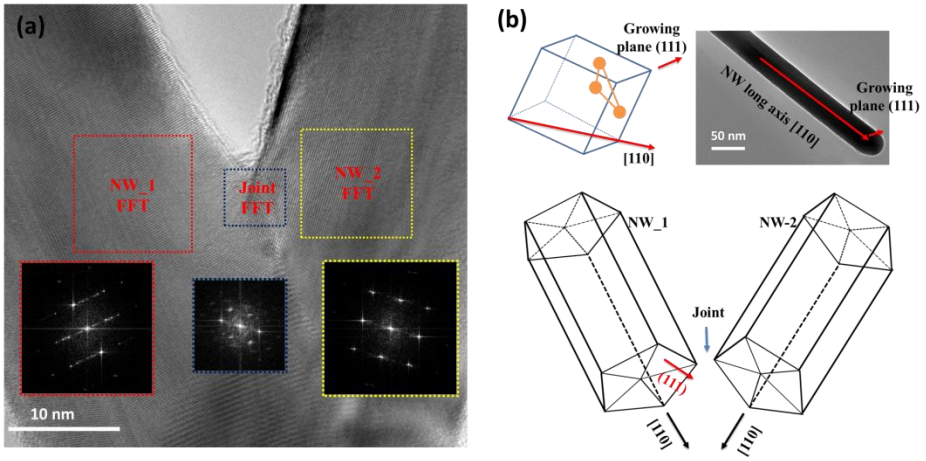

Figure 6.12. (a) and HRTEM of welded junctions, the square represents the size and location of the optical diffraction aperture used for the FFT patterns. (b) Scheme of growing silver nanowire crystal structure, where central axis of nanowire is [111] direction and growing plane is along (111) facets. Nanowires welded together merge over growing plane.

6.4. Performance characterization and discussion

6.4.1. Electrical conductance and optical transparency

To demonstrate the practicality of laser process in macro-scale applications, we printed large area AgNWs (Figure 6.4b, 8 inch by 4 inch) on PET for optoelectronic performance evaluation. Since application in flat panel displays and touch screen technologies, as well as thin-film photovoltaics, high visible transparency and low sheet resistance are required simultaneously. Thus, AgNW films subject to area density of P2 and P3 (density denoted in section 6.3) were printed and welded to achieve best optoelectronic performance. Figure 6.13a and b monitor visible-IR transmittance (average of large area test) with a bare PET substrate as reference, and 4-point-sheet resistance as a function of laser exposure time. Compared with as-printed P2 sample in Figure 6.13a, the wavelength-dependent transmittance remains almost unchanged after laser treatment, with a slight increase owing to organic ligands removal or minor variations in the nanowire density. 95-96% @ 550nm and over 90% @ visible range Transmittance were obtained for P2 samples subject to both untreated and laser welded conditions. Then, the inserted figure shows low sheet resistance simultaneously accomplished after laser processing, which decreases from 450 Ω/sq to 13 Ω/sq as laser exposure time increases from 0 to 2.50 μs. The sheet resistance drops by a factor of over 30 after 2.50 μs shining, but slightly increases subject to 3.75 μs shining (~15 Ω/sq). This large drop in resistance is attributed to UV laser nano-welding of nanowire junction, which is usually 3 orders of magnitude higher than single nanowire resistance[23, 34, 46, 116]. However, after laser welding, the dominant individual junction resistance decreases to be comparable with nanowires themselves, leading to incredible low sheet resistance as 13 Ω/sq. This also can be

demonstrated by AgNW network sheet resistance calculation according to Kirchoff's rules[117], where 10-50 Ω/sq would be contributed by solely nanowires themselves. The incredible high transmittance (95% T@550nm) and simultaneously low sheet resistance (13 Ω/sq) have not been reported before, which is comparable to bulk silver grid fabricated with perfect bulk junction between crossed grids. However, the transmittance of current sample (95% T@550nm) performs much higher than bulk silver grid, implying the superiority of ultrafast laser processed AgNW network. The slight increases subject to over-exposure of 3.75 μs, resulted from the randomly formed necking area in specific nanowires as mentioned above. Since the stretched morphology along rod axis during necking, would increases the resistance of nanowire itself. Thereby optimal laser exposure time play a crucial role. To further enhance electrical conductance, P3 sample subject to higher nanowire area density was investigated as shown in Figure 6.13b. The lowest sheet resistance of 5 Ω/sq was achieved by 2.50 μs UV laser exposure as well. However, the slight increase to 15Ω/sq after 3.75 μs UV laser shining implies the Rayleigh instability[34, 118] might be introduced by excessive heat generation from nanowire surface Plasmon or PET substrate absorption. The visible-IR transmittance of P3 sample is also nearly unaffected before and after laser, encountering slight variations similar to P2. Relative lower transmittance of 91-92% @ 550nm and over 85% @ visible range were obtained owing to higher nanowire area density. The best optoelectronic performance of 5 Ω/sq and simultaneous 91% T@550nm was also remarkable to the author's knowledge. It reveals that the laser processing has the potential to implant into commercial scale fabrication like roll-to-roll printing to fulfill the demand of enhancing AgNW TCE optoelectronic performance during printing.

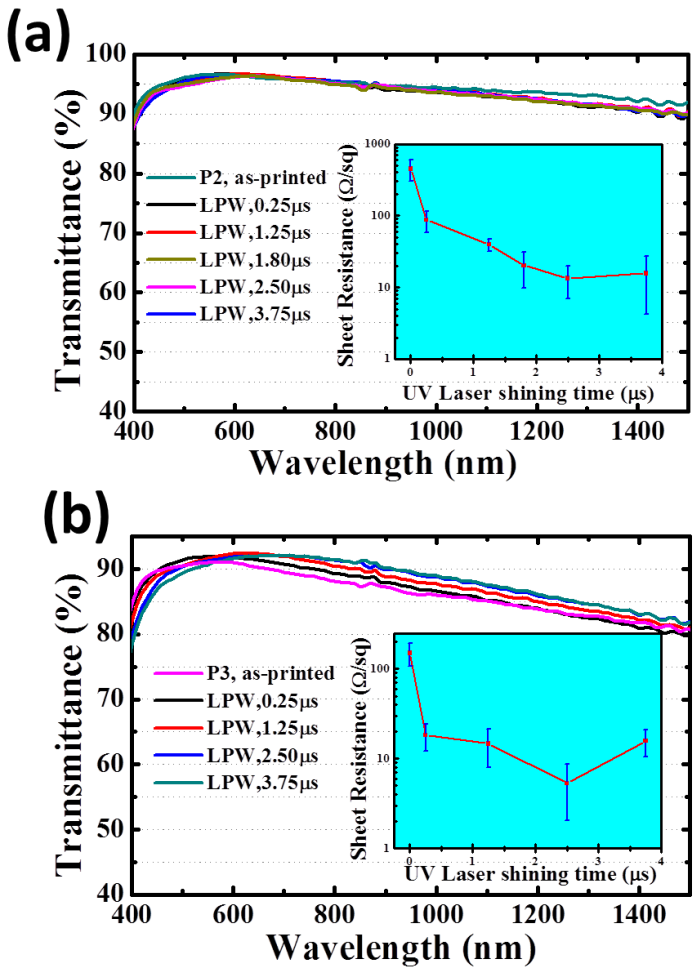

Figure 6.13. (a) Optical transmittance of P2 AgNW transparent electrode film versus wavelength and laser exposure time. The plots show the total diffusive transmittance as a function of wavelength for different exposure time for P2 sample. Insert: P2 AgNW transparent electrode sheet resistance corresponding to laser exposure time. (b) Optical transmittance of P3 AgNW transparent electrode film versus wavelength and laser exposure time. Insert: P3 AgNW transparent electrode sheet resistance corresponding to laser exposure time.

6.4.2. Percolation theory

Classical percolation theory was referred to further calculate the nanowire junction resistance and the film sheet resistance, in order to clarify the electrical conductance improvement by laser processing. As shown in equation 6.1, Stauffer *et al.[102, 103, 119]* states that, "sticks" (nanotubes & nanowires) randomly distributed throughout an insulating medium adhere to the following relation:

$$\sigma \propto (N - N_c)^t \qquad \text{Eq6.1}$$

where σ is film conductivity, N_c is the minimum wire density (per area for a 2-D film; per volume for a 3-D film) required to achieve conductivity from one side to the other, N is the actual wire density within the film and *t* is the critical exponent which accounts for dimension and percolation model. Then, Foygel *et al.[102]* advances the equation to calculate the "sticks" percolated film conductivity, considering wire density and aspect ratio as shown in equation 6.2.

$$\sigma \cong [\, R_0 \, l \, (\frac{0.6}{\alpha})^t \,]^{-1} \qquad \text{Eq6.2}$$

where R_0 is the resistance of the nanowire or of the contact between nanowires, whichever is larger. l is the typical distance between the contacts, which decreases as nanowire area density increases due to crisscross. *a* is the aspect ratio of the nanowire and t = 1.4 for our AgNWs network[102]. To calculate film sheet resistance, equation 6.3 is drawn to divide film resistivity by thickness, where *T* indicates estimated film thickness.

$$R_{sheet} \cong [\, R_0 \, l \, (\frac{0.6}{\alpha})^t \,] / T \qquad \text{Eq6.3}$$

Figure 6.14a and b plot the film conductivity and sheet resistance as a function of R_0, according to equation 6.2 and 6.3, in which l~500nm & T~70nm for P2 and l~300nm & T~100nm for P3 are assumed by pane view SEM images and ImageJ software calculation.

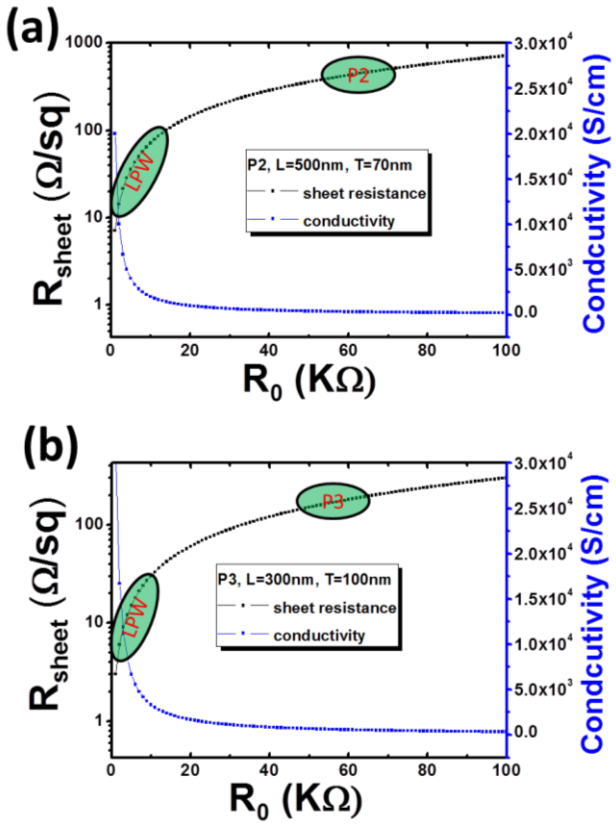

Figure 6.14. (c) P2 AgNW film sheet resistance and conductivity as a function of percolation junction resistance R_0, calculated by percolation theory with thickness T of 70nm and percolated 'stick' length L of 500nm. (d) P3 AgNW film sheet resistance and conductivity as a function of percolation junction resistance R_0, calculated by percolation theory with thickness T of 100nm and percolated 'stick' length L of 300nm.

Apparently, after laser welding, to obtain ~13 Ω/sq for P2, R_0 should be <2KΩ, revealing that the contact resistance between nanowire junctions becomes comparable or negligible

to that of nanowires themselves (R_{NW}). Directly calculated R_{NW} could be as low as ~0.25KΩ for a single AgNW with 15μm in length and 35nm in diameter, whereas actually value usually approaches one or several KΩ[34] probably because of oxidation degrading and organic ligands coating. Therefore after laser treatment, taking off R_{NW} contribution to R_0, the contact resistance cross nanowires could be estimated as 0 Ω. However, before welding, R_{sheet} subject to P2 is ~450Ω/sq, and this corresponds to R_0 of >60 KΩ revealing that junction resistance is dominant. As well as P3, R_0 is decreased from >55 KΩ to <2 KΩ after laser welding as well, according to sheet resistance change. This change implies the dominant resistance of NW-NW junctions has been decreased by laser induced nano-welding, and finally becoming comparable or negligible to single nanowire resistance, as illustrated in figure 6.15.

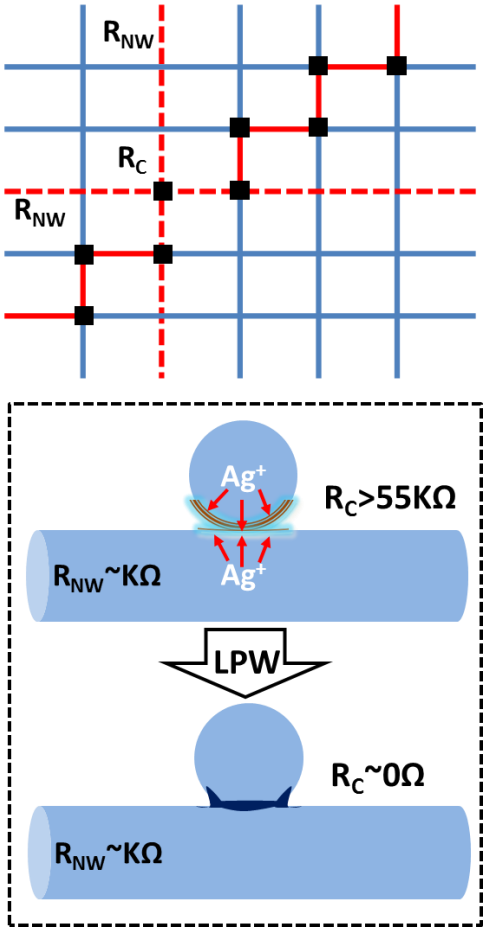

Figure 6.15. Scheme of AgNW network conductance dominated by contact resistance through percolating nanowires and the scheme of LPW effect on nanowire contact resistance.

6.4.3. HAZE measurements

Similarly to AZO, the transmittance in current investigation was measured by Lambda 950 with an integrating sphere to integrate all forward light including both specular transmitted and scattered transmitted. The specular transmittance indicates the light comes out of the sample parallel to the incident light. The difference between the

diffusive and specular transmittance is generally utilized to evaluate the light scattering which might trigger problematic for flat panel displays and touch screens[23, 53]. To measure the light scattering, the baseline for the spectroscopy is set by scanning a blank PET substrate and then AgNW film is installed on a solid sample holder between light source and the detector. The diffusive and specular transmittance data are obtained at 550 nm wavelength, the difference between them are shown in Figure 6.16 comparing with other transparent electrode alternatives[23, 53]. It can be seen that the scattering of AgNW film on PET substrate after LPW is ~4.2% and ~5.6% subject to P2 and P3 density, respectively. Considering approximate 2% light scattering contributed by PET itself (1% for glass substrate), only ~2.2% and 3.6% result from P2 and P3 metal nanowire scattering. Taking off the scattered transmitted light, the pure specular transmittance of P2 and P3 samples achieve 92.8% and 87.4%, which are also outstanding performance and fulfill industrial requirements. Relative higher nanowire density will result in larger light scattering, which is consistent with metal nanowire optical property[23]. However, it is lower than prior reports of Ag nanowire (~10%)[23] and AgNW-Graphene hybrid film[53] (h3, ~6.6%), attributing to slimmer nanowires and more uniform printing. As we know, it was remaining an issue to fabricate uniform film of AgNW with high aspect ratio like 35nm in diameter and 15μm in length before this study. Comparing with single walled carbon nanotubes network (~3%), P2 sample is more competitive. But it is additionally desired to note that CNT lose transmittance due to absorption while AgNW film lose transmittance due to scattering, not absorption[66]. Unfortunately, current series of samples still suffer from competing with traditional transparent conductive oxide (TCO) like ITO (~1%)[23, 53]. However, due to flexible

and stretchable electronic devices demand, AgNWs network would be favorable over brittle TCO, especially for light scattering preferred device like thin film photovoltaics.

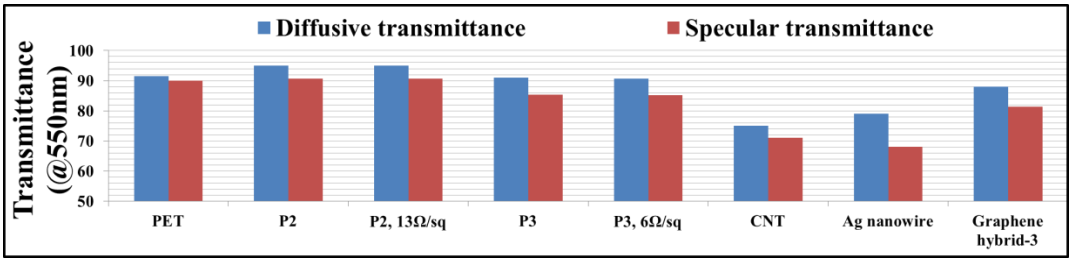

Figure 6.16. Diffusive and specular transmittance of PET substrate, CNT on glass, Ag nanowire on glass, Graphene hybrid on glass, and P2, P3 AgNW on PET substrate. The differences in the diffusive and specular transmittance indicate the scattering of the light by the material.

6.4.4. Mechanical and chemical stability

To explore the mechanical stability of welded AgNW film which might be utilized in future flexible optoelectronic devices, mechanical related characterizations were carried out like bending sheet resistance (figure 6.17a). As shown in figure 6.17a, the resistance measurements of AgNW/PET with curvature from 0 to 0.06 mm^{-1} were carried out to test the bending flexibility. It was detected that P2 and P3 samples (before laser processing) possess pretty stable conductance during bending, comparing to standard brittle ITO film. However, there are still fluctuations observed due to not welded cross nanowire junction. After laser processing, P2 and P3 achieve ultra-stable conductance during bending, though negligible fluctuations felling into the scope of conductance deviation, illustrating outstanding flexibility in current series of samples[53]. Finally, chemical stability was

tested in ambient atmosphere as shown in supporting materials (6.17b and c). The sheet resistance of P2 and P3 samples under different laser welding conditions was tested after 3 months, comparing with right after roll to roll printing combined laser processing, the evaluation reveals that electrical conductance nearly maintains unchanged after long time period. The stable electrical property is important for practical macro-scale application even though protective package will be added in commercial fabrication.

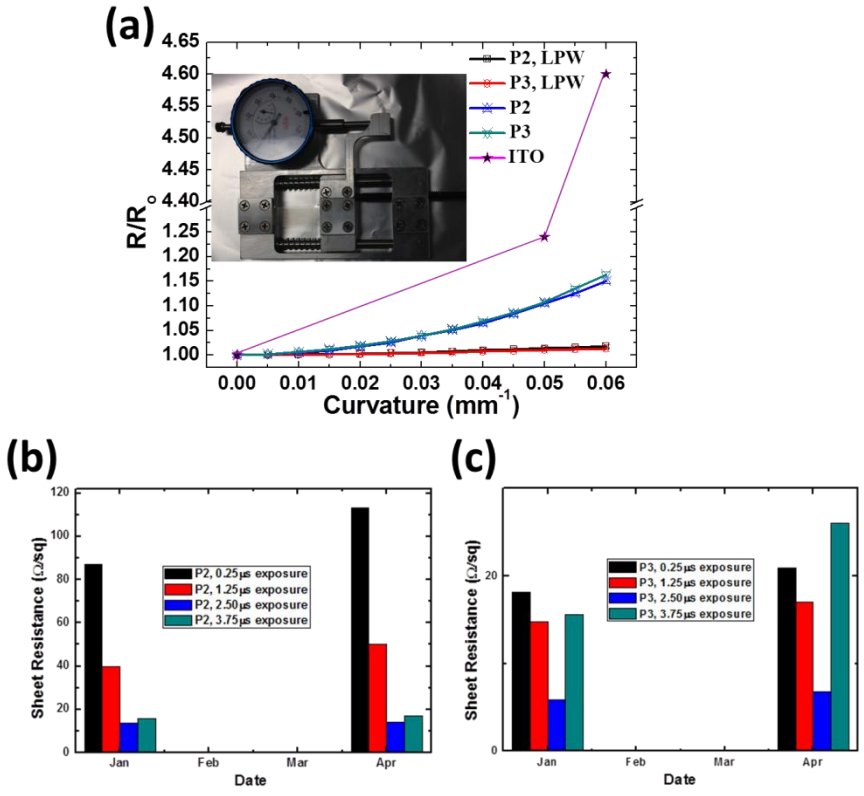

Figure 6.17. (a) The ratio of bending resistance to original resistance as a function of bending curvature before and after laser processing for P2 and P3 samples, comparing to standard ITO film. The insert shows the designed bending gadget. (b) chemical stability test of laser processed P2 AgNW network on PET. (c) chemical stability test of laser processed P3 AgNW network on PET.

6.4.5. Overexposure effect

The supplementary experiments were added to explore the effect of laser power on the performance of AgNW thin film. 5 different laser power densities were utlized as 15, 20, 35, 50, 65 mJ cm^{-2}, subject to the same exposure time of 2.5 μs. The sheet resistance curve revealed higher laser intensity than optimal one (20 mJ cm^{-2}) like 35 mJ cm^{-2} would decrease the film performance a little bit, due to overexposure might hurt nanojunctions or nanowire itself. The inserted SEM image of figure 6.18 confirmed about the overexposure issue of the nanowire network, in which selected area of nanowires are broken and fragmented to short sections. Those nanowire morphology change affected macro scale film electrical performance. Even higher laser intensity like 50-65 mJ cm^{-2} would destroy the whole film as shown in the sheet resistance curve, in which film conductivity has become insulate (beyond the contact of limit of our 4 point measurement). The inserted SEM of destroyed nanowire network also confirmed that nanowires are degraded to not only short sections but also nanobeads, which fays well with Raleigh instability[120].

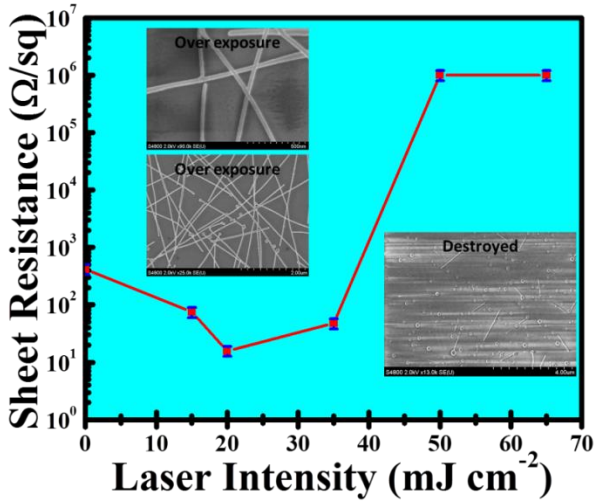

Figure 6.18. AgNW film sheet resistances as a function of laser power. The inserts shows the demonstration of selected area of damaged nanowires by over exposure and some area of destroyed nanowires by ultra-intense laser ablation.

6.5. Summary of this chapter

In summary, the high speed LPW provides direct, efficient and selective generation of NW-NW crystalline junction in roll-to-roll printed AgNWs percolated networks. Such as the optoelectronic performance evaluation, the transmittance @ 550nm of current series of direct laser welded AgNW films was plotted as a function of film sheet resistance in Figure 6.19 and compared to experimental data for ITO thin films[10] and other developed transparent electrode alternatives such as metal gratings[11], CNT random meshes[94-96], referring AgNWs[23, 51] and graphene/hybrid graphene[53, 97]. All of these transparent electrodes need to compromise the transmittance to achieve lower sheet resistance (<100 Ω/sq), with which AgNW films perform similarly. However, the uniformly printed films with high aspect ratio Ag nanowires could accomplish ~13 Ω/sq and 95% transmittance (P2), which show more competitiveness than ITO thin film in the mainstream market and the cutting age alternatives. AgNW films subject to higher density (P3) could achieve ~5 Ω/sq and 91% transmittance due to higher reflectance and scattering[23]. This mass-produced AgNW films show superior performance, which simultaneously possessing low cost solution based fabrication, uniform Roll-to-Roll printing and efficient laser processing could immediate commercial scale manufacturing.

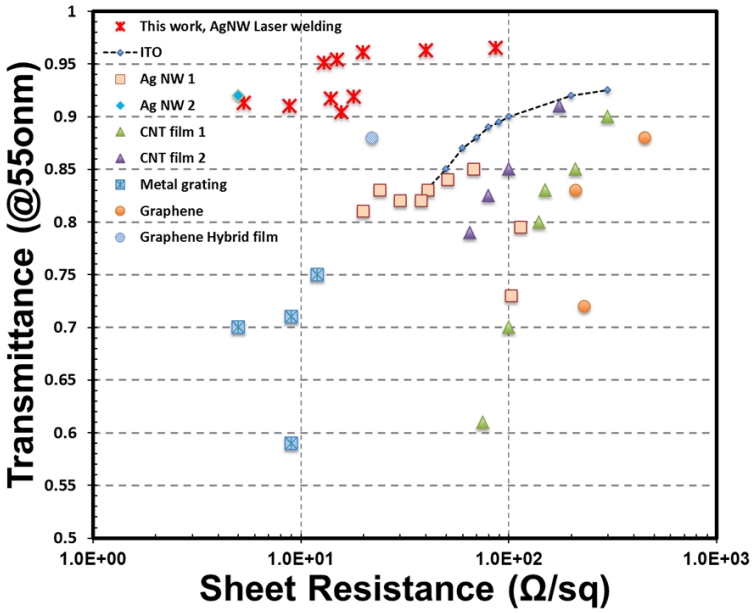

Figure 6.19. Optical transmittance @550nm wavelength of laser welded P2 and P3 AgNW TCE as a function of sheet resistance. The performance of ITO, CNT, Graphene, and metal gratings are shown for comparison.

CHAPTER 7. CONCLUSION

To date, the industry standard TCE material is ITO (tin-doped indium-oxide) because of best optoelectronic property[21]. ITO achieves low resistivity of ~1-2×10−4 Ωcm and a transmittance over 80%. However, ITO has the drawback of being expensive, that is due to the film's primary metal Indium is rare (6000 metric tons worldwide, 2006) and price fluctuates due to market demand (over $800/kg, 2006)[22]. Therefore, earth abundant doped zinc oxide (ZnO:X) has been proposed as alternative materials[21], as well as other like metal nanowires network[23]. Al doped ZnO (AZO) and nanometals are currently under intense investigation and development to replace indium tin oxide (ITO) as TCE film[27], though latter one is the standard compound for most applications performing best optoelectronic property[21]. Since it is crucial that AZO and metals ensure a sustainable supply of the earth abundant and cost-effect alternatives and which is also reflected in predicted markets of $925 million in 2016 for alternative TCEs [28] in figure 7.1.

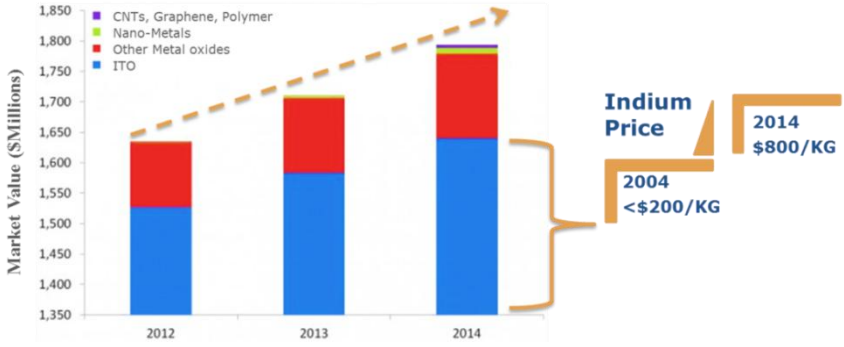

Figure 7.1. IDTechEx©, Transparent Conductive Films (TCF) 2014-2024: Forecasts, Markets, Technologies NanoMarkets™, Emerging Markets for Non-ITO Transparent Conductive Oxides, 2011

Current dissertation milestones the accomplished AZO film and AgNW film performance via laser processing, comparing with experimental data for ITO thin films and other recently developed transparent electrode alternatives such as CNT random meshes, silver nanowire networks[23], metal gratings[11] and graphene[53, 97]. The laser processed films compare favorably to vapor deposited ITO and other transparent electrodes at a lower manufacturing cost due to the nature of printing technology. Those prior advancements have achieved high electrical conductivity on different substrates with mainly high vacuum and high temperature methods. In current dissertation, we developed the aqueous solution / ethanol solution based nanomaterial ink, enabled printing technology, and sparked off the following laser processing to boost up film performance after printing. This method provides a low cost TCE film fabrication without compromise on performance.

This first material system is composed of AZO nanocrystal thin films. With efforts in developing laser processing on the AZO coatings, an in-depth understanding has been achieved and following remarks were drawn:

1. In the simulation of laser processing 0D and 1D nanomaterials, the laser induced plasmonic effect and the brought localized nanowelding was studied.

2. In the experiment of the AZO nanocrystal film coating and laser processing, SEM, XRD and other techniques confirmed the microstructure improvement of the thin film after laser processing.

3. The electrical and optical performance of laser processed aqueous solution based AZO coating was investigated. High conductivity and simultaneous outstanding optical transparency were achieved. The mobility increase was turn out to be the dominant factor which leads to high conductivity without drawback optical transparency.

4. Various mechanism of mobility increase was studied and theoretical analyzed. The grain boundary density decrease and electro trap density decrease at grain boundaries were prove to be the dominant factors, in the polycrystalline AZO film.

The Second material system is metal nanowire network (AgNW).

1. The similar simulation and experiment of AgNW printing and laser processing were conducted. SEM, TEM and other techniques confirmed the nanowelding between metal nanowire, which laser was shining on the thin film and plasmonic effect heating was induced.

2. The electrical and optical performance of laser processed AgNW printing was investigated. High conductivity and simultaneous outstanding optical transparency were achieved. The conductance between adjacent crossed nanowires increase was turn out to be the dominant factor which leads to high conductivity without drawback optical transparency. The percolation theory and MD simulation verified the mechanism.

LIST OF REFERENCES

LIST OF REFERENCES

[1] K. Ellmer, "Past achievements and future challenges in the development of optically transparent electrodes," *Nature Photonics,* vol. 6, pp. 809-817, 2012.

[2] T. Minami, "Transparent conducting oxide semiconductors for transparent electrodes," *Semiconductor Science and Technology,* vol. 20, p. S35, 2005.

[3] D. L. White and M. Feldman, "Liquid-crystal light valves," *Electronics Letters,* vol. 6, pp. 837-839, 1970.

[4] U. Betz, M. Kharrazi Olsson, J. Marthy, M. F. Escolá, and F. Atamny, "Thin films engineering of indium tin oxide: Large area flat panel displays application," *Surface and Coatings Technology,* vol. 200, pp. 5751-5759, 5/22/ 2006.

[5] M. Katayama, "TFT-LCD technology," *Thin Solid Films,* vol. 341, pp. 140-147, 3/12/ 1999.

[6] B. Rech and H. Wagner, "Potential of amorphous silicon for solar cells," *Applied Physics A,* vol. 69, pp. 155-167, 1999/08/01 1999.

[7] E. Fortunato, D. Ginley, H. Hosono, and D. C. Paine, "Transparent Conducting Oxides for Photovoltaics," *MRS Bulletin,* vol. 32, pp. 242-247, 2007.

[8] A. Kumar and C. Zhou, "The Race To Replace Tin-Doped Indium Oxide: Which Material Will Win?," *ACS Nano,* vol. 4, pp. 11-14, 2010/01/26 2010.

[9] M. Eritt, C. May, K. Leo, M. Toerker, and C. Radehaus, "OLED manufacturing for large area lighting applications," *Thin Solid Films,* vol. 518, pp. 3042-3045, 3/31/ 2010.

[10] J.-Y. Lee, S. T. Connor, Y. Cui, and P. Peumans, "Solution-Processed Metal Nanowire Mesh Transparent Electrodes," *Nano Letters,* vol. 8, pp. 689-692, 2008/02/01 2008.

[11] M. G. Kang and L. J. Guo, "Nanoimprinted Semitransparent Metal Electrodes and Their Application in Organic Light-Emitting Diodes," *Advanced Materials,* vol. 19, pp. 1391-1396, 2007.

[12] S. De, P. J. King, P. E. Lyons, U. Khan, and J. N. Coleman, "Size Effects and the Problem with Percolation in Nanostructured Transparent Conductors," *ACS Nano,* vol. 4, pp. 7064-7072, 2010/12/28 2010.

[13] Z. Zhang, C. Bao, S. Ma, and S. Hou, "Effect of crystallinity of ZnO buffer layer on the properties of epitaxial (ZnO:Al)/(ZnO:Ga) bi-layer films deposited on c-sapphire substrate," *Applied Surface Science,* vol. 257, pp. 7893-7899, 2011.

[14] D. C. Look, C. Coşkun, B. Claflin, and G. C. Farlow, "Electrical and optical properties of defects and impurities in ZnO," *Physica B: Condensed Matter,* vol. 340–342, pp. 32-38, 12/31/ 2003.

[15] L. Ding, S. Nicolay, J. Steinhauser, U. Kroll, and C. Ballif, "Relaxing the Conductivity/Transparency Trade-Off in MOCVD ZnO Thin Films by Hydrogen Plasma," *Advanced Functional Materials,* vol. 23, pp. 5177-5182, 2013.

[16] W.-J. Jeong and G.-C. Park, "Electrical and optical properties of ZnO thin film as a function of deposition parameters," *Solar Energy Materials and Solar Cells,* vol. 65, pp. 37-45, 1// 2001.

[17] O. Bamiduro, H. Mustafa, R. Mundle, R. B. Konda, and A. K. Pradhan, "Metal-like conductivity in transparent Al:ZnO films," *Applied Physics Letters,* vol. 90, p. 252108, 2007.

[18] N. P. Dasgupta, S. Neubert, W. Lee, O. Trejo, J.-R. Lee, and F. B. Prinz, "Atomic Layer Deposition of Al-doped ZnO Films: Effect of Grain Orientation on Conductivity," *Chemistry of Materials,* vol. 22, pp. 4769-4775, 2010.

[19] K. Ellmer, "Electrical Properties," in *Transparent Conductive Zinc Oxide*. vol. 104, K. Ellmer, A. Klein, and B. Rech, Eds., ed: Springer Berlin Heidelberg, 2008, pp. 35-78.

[20] A. E. Delahoy and S. Guo, "Transparent Conducting Oxides for Photovoltaics," in *Handbook of Photovoltaic Science and Engineering*, ed: John Wiley & Sons, Ltd, 2011, pp. 716-796.

[21] H. Hagendorfer, K. Lienau, S. Nishiwaki, C. M. Fella, L. Kranz, A. R. Uhl, *et al.*, "Highly Transparent and Conductive ZnO: Al Thin Films from a Low Temperature Aqueous Solution Approach," *Adv Mater,* vol. 26, pp. 632-6, Jan 2014.

[22] "Indium," *USGS report*.

[23] L. Hu, H. S. Kim, J.-Y. Lee, P. Peumans, and Y. Cui, "Scalable Coating and Properties of Transparent, Flexible, Silver Nanowire Electrodes," *ACS Nano,* vol. 4, pp. 2955-2963, 2010/05/25 2010.

[24] D. Altamiranojuarez, "Low-resistivity ZnO:F:Al transparent thin films," *Solar Energy Materials and Solar Cells,* vol. 82, pp. 35-43, 2004.

[25] A. E. Jiménez González and J. A. Soto Urueta, "Optical transmittance and photoconductivity studies on ZnO : Al thin films prepared by the sol–gel technique," *Solar Energy Materials and Solar Cells*, vol. 52, pp. 345-353, 4/30/ 1998.

[26] S. J. Pearton, D. P. Norton, K. Ip, Y. W. Heo, and T. Steiner, "Recent progress in processing and properties of ZnO," *Progress in Materials Science,* vol. 50, pp. 293-340, 3// 2005.

[27] J.-P. Lin and J.-M. Wu, "The effect of annealing processes on electronic properties of sol-gel derived Al-doped ZnO films," *Applied Physics Letters,* vol. 92, p. 134103, 2008.

[28] "Emerging markets for non-ITO transparent conductive oxides Market study TCOs," NanoMarkets Report2011.

[29] M. Y. Zhang, Q. Nian, and G. J. Cheng, "Room temperature deposition of alumina-doped zinc oxide on flexible substrates by direct pulsed laser recrystallization," *Applied Physics Letters,* vol. 100, pp. 151902-151902-4, 2012.

[30] S. Takata, T. Minami, and H. Nanto, "The stability of aluminium-doped ZnO transparent electrodes fabricated by sputtering," *Thin Solid Films,* vol. 135, pp. 183-187, 1/15/ 1986.

[31] T. Stubhan, M. Salinas, A. Ebel, F. C. Krebs, A. Hirsch, M. Halik, *et al.*, "Increasing the Fill Factor of Inverted P3HT:PCBM Solar Cells Through Surface Modification of Al-Doped ZnO via Phosphonic Acid-Anchored C60 SAMs," *Advanced Energy Materials,* vol. 2, pp. 532-535, 2012.

[32] H. Cheun, C. Fuentes-Hernandez, J. Shim, Y. Fang, Y. Cai, H. Li, *et al.*, "Oriented Growth of Al2O3:ZnO Nanolaminates for Use as Electron-Selective Electrodes in Inverted Polymer Solar Cells," *Advanced Functional Materials,* vol. 22, pp. 1531-1538, 2012.

[33] H. Kim, C. M. Gilmore, J. S. Horwitz, A. Piqué, H. Murata, G. P. Kushto, *et al.*, "Transparent conducting aluminum-doped zinc oxide thin films for organic light-emitting devices," *Applied Physics Letters,* vol. 76, p. 259, 2000.

[34] E. C. Garnett, W. Cai, J. J. Cha, F. Mahmood, S. T. Connor, M. Greyson Christoforo, *et al.*, "Self-limited plasmonic welding of silver nanowire junctions," *Nat Mater,* vol. 11, pp. 241-9, Mar 2012.

[35] B. Han, K. Pei, Y. Huang, X. Zhang, Q. Rong, Q. Lin, *et al.*, "Uniform self-forming metallic network as a high-performance transparent conductive electrode," *Adv Mater,* vol. 26, pp. 873-7, Feb 2014.

[36] G. Baffou, R. Quidant, and C. Girard, "Heat generation in plasmonic nanostructures: Influence of morphology," *Applied Physics Letters,* vol. 94, p. 153109, 2009.

[37] S. Plimpton, "Fast Parallel Algorithms for Short-Range Molecular Dynamics," *Journal of Computational Physics,* vol. 117, pp. 1-19, 3/1/ 1995.

[38] S. Alexander, "Visualization and analysis of atomistic simulation data with OVITO–the Open Visualization Tool," *Modelling and Simulation in Materials Science and Engineering,* vol. 18, p. 015012, 2010.

[39] D. J. Binks and R. W. Grimes, "Incorporation of Monovalent Ions in ZnO and Their Influence on Varistor Degradation," *Journal of the American Ceramic Society,* vol. 76, pp. 2370-2372, 1993.

[40] D. Jason Binks and R. W. Grimes, "The non-stoichiometry of zinc and chromium excess zinc chromite," *Solid State Communications,* vol. 89, pp. 921-924, 3// 1994.

[41] T. Darden, D. York, and L. Pedersen, "Particle mesh Ewald: An N·log(N) method for Ewald sums in large systems," *The Journal of Chemical Physics,* vol. 98, pp. 10089-10092, 1993.

[42] M. Y. Zhang, Q. Nian, Y. Shin, and G. J. Cheng, "Direct pulsed laser crystallization of nanocrystals for absorbent layers in photovoltaics: Multiphysics simulation and experiment," *Journal of Applied Physics,* vol. 113, p. 193506, 2013.

[43] M. Y. Zhang and G. J. Cheng, "Highly conductive and transparent alumina-doped ZnO films processed by direct pulsed laser recrystallization at room temperature," *Applied Physics Letters,* vol. 99, p. 051904, 2011.

[44] H. Qian, Y. Ma, Q. Yang, B. Chen, Y. Liu, X. Guo, *et al.*, "Electrical Tuning of Surface Plasmon Polariton Propagation in Graphene–Nanowire Hybrid Structure," *ACS Nano,* 2014.

[45] M. Song, G. Chen, Y. Liu, E. Wu, B. wu, and H. Zeng, "Polarization properties of surface plasmon enhanced photoluminescence from a single Ag nanowire," *Optics Express,* vol. 20, pp. 22290-22297, 2012/09/24 2012.

[46] J. A. Spechler and C. B. Arnold, "Direct-write pulsed laser processed silver nanowire networks for transparent conducting electrodes," *Applied Physics A,* vol. 108, pp. 25-28, 2012.

[47] M. W. Finnis and J. E. Sinclair, "A simple empirical N-body potential for transition metals," *Philosophical Magazine A,* vol. 50, pp. 45-55, 1984/07/01 1984.

[48] P. L. Williams, Y. Mishin, and J. C. Hamilton, "An embedded-atom potential for the Cu–Ag system," *Modelling and Simulation in Materials Science and Engineering,* vol. 14, pp. 817-833, 2006.

[49] A. Stukowski, "Visualization and analysis of atomistic simulation data with OVITO–the Open Visualization Tool," *Modelling and Simulation in Materials Science and Engineering,* vol. 18, p. 015012, 2010.

[50] H. Tsuzuki, P. S. Branicio, and J. P. Rino, "Structural characterization of deformed crystals by analysis of common atomic neighborhood," *Computer Physics Communications,* vol. 177, pp. 518-523, 9/15/ 2007.

[51] S. J. Lee, Y.-H. Kim, J. K. Kim, H. Baik, J. H. Park, J. Lee, *et al.*, "A roll-to-roll welding process for planarized silver nanowire electrodes," *Nanoscale,* vol. 6, pp. 11828-11834, 2014.

[52] C. Kelchner, S. Plimpton, and J. Hamilton, "<title>Dislocation nucleation and defect structure during surface indentation</title>," *Physical Review B,* vol. 58, pp. 11085-11088, 11/01/ 1998.

[53] R. Chen, S. R. Das, C. Jeong, M. R. Khan, D. B. Janes, and M. A. Alam, "Co-Percolating Graphene-Wrapped Silver Nanowire Network for High Performance, Highly Stable, Transparent Conducting Electrodes," *Advanced Functional Materials,* vol. 23, pp. 5150-5158, 2013.

[54] F. M. Smits, "Measurement of sheet resistivities with the four-point probe," *Bell System Technical Journal, The,* vol. 37, pp. 711-718, 1958.

[55] D. K. Schroder, *Semiconductor material and device characterization*: John Wiley & Sons, 2006.

[56] P. Nunes, E. Fortunato, P. Tonello, F. Braz Fernandes, P. Vilarinho, and R. Martins, "Effect of different dopant elements on the properties of ZnO thin films," *Vacuum,* vol. 64, pp. 281-285, 1// 2002.

[57] T. Minami, S. Suzuki, and T. Miyata, "Transparent conducting impurity-co-doped ZnO:Al thin films prepared by magnetron sputtering," *Thin Solid Films,* vol. 398–399, pp. 53-58, 11// 2001.

[58] M. E. Fragalà, G. Malandrino, M. M. Giangregorio, M. Losurdo, G. Bruno, S. Lettieri, *et al.*, "Structural, Optical, and Electrical Characterization of ZnO and Al-doped ZnO Thin Films Deposited by MOCVD," *Chemical Vapor Deposition,* vol. 15, pp. 327-333, 2009.

[59] J.-H. Oh, K.-K. Kim, and T.-Y. Seong, "Effects of deposition temperatures and annealing conditions on the microstructural, electrical and optical properties of polycrystalline Al-doped ZnO thin films," *Applied Surface Science,* vol. 257, pp. 2731-2736, 1/15/ 2011.

[60] J. I. Owen, W. Zhang, D. Köhl, and J. Hüpkes, "Study on the in-line sputtering growth and structural properties of polycrystalline ZnO:Al on ZnO and glass," *Journal of Crystal Growth,* vol. 344, pp. 12-18, 2012.

[61] C. Guillén and J. Herrero, "Optical, electrical and structural characteristics of Al:ZnO thin films with various thicknesses deposited by DC sputtering at room temperature and annealed in air or vacuum," *Vacuum,* vol. 84, pp. 924-929, 2010.

[62] K. Matsubara, P. Fons, K. Iwata, A. Yamada, and S. Niki, "Room-temperature deposition of Al-doped ZnO films by oxygen radical-assisted pulsed laser deposition," *Thin Solid Films,* vol. 422, pp. 176-179, 12/20/ 2002.

[63] A. V. Singh, R. M. Mehra, N. Buthrath, A. Wakahara, and A. Yoshida, "Highly conductive and transparent aluminum-doped zinc oxide thin films prepared by pulsed laser deposition in oxygen ambient," *Journal of Applied Physics,* vol. 90, p. 5661, 2001.

[64] R. J. Lad, P. D. Funkenbusch, and C. R. Aita, "Postdeposition annealing behavior of rf sputtered ZnO films," *Journal of Vacuum Science and Technology,* vol. 17, pp. 808-811, 1980.

[65] M. A. Al-Maghrabi, M. F. Al-Kuhaili, S. M. A. Durrani, and I. A. Bakhtiari, "Influence of vacuum annealing on the physical properties of ZnO/Al/ZnO multilayer coatings," *Journal of Vacuum Science & Technology A: Vacuum, Surfaces, and Films,* vol. 27, p. 276, 2009.

[66] L. Ding, M. Boccard, G. Bugnon, M. Benkhaira, S. Nicolay, M. Despeisse, *et al.*, "Highly transparent ZnO bilayers by LP-MOCVD as front electrodes for thin-film micromorph silicon solar cells," *Solar Energy Materials and Solar Cells,* vol. 98, pp. 331-336, 3// 2012.

[67] Y. Geng, Z. Y. Xie, S. S. Xu, Q. Q. Sun, S. J. Ding, H. L. Lu, *et al.*, ECS Journal of Solid State Science and Technology, vol. 1, pp. N45-N48, 2012.

[68] T. Sahoo, J.-W. Ju, V. Kannan, J. S. Kim, Y.-T. Yu, M.-S. Han, *et al.*, "Effect of precursor on epitaxially grown of ZnO thin film on p-GaN/sapphire (0 0 0 1) substrate by hydrothermal technique," *Materials Research Bulletin*, vol. 43, pp. 502-509, 3/4/ 2008.

[69] Y. Hwang, H. Kim, and Y. Um, "Structural, electrical, and ellipsometric properties of nitrogen-annealed ZnO:Al films," *Current Applied Physics*, vol. 12, pp. S76-S79, 2012.

[70] J. Zhang and W. Que, "Preparation and characterization of sol–gel Al-doped ZnO thin films and ZnO nanowire arrays grown on Al-doped ZnO seed layer by hydrothermal method," *Solar Energy Materials and Solar Cells*, vol. 94, pp. 2181-2186, 2010.

[71] A. Aprilia, P. Wulandari, V. Suendo, Herman, R. Hidayat, A. Fujii, *et al.*, "Influences of dopant concentration in sol–gel derived AZO layer on the performance of P3HT:PCBM based inverted solar cell," *Solar Energy Materials and Solar Cells*, vol. 111, pp. 181-188, 2013.

[72] Z. Zhan, J. Zhang, Q. Zheng, D. Pan, J. Huang, F. Huang, *et al.*, "Strategy for Preparing Al-Doped ZnO Thin Film with High Mobility and High Stability," *Crystal Growth & Design*, vol. 11, pp. 21-25, 2011.

[73] J. G. Lu, Z. Z. Ye, Y. J. Zeng, L. P. Zhu, L. Wang, J. Yuan, *et al.*, "Structural, optical, and electrical properties of (Zn,Al)O films over a wide range of compositions," *Journal of Applied Physics*, vol. 100, p. 073714, 2006.

[74] T. Minami, "New n-Type Transparent Conducting Oxides," *MRS Bulletin*, vol. 25, pp. 38-44, 2000.

[75] J. Y. W. Seto, "The electrical properties of polycrystalline silicon films," *Journal of Applied Physics*, vol. 46, pp. 5247-5254, 1975.

[76] G. Baccarani, B. Riccò, and G. Spadini, "Transport properties of polycrystalline silicon films," *Journal of Applied Physics*, vol. 49, pp. 5565-5570, 1978.

[77] R. L. Petritz, "Theory of Photoconductivity in Semiconductor Films," *Physical Review*, vol. 104, pp. 1508-1516, 12/15/ 1956.

[78] T. Ohgaki, Y. Kawamura, T. Kuroda, N. Ohashi, Y. Adachi, T. Tsurumi, *et al.*, "Optical Properties of Heavily Aluminum-Doped Zinc Oxide Thin Films Prepared by Molecular Beam Epitaxy," *Key Engineering Materials*, vol. 248, pp. 91-94, 2003.

[79] Y. N. Kento hirohata, Nobuto Oka, yasushi Sato, Isao Yamamoto and Yuzo Shigesato, "High Rate Deposition of Al-doped ZnO by Reactive Sputtering," *Mater. Res. Soc. Symp. Proc.*, vol. 1109-B, 2009.

[80] J. J. Berry, D. S. Ginley, and P. E. Burrows, "Organic light emitting diodes using a Ga:ZnO anode," *Applied Physics Letters*, vol. 92, p. 193304, 2008.

[81] G. Ma, D. Li, H. Ma, J. Shen, C. Wu, J. Ge, *et al.*, "Carrier concentration dependence of terahertz transmission on conducting ZnO films," *Applied Physics Letters*, vol. 93, p. 211101, 2008.

[82] S. Jäger, B. Szyszka, J. Szczyrbowski, and G. Bräuer, "Comparison of transparent conductive oxide thin films prepared by a.c. and d.c. reactive magnetron sputtering," *Surface and Coatings Technology*, vol. 98, pp. 1304-1314, 1// 1998.

[83] S. Cornelius, M. Vinnichenko, N. Shevchenko, A. Rogozin, A. Kolitsch, and W. Möller, "Achieving high free electron mobility in ZnO:Al thin films grown by reactive pulsed magnetron sputtering," *Applied Physics Letters*, vol. 94, p. 042103, 2009.

[84] H. Tanaka, K. Ihara, T. Miyata, H. Sato, and T. Minami, "Low resistivity polycrystalline ZnO:Al thin films prepared by pulsed laser deposition," *Journal of Vacuum Science & Technology A: Vacuum, Surfaces, and Films*, vol. 22, p. 1757, 2004.

[85] H. Agura, A. Suzuki, T. Matsushita, T. Aoki, and M. Okuda, "Low resistivity transparent conducting Al-doped ZnO films prepared by pulsed laser deposition," *Thin Solid Films,* vol. 445, pp. 263-267, 2003.

[86] R. J. Mendelsberg, S. H. N. Lim, Y. K. Zhu, J. Wallig, D. J. Milliron, and A. Anders, "Achieving high mobility ZnO : Al at very high growth rates by dc filtered cathodic arc deposition," *Journal of Physics D: Applied Physics,* vol. 44, p. 232003, 2011.

[87] Z. B. Ayadi, L. El Mir, K. Djessas, and S. Alaya, "The properties of aluminum-doped zinc oxide thin films prepared by rf-magnetron sputtering from nanopowder targets," *Materials Science and Engineering: C,* vol. 28, pp. 613-617, 2008.

[88] D. Dimova-Malinovska, N. Tzenov, M. Tzolov, and L. Vassilev, "Optical and electrical properties of R.F. magnetron sputtered ZnO:Al thin films," *Materials Science and Engineering: B,* vol. 52, pp. 59-62, 3/6/ 1998.

[89] T. Ootsuka, Z. Liu, M. Osamura, Y. Fukuzawa, R. Kuroda, Y. Suzuki, *et al.*, "Studies on aluminum-doped ZnO films for transparent electrode and antireflection coating of β-FeSi2 optoelectronic devices," *Thin Solid Films,* vol. 476, pp. 30-34, 2005.

[90] Y. Okuhara, T. Kato, H. Matsubara, N. Isu, and M. Takata, "Near-infrared reflection from periodically aluminium-doped zinc oxide thin films," *Thin Solid Films,* vol. 519, pp. 2280-2286, 2011.

[91] T. Dhakal, A. S. Nandur, R. Christian, P. Vasekar, S. Desu, C. Westgate, *et al.*, "Transmittance from visible to mid infra-red in AZO films grown by atomic layer deposition system," *Solar Energy,* vol. 86, pp. 1306-1312, 2012.

[92] M.-C. Jun, S.-U. Park, and J.-H. Koh, "Comparative studies of Al-doped ZnO and Ga-doped ZnO transparent conducting oxide thin films," *Nanoscale Research Letters,* vol. 7, p. 639, 2012.

[93] J. Steinhauser, "LOW PRESSURE CHEMICAL VAPOR DEPOSITED ZINC OXIDE FOR SILICON THIN FILM SOLAR CELLS - OPTICAL AND ELECTRICAL PROPERTIES," PhD Thesis, PhD Thesis, UNIVERSITY OF NEUCHÂTEL, 2008.

[94] G. Gruner, "Carbon nanotube films for transparent and plastic electronics," *Journal of Materials Chemistry,* vol. 16, p. 3533, 2006.

[95] J. Li, L. Hu, L. Wang, Y. Zhou, G. Grüner, and T. J. Marks, "Organic Light-Emitting Diodes Having Carbon Nanotube Anodes," *Nano Letters,* vol. 6, pp. 2472-2477, 2006/11/01 2006.

[96] H.-Z. Geng, K. K. Kim, K. P. So, Y. S. Lee, Y. Chang, and Y. H. Lee, "Effect of Acid Treatment on Carbon Nanotube-Based Flexible Transparent Conducting Films," *Journal of the American Chemical Society,* vol. 129, pp. 7758-7759, 2007/06/01 2007.

[97] L. Gomez De Arco, Y. Zhang, C. W. Schlenker, K. Ryu, M. E. Thompson, and C. Zhou, "Continuous, Highly Flexible, and Transparent Graphene Films by Chemical Vapor Deposition for Organic Photovoltaics," *ACS Nano,* vol. 4, pp. 2865-2873, 2010/05/25 2010.

[98] Z. Wu, Z. Chen, X. Du, J. M. Logan, J. Sippel, M. Nikolou, *et al.*, "Transparent, Conductive Carbon Nanotube Films," *Science,* vol. 305, pp. 1273-1276, August 27, 2004 2004.

[99] R. G. Gordon, "Criteria for Choosing Transparent Conductors," *MRS Bulletin,* vol. 25, pp. 52-57, 2000.

[100] D. S. Hecht, L. Hu, and G. Irvin, "Emerging transparent electrodes based on thin films of carbon nanotubes, graphene, and metallic nanostructures," *Adv Mater,* vol. 23, pp. 1482-513, Apr 5 2011.

[101] S. M. Bergin, Y. H. Chen, A. R. Rathmell, P. Charbonneau, Z. Y. Li, and B. J. Wiley, "The effect of nanowire length and diameter on the properties of transparent, conducting nanowire films," *Nanoscale,* vol. 4, pp. 1996-2004, Mar 21 2012.

[102] M. Foygel, R. D. Morris, D. Anez, S. French, and V. L. Sobolev, "Theoretical and computational studies of carbon nanotube composites and suspensions: Electrical and thermal conductivity," *Physical Review B,* vol. 71, p. 104201, 03/04/ 2005.

[103] A. Madaria, A. Kumar, F. Ishikawa, and C. Zhou, "Uniform, highly conductive, and patterned transparent films of a percolating silver nanowire network on rigid and flexible substrates using a dry transfer technique," *Nano Research,* vol. 3, pp. 564-573, 2010/08/01 2010.

[104] J. Tang, D. Tang, B. Su, Q. Li, B. Qiu, and G. Chen, "Silver nanowire–graphene hybrid nanocomposites as label for sensitive electrochemical immunoassay of alpha-fetoprotein," *Electrochimica Acta,* vol. 56, pp. 8168-8175, 10/1/ 2011.

[105] M. Zhu, P. Chen, and M. Liu, "Graphene Oxide Enwrapped Ag/AgX (X = Br, Cl) Nanocomposite as a Highly Efficient Visible-Light Plasmonic Photocatalyst," *ACS Nano,* vol. 5, pp. 4529-4536, 2011/06/28 2011.

[106] L. W. Schwartz, P. Moussallp, P. Campbell, and R. R. Eley, "Numerical Modelling of Liquid Withdrawal from Gravure Cavities in Coating Operations," *Chemical Engineering Research and Design,* vol. 76, pp. 22-28, 1// 1998.

[107] G. L. Harry, "Slot Die Coating for Low Viscosity Fluids," in *Coatings Technology Handbook, Third Edition*, ed: CRC Press, 2005, pp. 19-1-19-15.

[108] C. H. Liu and X. Yu, "Silver nanowire-based transparent, flexible, and conductive thin film," *Nanoscale Res Lett,* vol. 6, p. 75, 2011.

[109] M. G. Faraj and K. Ibrahim, "Optical and Structural Properties of Thermally Evaporated Zinc Oxide Thin Films on Polyethylene Terephthalate Substrates," *International Journal of Polymer Science,* vol. 2011, pp. 1-4, 2011.

[110] H. Chen, Y. Gao, H. Zhang, L. Liu, H. Yu, H. Tian, *et al.*, "Transmission-Electron-Microscopy Study on Fivefold Twinned Silver Nanorods," *The Journal of Physical Chemistry B,* vol. 108, pp. 12038-12043, 2004/08/01 2004.

[111] X. Wen, Y.-T. Xie, W. C. Mak, K. Y. Cheung, X.-Y. Li, R. Renneberg, *et al.*, "Dendritic Nanostructures of Silver: Facile Synthesis, Structural Characterizations, and Sensing Applications," *Langmuir,* vol. 22, pp. 4836-4842, 2006/05/01 2006.

[112] C. Ding, C. Tian, R. Krupke, and J. Fang, "Growth of non-branching Ag nanowires via ion migrational-transport controlled 3D electrodeposition," *CrystEngComm,* vol. 14, p. 875, 2012.

[113] Y. Lu, J. Y. Huang, C. Wang, S. Sun, and J. Lou, "Cold welding of ultrathin gold nanowires," *Nat Nanotechnol,* vol. 5, pp. 218-24, Mar 2010.

[114] Q. Nian, M. Y. Zhang, B. D. Schwartz, and G. J. Cheng, "Ultraviolet laser crystallized ZnO:Al films on sapphire with high Hall mobility for simultaneous enhancement of conductivity and transparency," *Applied Physics Letters,* vol. 104, pp. -, 2014.

[115] B. Li, X. Wen, R. Li, Z. Wang, P. G. Clem, and H. Fan, "Stress-induced phase transformation and optical coupling of silver nanoparticle superlattices into mechanically stable nanowires," *Nat Commun,* vol. 5, p. 4179, 2014.

[116] D. Langley, G. Giusti, C. Mayousse, C. Celle, D. Bellet, and J. P. Simonato, "Flexible transparent conductive materials based on silver nanowire networks: a review," *Nanotechnology,* vol. 24, p. 452001, Nov 15 2013.

[117] J. van de Groep, P. Spinelli, and A. Polman, "Transparent Conducting Silver Nanowire Networks," *Nano Letters,* vol. 12, pp. 3138-3144, 2012/06/13 2012.

[118] S. Karim, M. E. Toimil-Molares, A. G. Balogh, W. Ensinger, T. W. Cornelius, E. U. Khan, *et al.*, "Morphological evolution of Au nanowires controlled by Rayleigh instability," *Nanotechnology,* vol. 17, pp. 5954-5959, 2006.
[119] D. Stauffer and A. Aharony, *Introduction to Percolation Theory*: Taylor & Francis, 1992.
[120] S. Karim, M. E. Toimil-Molares, A. G. Balogh, W. Ensinger, T. W. Cornelius, E. U. Khan, *et al.*, "Morphological evolution of Au nanowires controlled by Rayleigh instability," *Nanotechnology,* vol. 17, p. 5954, 2006.

VITA

VITA

Qiong Nian

EDUCATION:

Ph. D. in Industrial Engineering, Purdue University, West Lafayette, IN, August 2015

Advisor: Gary J. Cheng

Title of Dissertation: "Ultra-fast laser enhanced printing of Nanomaterial for high quality transparent electrode"

B.S. in Materials science and Engineering, University of Sci&Tech of China, Hefei, China, June 2010

Advisor: Xingqin Liu

Title of Dissertation: "Layered $SmBaCuCoO_{5+\delta}$ and $SmBaCuFeO_{5+\delta}$ perovskite oxides as cathode materials for proton-conducting solid state fuel cells"

RESEARCH INTEREST:

- Laser-based advanced manufacturing and materials processing: Laser induced plasmonic welding, laser crystallization, pulsed laser ablation, laser micro machining/scribing, laser-matter interaction, etc.
- Renewable energy device fabrication and manufacturing: thin film solar cell laser annealing, thin film laser patterning/scribing, alternative polymer/perovskite photovoltaic, 3D printing of complex structure for energy harvesting
- Micro/Nanoscale manufacturing, manufacturing process simulation, nanomaterials synthesis and processing.
- 3D/porous structure synthesis, fabrication and assembly for energy harvesting/storage, specifically in lithium ion battery and super capacitor.

PUBLICATIONS

PUBLICATIONS

1. Qiong Nian, Michael Callahan, David Look, John Bailey, Harry Efstathiadis, Mojib, Saei, Gary Cheng, Large Scale Laser Crystallization of Solution-based Alumina-doped Zinc Oxide (AZO) Nanoinks for Highly Transparent Conductive Electrode, ***Scientific Reports***, in press, 2015.
2. Suprem Das/Qiong Nian (co-first author), mojib Saei, Prashant Kumar, David Janes, Muhammad Alam, Gary J. Cheng, "Single Layer Graphene as a barrier layer for intense UV laser induced damages for Silver Nanowire Network", ***ACS Nano***, in press, 2015.
3. Qiong Nian, Yang Xu, Ganguli Sabyasachi, Dong Lin, Mojib Saei, Biwei Deng, Wenqi Wang, Gary J. Cheng, "Crystalline Nanojoining Silver Nanowire Percolated Networks on Flexible Substrate", ***ACS Nano***, online, 2015.
4. Yaowu Hu, Seunghyun Lee, Prashant Kumar, Qiong Nian, Wenqi Wang, Joseph Irudayaraj, Gary J. Cheng, "Water flattens graphene wrinkles: laser shock wrapping of graphene onto substrate-supported crystalline plasmonic nanoparticle arrays", ***Nanoscale***, online, 2015.
5. Kelly Rickey, Qiong Nian, Genqiang Zhang, Liangliang Chen, Sergey Suslov, S. Venkataprasad Bhat, Yue Wu, Gary Cheng, Xiulin Ruan, "Welding of Semiconductor Nanowires by Coupling Laser-Induced Peening and Localized Heating", ***Scientific Reports***, in press, 2015.
6. Qiong Nian, Kyle H. Montgomery, Xin Zhao, Thomas N. Jackson, Jerry M. Woodall, Gary Cheng, "InP/i-ZnO/Al-ZnO Heterojunction Solar Cells Using Pulsed Laser Deposition", ***Applied Physics A***: 1-8, 2015
7. Dong Lin, Prashant Kumar, Shengyu Jin, Shuo Liu, Qiong Nian, Gary J. Cheng, "Laser direct writing of crystalline Fe2O3 atomic sheets on steel surface in aqueous medium", ***Applied Surface Science***, 351, 148, 2015.
8. Qiong Nian, Martin Zhang, Dong Lin, Suprem Das, Yung Shin, Gary Cheng, "Crystalline photoactive copper indium diselenide thin films by pulsed laser crystallization of nanoparticle-inks at ambient conditions", ***RSC Advances***, 5(71), 57550, 2015.
9. Qiong Nian, Michael Callahan, David Look, Harry Efstathiadis, John Bailey, Gary Cheng, "Highly Transparent Conductive Electrode with Ultra-low HAZE by Grain Boundary Modification of Aqueous Solution Fabricated Alumina-Doped Zinc Oxide (AZO) Nanocrystals", ***APL Materials***, 3(6), 062803, 2015 (Invited).
10. Qiong Nian**,** Yuefeng Wang, Yingling Yang, Ji Li, Martin Y Zhang, Jiayi Shao, Liang Tang, Gary J Cheng, Direct Laser Writing of Nanodiamond Films from Graphite under Ambient Conditions, ***Scientific Reports,*** 4, 6612 (2014)

11. Dong Lin , Qiong Nian, Biwei Deng , Shengyu Jin , Yaowu Hu , Wenqi Wang , and Gary J. Cheng, Three-Dimensional Printing of Complex Structures: Man Made or toward Nature? ***ACS Nano,*** 8(10), 9710 (2014) (Invited)
12. Qiong Nian**,** Martin Y. Zhang, Bradley Schwartz, Gary J. Cheng, Ultraviolet laser crystallized ZnO:Al films on sapphire with high Hall mobility for simultaneous enhancement of conductivity and transparency, ***Applied Physics Letters*****, 104,** 201907 (2014)
13. Qiong Nian**,** MY Zhang, Y Wang, SR Das, VS Bhat, F Huang, GJ Cheng, 2014, Charger Carrier Transport and Collection Enhancement of Copper Indium Diselenide Photoactive Nanoparticle-Ink by Laser Crystallization, ***Applied Physics Letters*****,** 105, 111909 (2014)
14. Xin Zhao, Yunfeng Cao, Qiong Nian, Yung C Shin, Gary Cheng, Precise selective scribing of thin-film solar cells by a picosecond laser, ***Applied Physics A,*** 116, 671 (2014)
15. Xin Zhao, Yunfeng Cao, Qiong Nian, Gary Cheng, Yung C Shin, Control of Ablation Depth and Surface Structure in P3 Scribing of Thin-Film Solar Cells by A Picosecond Laser, ***Journal of Micro and Nano-Manufacturing*** (2014)
16. Bryan T Spann, S Venkataprasad Bhat, Qiong Nian, Kelly M Rickey, Gary J Cheng, Xiulin Ruan, Xianfan Xu, Enhancing photo-induced ultrafast charge transfer across heterojunctions of CdS and laser-sintered TiO 2 nanocrystals***, Physical Chemistry Chemical Physics***, 16, 10669 (2014)
17. Qiong Nian**,** CR Liu, GJ Cheng, 2013, "Laser assisted electro-deposition of earth abundant Cu2ZnSnS4 photovoltaic thin film", ***Manufacturing Letters*** (2013)
18. MY Zhang, Q Nian, Y Shin, GJ Cheng, Direct pulsed laser crystallization of nanocrystals for absorbent layers in photovoltaics: Multiphysics simulation and experiment, ***Journal of Applied Physics***, 113 (19), 193506 (2013)
19. P Kumar, J Li, Q Nian, Y Hu, GJ Cheng, Plasmonic tuning of silver nanowires by laser shock induced lateral compression, ***Nanoscale***, 5 (14), 6311-6317 (2013)
20. Martin Y. Zhang, Qiong Nian, Gary J. Cheng, Room Temperature Deposition of Alumina-doped zinc oxide (AZO) on flexible substrates by Direct Pulsed Laser recrystallization, ***Applied Physics Letter,*** 100, 151902 (2012)